

**Bottom-up synthesis of Nicotinamide Adenine Dinucleotide
(NAD) regeneration modules for artificial cells**

Dissertation

Zur Erlangung des akademischen Grades

Doktoringenieurin

(Dr. -Ing.)

von **M.Sc. MinHui Wang**

geb.am 30th of May 1987 in Fuzhou, Jiangxi, China

genehmigt durch die Fakultät für Verfahrens- und Systemtechnik
der Otto-von-Guericke-Universität Magdeburg

Promotionskommision: Prof. Dr.rer.nat. Franziska Scheffler (Vorsitz)
 Prof. Dr.-Ing. Kai Sundmacher (Gutachter)
 Dr. Dora Tang (Gutachter)
 Dr. Lucas Caire da Silva (Gutachter)

eingereicht am: 7 January 2022

Promotionskolloquium am: 19 April 2022

Abstract

With the bottom-up approach to synthetic biology, we are trying to develop an artificial biological system with minimal but essential components in order to better understand the basic mechanisms of life and further refine, advance, and improve it for diverse applications. This approach involves piecing together essential biological functional modules and their further engineering, controlling, and re-designing towards an increasing complexity. Considering a minimal blueprint revolving around metabolism, we envision a synthetic cell consisting of an ATP energy regeneration module, a NAD regeneration module, as well as enzymatic cascades, all enclosed in a common compartment.

In this thesis, we aimed to develop NAD regeneration modules for synthetic cells. We have demonstrated a highly simplified and feasible strategy for the transmembrane NAD regeneration by placing NAD inside the membrane and redox agents outside with the aid of mediators embedded in the same membrane. We used different types of membranes in two different testing platforms – black lipid membranes (BLMs) and vesicles and studied the NAD regeneration.

Firstly, we investigated the NAD^+ regeneration in black lipid membranes with embedded conductive agents and redox catalysts (methylene blue). The molecular wires were successfully embedded in BLMs and the conductivity increased. However, due to the limited stability of the setup, the introduced permeability of the membrane, and the low activity of methylene blue for oxidation of NADH, this approach turned out not to be feasible in the context of the envisioned synthetic cell.

Then, we developed a versatile NAD regeneration module via the transmembrane oxidation and reduction of encapsulated NADH/ NAD^+ facilitated by other mediators embedded in vesicles. In the case of NAD^+ regeneration, we thoroughly investigated the process and described the system behaviour through a simple dimensionless kinetic model. Furthermore, we have studied the effects of different membrane compositions at two size scales. These results move us closer to the sustainable redox management of synthetic cells and provide model systems for better understanding of natural membrane-related phenomena.

Zusammenfassung

Mit dem Bottom-up-Ansatz der synthetischen Biologie versuchen wir, ein künstliches biologisches System mit minimalen, aber essentiellen Komponenten zu entwickeln, um grundlegende Mechanismen des Lebens besser zu verstehen und für vielfältige Anwendungen weiter zu verfeinern, voranzutreiben und zu verbessern. Dieser Ansatz beinhaltet die Zusammenstellung wesentlicher biologischer Funktionsmodule und deren weitere Entwicklung, Steuerung und Neugestaltung hin zu einer Komplexitätssteigerung. Unter Berücksichtigung eines minimalen Bauplans, der sich um den Stoffwechsel dreht, stellen wir uns eine synthetische Zelle vor, die aus einem ATP-Energiergenerationsmodul, einem NAD-Regenerationsmodul sowie einer enzymatischen Kaskade besteht, die alle in einem gemeinsamen Kompartiment eingeschlossen sind.

In dieser Arbeit war es das Ziel, die NAD-Regenerationsmodule für die synthetischen Zellen zu entwickeln. Wir haben eine stark vereinfachte und praktikable Strategie für die transmembrane NAD-Regeneration entwickelt, indem wir NAD innerhalb der Membran und Redox-Agenzien außerhalb mit Hilfe von in derselben Membran eingebetteten Mediatoren platzierten. Wir verwendeten verschiedene Membrantypen in zwei verschiedenen Testplattformen – schwarze Lipidmembranen (BLMs) und Vesikel – und untersuchten die NAD-Regeneration.

Zunächst untersuchten wir die NAD^+ -Regeneration in schwarze Lipidmembranen mit eingebetteten leitfähigen Substanzen und einem Redoxkatalysator (Methylenblau). Diese molekularen Drähte wurden erfolgreich in BLMs eingebettet und die Leitfähigkeit erhöht. Aufgrund der begrenzten Stabilität des Aufbaus, der eingeführten Permeabilität der Membran und der geringen Aktivität von Methylenblau für die Oxidation von NADH erwies sich dieser Ansatz jedoch im Kontext der anvisierten synthetischen Zelle als nicht praktikabel.

Aus diesem Grund entwickelten wir danach ein vielseitiges NAD-Regenerationsmodul aus einer transmembranen Oxidation und Reduktion von eingekapseltem NADH/NAD^+ , das durch andere in Vesikel eingebettete Mediatoren ermöglicht wird. Im Falle der NAD^+ -Regeneration haben wir den Prozess gründlich untersucht und das Systemverhalten mit einem einfachen, dimensionslosen kinetischen Modell beschrieben. Darüber hinaus haben wir die

Auswirkungen unterschiedlicher Membranzusammensetzungen auf zwei Größenskalen untersucht. Diese Ergebnisse bringen uns dem nachhaltigen Redoxmanagement synthetischer Zellen näher und liefern Modellsysteme zum besseren Verständnis natürlicher Membranphänomene.

List of Figures

FIGURE 1.1 SCHEMATIC REPRESENTATION OF THE PROPOSED WORKFLOW ADOPTED IN MAXSYNBIO TO CONSTRUCT A MINIMAL CELLULAR SYSTEM ²⁴	4
FIGURE 1.2 SCHEME OF A FICTIONAL SYNTHETIC CELL DESIGNED WITHIN MAXSYNBIO IN MAGDEBURG, CONSISTING OF AN ATP ENERGY REGENERATION MODULE (ORANGE), A NAD REGENERATION MODULE (GREEN), AND METABOLIC ENZYMATIC CASCADES (BLUE, S: SUBSTRATE, E: ENZYME, P: PRODUCT) WHICH ARE ALL INCLUDED IN A CLOSED COMPARTMENT (BLACK).	5
FIGURE 1.3 THE FLUID MOSAIC MODEL OF A NATURAL MEMBRANE WITH THE SCHEMATIC THREE- DIMENSIONAL CROSS-SECTIONAL VIEW, ADAPTED BY G.L. NICOLSON ³⁷ FROM SINGER AND NICOLSON ³⁰	6
FIGURE 2. 1 SCHEMATIC ILLUSTRATION OF A NAD REGENERATION MODULE. (YELLOW AND BLUE CIRCLES INDICATE MEDIATORS).	10
FIGURE 3.1 STRUCTURE OF NAD ⁺ (LEFT) AND THE SIMPLIFIED STRUCTURES SHOWING THE REDOX REACTION OF NAD ⁺ /NADH (RIGHT).	12
FIGURE 4.1 SCHEMATIC OF A PAINTED BLM IN A CHAMBER.	16
FIGURE 4.2 MOLECULAR STRUCTURES (RIGHT) OF PHOSPHOGLYCERIDES WITH PALMITATE AND OLEATE TAILS AND THEIR SCHEMATIC STRUCTURE (LEFT) INDICATING THE HYDROPHILIC HEAD (A CIRCLE) AND TWO HYDROPHOBIC TAILS (TWO LINES) AS THE TYPICAL PHOSPHOLIPID ABLE TO FORM A LIPID MEMBRANE.	17
FIGURE 4.3 MOLECULAR SHAPES AND CRITICAL PACKING PARAMETERS OF SURFACTANTS AND LIPIDS AND THE CORRESPONDING RESULTING STRUCTURES ⁷⁹	19
FIGURE 4.4 COMMONLY OBSERVED CRYSTALLINE AND LIQUID CRYSTALLINE PHASES OF LIPIDS ⁸³	20
FIGURE 4.5 SCHEMATIC ILLUSTRATION OF NAD ⁺ REGENERATION IN BLMs BY INCORPORATION OF DSSN AND METHYLENE BLUE AS CATALYTIC MEDIATOR (C).	22
FIGURE 4.6 TESTING CHAMBER (LEFT) AND BILAYER SCOUT DEVICE (RIGHT) FROM IONOVIATION GMBH.	23

FIGURE 4.7 SCREENSHOT OF CURRENT PROFILE (IN BLACK) OF A STABLE BLACK LIPID MEMBRANE (BLM) PREPARED BY POPC/POPE/POPS (8:1:1 WT%) WITH A CONSTANT APPLIED VOLTAGE (IN RED) OF 60 mV SHOWN IN PATCHMASTER.....	24
FIGURE 4.8 UV/VIS SPECTRA OF NAD ⁺ (B, MAGENTA), NADH (B, CYAN), METHYLENE BLUE (MB, A, BLUE), AND MB MIXED WITH NADH FOR 40 MIN (A, BLACK) AND 130 MIN (A, RED) AFTER PURGING WITH OXYGEN (WITH A MOLAR RATIO OF NADH TO MB = 15:1). ...	26
FIGURE 4.9 TIME COURSES OF ABSORBANCE OF NADH (BLACK, AT 340 NM), METHYLENE BLUE (MB, RED, AT 609 NM, AND GREEN, 665 NM) AND FLUORESCENCE INTENSITY OF NADH (BLUE, $\lambda_{EX} = 340$ NM, $\lambda_{EM} = 460$ NM), (RIGHT, BLUE) IN THE OPEN AIR (WITH A MOLAR RATIO OF NADH TO MB = 3:1).....	27
FIGURE 4.10 MEAN CURRENT CHANGE RESPONDING TO THE APPLIED VOLTAGE CHANGE OF DIFFERENT BLMs (CONSIST OF POPC/POPE/POPS 8:1:1 WT%): PURE BILAYER, BLMs WITH EMBEDDED HEMOLYSIN, GRAMICIDIN A AND DSSN.	28
FIGURE 4.11 CURRENT AND VOLTAGE CHANGE OF BLMs CONSISTING OF POPC/POPE/POPS 8:1:1 WT%, WITH 5 μ M DSSN EMBEDDED, MONITORED OVER TIME.	29
FIGURE 4.12 MEAN CURRENT CHANGE RESPONDING TO THE APPLIED VOLTAGE CHANGE OF DPhPC BLMs WITH DIFFERENT CONCENTRATIONS OF EMBEDDED DSSN: 0 (PURE BILAYER), 5 μ M, 10 μ M, 20 μ M, AND 50 μ M.	30
FIGURE 4.13 MEAN CONDUCTANCE CHANGE RESPONDING TO THE APPLIED VOLTAGE CHANGE OF DPhPC BLMs WITH DIFFERENT CONCENTRATIONS OF EMBEDDED DSSN: 0 (PURE BILAYER), 5 μ M, 10 μ M, 20 μ M, AND 50 μ M.	31
FIGURE 4.14 CONDUCTANCE AND CAPACITANCE CHANGE OF DPhPC BLMs, WITH 20 μ M DSSN EMBEDDED, MONITORED OVER TIME.	32
FIGURE 4.15 UV/VIS SPECTRA OF DSSN AT DIFFERENT CONCENTRATIONS.....	33
FIGURE 4.16 FLUORESCENCE INTENSITY VERSUS DSSN CONCENTRATION (λ_{EX} : 485 NM, λ_{EM} : 590 NM).	34
FIGURE 4.17 FLUORESCENT IMAGE OF DSSN EMBEDDED IN POPC SUSPENSIONS.	34
FIGURE 5.1 LIPID BILAYER STRUCTURE AND TYPES OF VESICLES ⁹⁷	37
FIGURE 5.2 MOLECULAR STRUCTURE (LEFT) OF PDMS- <i>g</i> -PEO AND ITS SCHEMATIC STRUCTURE (RIGHT) INDICATES HYDROPHILIC HEAD (RED) AND HYDROPHOBIC BACKBONES (BLACK).	39

FIGURE 5.3 SCHEMATIC PRESENTATION OF THE ANALOGY OF NATURAL ELECTRON TRANSPORT CHAIN IN MITOCHONDRIA (A) AND TCNQ BASED NAD ⁺ REGENERATION MODULE (B) ¹¹⁸ .	40
FIGURE 5.4 SCHEMATIC PRESENTATION OF THE LUVs PREPARATION PROCEDURE.....	42
FIGURE 5.5 SCHEMATIC PRESENTATION OF THE GUVs PREPARATION PROCEDURES.....	47
FIGURE 5.6 NORMALIZED NADH FLUORESCENCE PROFILES OF TIME-DEPENDENT REACTION OF NADH OXIDATION WITH FERRICYANIDE IN MOPS BUFFER (100 mM MOPS, 250 mM KCL, TRIS, PH 7.2) AT DIFFERENT MOLAR RATIOS OF NADH TO FERRICYANIDE (1:0, 1:1, 1:2, 1:5, AND 1:10).	50
FIGURE 5.7 FLUORESCENCE MICROSCOPY IMAGE OF POPC VESICLES WITH TCNQ RECONSTITUTED (LEFT) AND MEMBRANE DYE NR (RIGHT) UNDER THE EXCITATION OF BLUE LIGHT.	51
FIGURE 5.8 SIZE DISTRIBUTIONS OF DIFFERENT LUVs: POPC VESICLES, VESICLES WITH TCNQ, UQ, AND NR RECONSTITUTED WITH AND WITHOUT ENCAPSULATION OF NADH.....	52
FIGURE 5.9 FLUORESCENCE INTENSITY AND NORMALIZED PROFILES OF NADH IN DIFFERENT VESICULAR CONFIGURATIONS OVER TIME.....	57
FIGURE 5.10 A) NADH CONCENTRATION PROFILE: NADH LOADED (20 μM INPUT) IN POPC-TCNQ VESICLES REACT WITH DIFFERENT CONCENTRATIONS OF FERRICYANIDE (0-BLUE, 100μM-GREEN, 200 μM-RED, 400 μM-BLACK). B) FLUORESCENCE SPECTRA OF NADH AT DIFFERENT CONCENTRATIONS, INSET: NADH FLUORESCENCE INTENSITY IN DEPENDENCE ON THE NADH CONCENTRATION.	59
FIGURE 5.11 UV/VIS SPECTRA OF TCNQ AND LiTCNQ IN METHANOL.	66
FIGURE 5.12 UV/VIS SPECTRA OF HYDRATED POPC-TCNQ SUSPENSIONS IN THE PRESENCE OF 400 mM FERRICYANIDE.....	66
FIGURE 5.13 UV/VIS SPECTRA OF HYDRATED POPC-TCNQ SUSPENSIONS DURING AERATION WITH OXYGEN.	67
FIGURE 5.14 MEAN DIAMETER AND STANDARD DEVIATION (S.D.) OF DIFFERENT LUVs (ALL WITH ENCAPSULATION OF NADH) WITH DIFFERENT COMPOSITIONS OBTAINED FROM DLS.	69

FIGURE 5.15 TIME COURSES OF FLUORESCENCE INTENSITY PROFILES OF BARE AND FUNCTIONALIZED VESICLES AT DIFFERENT COMPOSITIONS, IN THE ABSENCE AND PRESENCE OF 400 μM POTASSIUM FERRICYANIDE.	74
FIGURE 5.16 TIME COURSES OF NORMALIZED NADH FLUORESCENT INTENSITY PROFILES MONITORED BY A FLUORESCENCE SPECTROMETER IN DIFFERENT NM-SCALE VESICLES WITH TCNQ INCORPORATED AFTER 400 μM FERRICYANIDE BEING ADDED AT $T = 0$	76
FIGURE 5.17 FLUORESCENT INTENSITY IN DEPENDENCE ON THE CARBOXYFLUORESCEIN (CF) CONCENTRATION AT AN EXCITATION WAVELENGTH OF 494 NM AND AN EMISSION WAVELENGTH OF 524 NM (BOTH SLIT WIDTH AT 2.5).....	77
FIGURE 5.18 FLUORESCENCE COURSES OF CARBOXYFLUORESCEIN ENCAPSULATED IN POPC LUVS AT 524 NM WITHOUT OR WITH EMBEDDED TCNQ IN 100 mM MOPS, 250 mM KCL, TRIS, PH 7.2.....	78
FIGURE 5.19 UV-VIS SPECTRA OF FERRICYANIDE WITH DIFFERENT CONCENTRATIONS (A) AND PURIFIED VESICLES (POPC, H1:4) WITH DIFFERENT AMOUNTS OF TCNQ (B). LINE: 420 NM.	79
FIGURE 5.20 FLUORESCENT IMAGES OF DIFFERENT VESICLES (A) GV, (B) GH1:4, (C) GMV1:4 WITH TCNQ INCORPORATED AND NADH ENCAPSULATED (LEFT: RED FLUORESCENCE OF PE-RHO, RIGHT: BLUE FLUORESCENCE OF NADH) (SCALE BAR: 50 μM).....	81
FIGURE 5.21 FLUORESCENT IMAGES OF (A) GV, (B) GH1:4, AND (C) GMV WITH TCNQ INCORPORATED AND NADH ENCAPSULATED AFTER ADDING 10 mM FERRICYANIDE (LEFT: RED FLUORESCENCE OF PE-RHO, MIDDLE: PHASE CONTRAST, RIGHT: BLUE FLUORESCENCE OF NADH) (SCALE BAR: 50 μM).....	83
FIGURE 5.22 CLSM IMAGES OF GV (A) AND GH1:4 (B) WITH TCNQ INCORPORATED AND NADH ENCAPSULATED (LEFT: FLUORESCENCE OF PE-RHO, MIDDLE: FLUORESCENCE OF NADH, RIGHT: BRIGHT FIELD) (SCALE BAR: 25 μM).....	84
FIGURE 5.23 TIME-LAPSE OF NADH IN GH1:4 CLSM IMAGES AFTER ADDING 10 mM FERRICYANIDE (RED: FLUORESCENCE OF PE-RHO, CYAN: FLUORESCENCE OF NADH), SCALE BAR: 10 μM	84
FIGURE 5.24 TIME-LAPSE OF NADH (BLUE) IN GH1:4 CLSM IMAGES AFTER ADDING 2 mM FERRICYANIDE (A) FROM LEFT TO RIGHT SHOWS $T \approx 0$, $T = 1$ MIN, $T = 2$ MIN, $T = 3$ MIN	

(SCALE BAR: 10 μM) AND THEIR CORRESPONDING NORMALIZED GRAY VALUE IN AVERAGE PROFILES OF GH1:4 (B).	86
FIGURE 5.25 TIME COURSES OF NORMALIZED NADH FLUORESCENT INTENSITY TRACES MONITORED IN GV CONTAINING NADH WITHOUT (A, B) WITH TCNQ (C, D) BEFORE (A, C) AND AFTER (B, D) ADDING 10 mM FERRICYANIDE.	90
FIGURE 5.26 TIME-LAPSE OF GV MICROSCOPE IMAGES AFTER ADDING 10 mM FERRICYANIDE (IMAGES OF FIGURE 5.25 D).	91
FIGURE 5.27 DIAMETERS (A) AND INITIAL FLUORESCENCE INTENSITY (B) OF ALL GVs FROM THE IMAGES PRESENTED IN FIGURE 5.26.	93
FIGURE 5.28 INITIAL FLUORESCENCE INTENSITY RELATIONSHIP WITH DIAMETERS OF GV (A) AND THEIR CORRESPONDING DECAY RATE (B).	94
FIGURE 6.1 NON-ENZYME REGENERATION OF NADH BY $[\text{Cp}^*\text{Rh}(\text{bpy})(\text{H}_2\text{O})]^{2+}$ SYNTHESIZED BY F. HOLLMANN ⁷³	95
FIGURE 6.2 FLUORESCENCE INTENSITY OF NADH IN MOPS BUFFER MONITORED OVER TIME BY STEPWISE ADDING DIFFERENT REAGENTS: 1= 2 mM NAD^+ , 2= 200 mM HCOONa , AND 3= 0.2 mM RHC.	97
FIGURE 6.3 THE SIZE DISTRIBUTION OF DIFFERENT POPC LUVs COMPOSED OF DIFFERENT MOLAR RATIOS OF RHC (25:1, AND 12.5:1) WITH AND WITHOUT ENCAPSULATION OF NAD^+ WITH (DASH LINES) AND WITHOUT (SOLID LINES) ADDING EXTERIOR REDUCING AGENT HCOONa	98
FIGURE 6.4 FLUORESCENCE INTENSITY PROFILE OF NADH IN DIFFERENT POPC-BASED LUVs COMPOSED OF DIFFERENT MOLAR RATIOS OF RHC (100:0, 50:1, 25:1, AND 12.5:1) WITH ENCAPSULATION OF NAD^+ AFTER ADDING EXTERIOR REDUCING AGENT HCOONa	99

List of Tables

TABLE 3.1 LIST OF NOTATIONS AND BASIC PROPERTIES OF LIPIDS USED IN THIS WORK.	11
TABLE 3.2 LIST OF THE INFORMATION ABOUT MEDIATORS AND OTHER ELECTRON AGENTS.	13
TABLE 3.3 LIST OF THE INFORMATION OF ALL OTHER CHEMICALS.	14
TABLE 5.1 SIZE AND CONCENTRATION DATA FOR VESICLES WITH RECONSTITUTED MEDIATORS AND ENCAPSULATED NADH OBTAINED FROM TRPS.	53
TABLE 5.2 INITIAL CONCENTRATIONS USED IN THE SIMULATION.	61
TABLE 5.3 ESTIMATED RATE AND EQUILIBRIUM CONSTANTS.	62
TABLE 5.4 SIZE DATA FOR VESICLES WITH TCNQ RECONSTITUTED AND ENCAPSULATED NADH OBTAINED FROM DLS.	69

Abbreviations

ADP – adenosine diphosphate

ATP – adenosine triphosphate

BLM – black lipid membrane

CF – carboxyfluorescein

CLSM – confocal laser scanning microscopy

CMC – critical micelle concentration

DAPI – 4',6-diamidino-2-phenylindole

DLS – dynamic light scattering

DOPC – 1,2-dioleoyl-*sn*-glycero-3-phosphocholine

DPhPC – 1,2-diphytanoyl-*sn*-glycero-3-phosphocholine

DSSN – 1,4'- bis (4' - (N,N - bis (6' - (N',N',N'-trimethylammonium) hexyl) amino) - styryl) stilbene tetraiodide

ETC – electron transport chain

FAD – flavin adenine dinucleotide

[Fe(CN)₆]³⁻ – potassium ferricyanide

[Fe(CN)₆]⁴⁻ – potassium ferrocyanide

GA – gramicidin A

GUVs – giant unilamellar vesicles

ITO – indium tin oxide

LUVs – large unilamellar vesicles

MB – methylene blue

MLVs – multilamellar vesicles

MOPS – (3-(*N*-morpholino)propanesulfonic acid

MVVs – multi-vesicular vesicles

NAD – nicotinamide adenine dinucleotide

NAD⁺ – oxidized NAD

NADH – reduced NAD

NADP – nicotinamide adenine dinucleotide phosphate

NR – Nile red

OG – octyl glucose

PC – phosphatidylcholine

PDI – polydispersity index

PDMS-*g*-PEO – poly(dimethylsiloxane)-*graft*-poly(ethylene oxide)

PE – phosphatidylethanolamine

PE-Rhod – 1,2-dioleoyl-*sn*-glycero-3-phosphoethanolamine-N-(lissamine rhodamine B sulfonyl) (ammonium salt)

PI – phosphatidylinositol

POPC – 1-palmitoyl-2-oleoyl-*sn*-glycero-3-phosphocholine

POPE – 1-palmitoyl-2-oleoyl-*sn*-glycero-3-phosphoethanolamine

POPS – 1-palmitoyl-2-oleoyl-*sn*-glycero-3-phospho-L-serine (sodium salt)

PS – phosphatidylserine

RhC – pentamethylcyclopentadienyl rhodium bipyridine complex

RSS – residual sum of squares

SUVs – small unilamellar vesicles

TCNQ – tetracyanoquinodimethane

T_m – phase transition temperature

TRPS – tunable resistive pulse sensing

UQ – ubiquinone-10

UVs – unilamellar vesicles

Table of Contents

Abstract.....	i
Zusammenfassung.....	iii
List of Figures.....	iv
List of Tables.....	ix
Abbreviations.....	x
Table of Contents.....	xii
1 Introduction.....	1
1.1 Background.....	1
1.2 Synthetic biology.....	1
1.3 MaxSynBio Project.....	3
1.4 Model membranes.....	5
1.5 Energy regeneration modules in synthetic cells.....	6
1.6 NAD-dependent metabolism.....	7
1.7 NAD regeneration methods.....	8
2 Aim of this work.....	10
3 Materials.....	11
3.1 Amphiphiles.....	11
3.2 NAD.....	12
3.3 Redox reagents.....	13
3.4 Other chemicals.....	14
4 NAD ⁺ regeneration in BLMs.....	15
4.1 Amphiphile composition and modular blueprint of regeneration module.....	17
4.1.1 Phospholipids.....	17
4.1.2 Design of NAD ⁺ regeneration module based on molecular wires.....	21
4.2 Experimental details.....	22
4.2.1 Oxidation of NADH with MB.....	22
4.2.2 Method for BLM study.....	23
4.2.3 NAD ⁺ regeneration in DSSN based BLMs.....	24
4.3 Oxidation of NADH with MB.....	25
4.4 Conductance studies in the BLM setup.....	27
4.5 Prospects for NAD ⁺ regeneration studies in BLMs.....	32

5	NAD ⁺ regeneration in vesicles.....	36
5.1	Amphiphile compositions and architecture of the regeneration module	37
5.1.1	Amphiphiles.....	37
5.1.2	Blueprint of the vesicular NAD ⁺ regeneration module.....	39
5.2	Experimental details.....	40
5.2.1	Oxidation of NADH with ferricyanide	40
5.2.2	Preparation and characterization of LUVs.....	41
5.2.3	NAD ⁺ regeneration in different LUVs.....	43
5.2.4	Modelling of TCNQ based NAD ⁺ regeneration in POPC LUVs.....	44
5.2.5	Leakage test	44
5.2.6	Preparation of different GUVs.....	45
5.2.7	NAD ⁺ regeneration in TCNQ based GUVs	48
5.3	NAD ⁺ regeneration in different LUVs.....	49
5.3.1	Oxidation of NADH with ferricyanide	49
5.3.2	Characterization of POPC LUVs with different mediators	50
5.3.3	NAD ⁺ regeneration in POPC LUVs with different mediators.....	53
5.3.4	Modelling of TCNQ based NAD ⁺ regeneration in POPC LUVs.....	57
5.3.5	Characterization of TCNQ based LUVs with different amphiphiles.....	67
5.3.6	NAD ⁺ regeneration in TCNQ based LUVs with different amphiphiles	70
5.3.7	Leakage test	76
5.4	NAD ⁺ regeneration in GUVs	80
5.4.1	Characterization of different GUVs.....	80
5.4.2	NAD ⁺ regeneration in different TCNQ based GUVs	81
6	Rhodium based NADH regeneration module.....	94
6.1	Experimental details.....	95
6.1.1	NAD ⁺ reduction by rhodium complex.....	95
6.1.2	NADH regeneration in rhodium-based LUVs	96
6.2	Reduction of NAD ⁺ with the rhodium complex	96
6.3	NADH regeneration in rhodium based LUVs	97
7	Conclusions and outlook.....	100
8	References.....	103

大道至简 (Dà Dào Zhì Jiǎn)

The greatest truths of the universe can be the simplest.

–Lao Zi

“Everything should be made as simple as possible, but not simpler.”

–Albert Einstein

1 Introduction

1.1 Background

As inspired by the quote from the ancient Chinese philosopher Lao Zi about Daoism which reads “*The greatest truths of the universe can be the simplest*”, and the great physicist Albert Einstein “*Everything should be made as simple as possible, but not simpler*”, during the process to understand the essence of life, we are trying to figure out the simplest life manifestation. The cell is the smallest yet still highly complex unit of life; thus, we would like to develop a minimal artificial cell containing only a few but essential components for its survival (self-maintenance, autopoiesis) and multiplication. “*What I cannot create, I do not understand.*” This is another quote from the American physicist Richard Feynman. Such “understanding by creating” can be applied as a feasible strategy via an engineering design to create a synthetic cell. In such a manner, it may be possible to find out how the very first life emerged and evolved from the non-living “primordial soup” and also to potentially explore simple synthetic cells, equipped with additional functions for pharmaceuticals production, pollutants elimination, and energy recovery, to name just a few.

Synthetic cell studies are related to a burgeoning multidisciplinary research area, **synthetic biology**¹. With the dramatic progress of biotechnology, systems engineering, genetic engineering, and molecular biology in the past decades, especially after the advanced development and cross-combination of the wealthy knowledge in physics, chemistry, biology, engineering, and computer science, synthetic biology is flourishing and considered to be one of the great promises for the future harnessing of biology²⁻³.

1.2 Synthetic biology

Synthetic biology aims to build up and re-design the *simplest* life-like cells and also to better understand the fundamental principles of life⁴⁻⁵. There are two approaches to create an artificial cell in synthetic biology, namely the top-down approach (by decomposition of natural

cells) and the bottom-up approach (by assembly of molecular pieces)⁶. The top-down approach is mainly related to the construction of a cell with a minimal vital system based on derived biological ancestry from the natural living cells by knocking out the non-essential parts. As pioneered by J.C. Venter and his colleagues, their team had studied the minimal *Mycoplasma* genome⁷, designed and chemically synthesized a minimal bacterial genome, and created the first “synthetic” bacterial cell⁸⁻⁹. Soon afterwards another international research project on synthetic yeast genome started and significant progress in the design of yeast has been made¹⁰⁻¹⁴. Meanwhile, Breuer *et al.* reported the first computational or “in silico” model for a synthetic minimal organism¹⁵. Quite recently, J.E. Venetz *et al.* started the chemical rewriting of a bacterial genome via a combination of computational tools¹⁶. This brings an inspiring parallel between artificial intelligence (AI) in software engineering that uses binary information and the natural code, mainly relying on four bases (ATGC), as a biological language. Thus, these synthetic genomes act as the “software” of synthetic cells. The other essential components of cells, analogous to the hardware of an AI machine, are the different functional parts and modules, such as compartments, energy modules, gene processing modules, metabolic modules, etc. They could be assembled from biochemical molecular bricks by mimicking natural cells. This is in fact the essence of the **bottom-up approach**, which is piecing together the necessary synthetic bricks by engineering, controlling, and re-designing protein-based functional toolkits, module by module¹⁷, first via cell-free strategies¹⁸ and thus gradually increasing complexity¹⁹. With such engineering principles of modularization, it is feasible to construct synthetic cells on the base of the hierarchical biological systems from parts to modules and systems step by step²⁰. This modular view is reflected for instance in the distinct consideration and versatility of energy regeneration systems for cell-free protein synthesis²¹.

Natural selection through the long evolution history (around 4 billion years) forced life to develop and modify itself unintentionally for better adaptation and then to pass these new features to the next generations in order to survive in extreme environments and on limited resources. These accumulations have brought some redundancy to life²². Considering that, synthetic biologists following the bottom-up approach are trying to synthesize simple, flexible parts and functional modules based on the same biochemical building blocks via a system engineering framework. This could be used to find out fundamental mechanisms of key

processes in natural cells and later on, to assemble and re-design synthetic functional cells, representing improved biotechnological systems with potential applications in drugs, green products, energy supply, etc.^{6, 20, 23}

1.3 MaxSynBio Project

The research conducted in this thesis was embedded in **MaxSynBio** – a Max Planck Research consortium in synthetic biology with research groups from nine Max Planck Institutes and research groups from the Friedrich Alexander University in Erlangen-Nuremberg and the University of Bordeaux. The primary goal of MaxSynBio was using the bottom-up approach to build up an artificial cell with minimal and essential non-living components, accompanied by computer-aided design, for the investigation of fundamental biological mechanisms and essential processes of life (Figure 1.1)²⁴. As a member of MaxSynBio, our research group applied knowledge in process systems engineering on the construction of controllable synthetic cells from compartments, energy modules, cofactor NAD modules, and metabolic enzymatic cascades (Figure 1.2). From the viewpoint of an engineer, natural cells can be considered as a highly efficient bioreactor or even a factory equipped with functional modules or systems²⁵⁻²⁷. Similarly, by mimicking and decomposing the natural cell, we can construct a minimal synthetic cell by creating an optimized cellular system through bringing together natural or “non-natural” molecules, functional parts, and modules. Further engineering, modifying, advancing, refining, and improving the latter should serve the purpose of better understanding of living systems, while generating new applications in industry and biological research on the other²⁴.

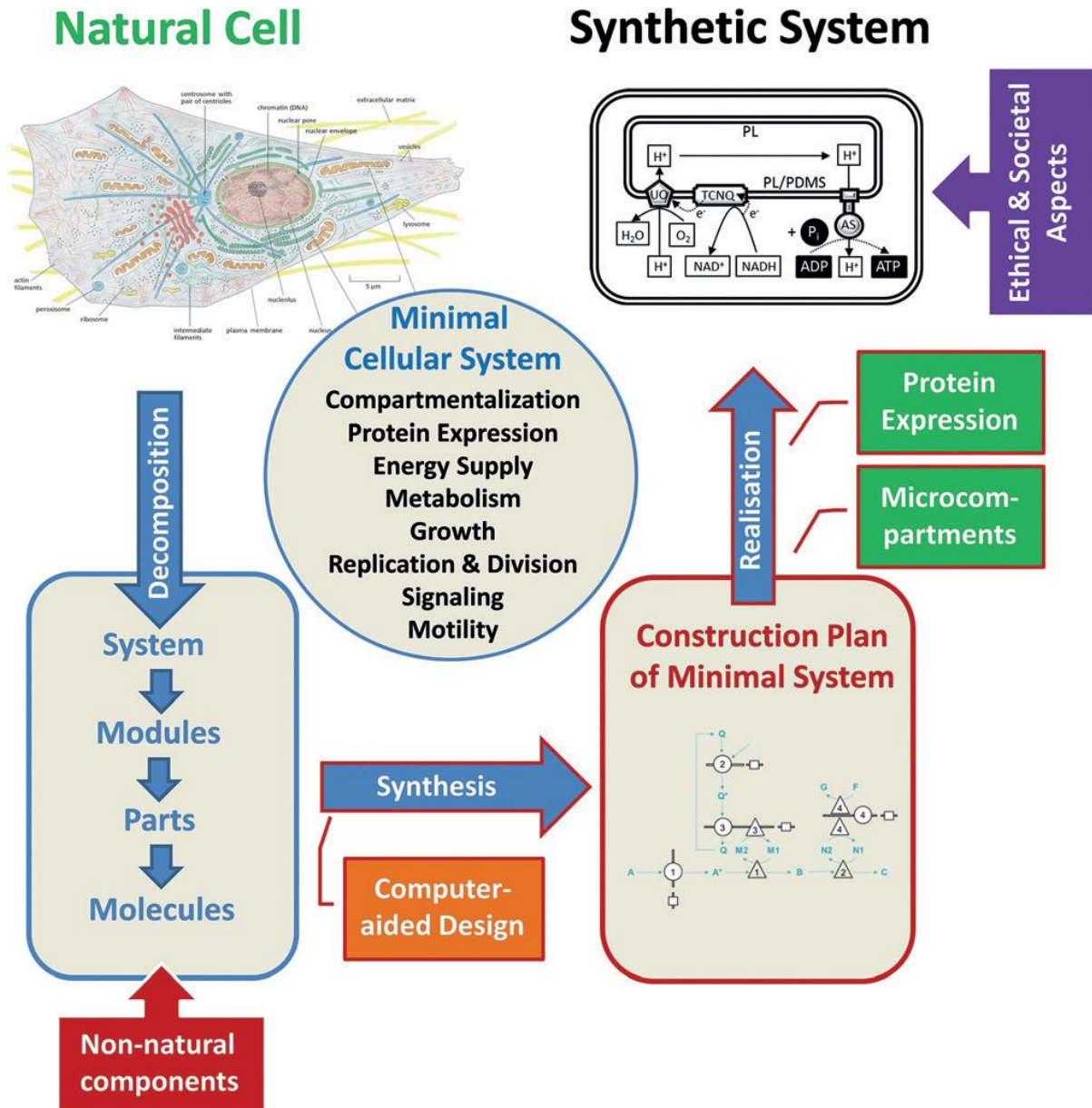


Figure 1.1 Schematic representation of the proposed workflow adopted in MaxSynBio to construct a minimal cellular system²⁴.

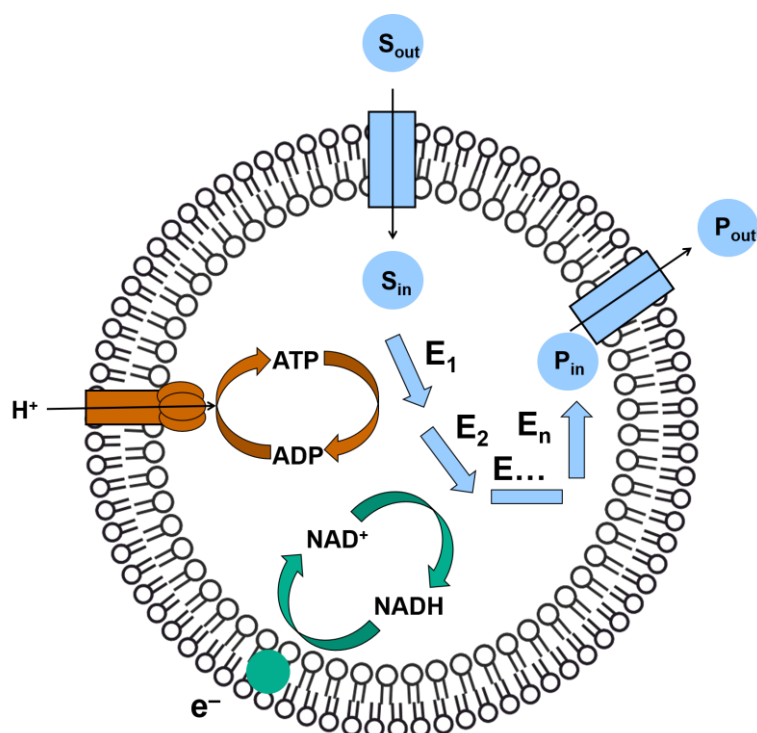


Figure 1.2 Scheme of a fictional synthetic cell designed within MaxSynBio in Magdeburg, consisting of an ATP energy regeneration module (orange), a NAD regeneration module (green), and metabolic enzymatic cascades (blue, S: substrate, E: enzyme, P: product) which are all included in a closed compartment (black).

1.4 Model membranes

As one of the basic components of the natural cell, the cell membrane is the barrier to the external environment. Therefore, one of the main steps to construct a synthetic cell from the bottom-up is to create a biomimetic compartment that uses membrane boundaries to separate distinct biochemical processes from each other²⁸⁻²⁹. In natural cells, the membrane consists of a lipid bilayer equipped with functional proteins to spatially or temporally regulate biological processes, according to the well-known fluid mosaic model introduced by Singer and Nicolson in 1972 (Figure 1.3)³⁰. The basic fluidic lipid bilayer is formed by self-assembly of amphiphilic lipids due to their non-covalent interactions depending on their molecular structure and temperature-defined phase formation behaviour. The term “mosaic structure”

comes from the functional proteins reconstituted in the lipid bilayer. These two main building blocks (proteins and lipids) define the bilayer stability, permeability, fluidity, and curvature³¹. In last decades, a great interest in developing many different types of lipid bilayer models was raised to investigate the functions of membrane systems³², such as free-standing black lipid membranes (BLMs)³³, supported lipid bilayers³⁴, and spherical vesicles³⁵. Moreover, with the flourishing development of polymer chemistry, not just natural and modified lipids, but also synthetic amphiphilic polymers with unlimited versatility are designed and used to form artificial membranes³⁶. All these models are further actively used in bottom-up synthetic biology to construct synthetic cells and their functional properties are studied in higher detail.

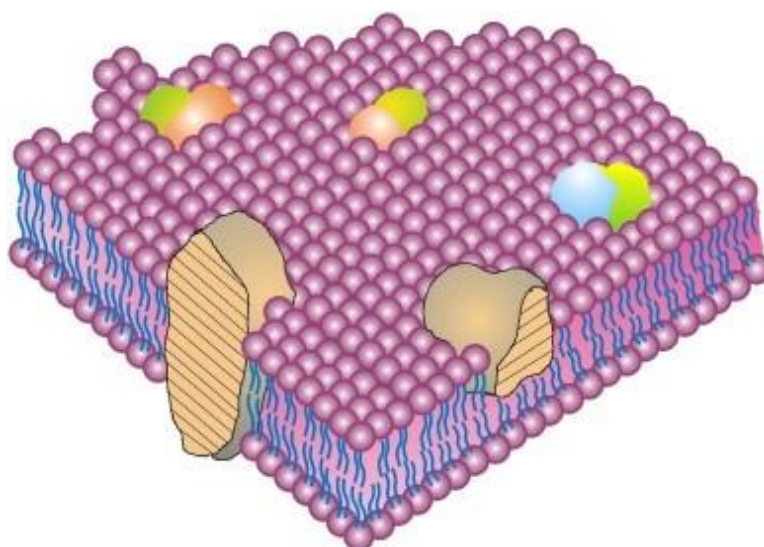


Figure 1.3 The fluid mosaic model of a natural membrane with the schematic three-dimensional cross-sectional view, adapted by G.L. Nicolson³⁷ from Singer and Nicolson³⁰.

1.5 Energy regeneration modules in synthetic cells

For the construction of a synthetic cell which can be seen as a biochemical reactor with optimal design, one important functionality is the continuous supply of energy and materials (Figure 1.2). The most abundant “energy currency” in cells is adenosine triphosphate (ATP). Concerning the ways how ATP is being regenerated, one can consult the natural blueprints. Apart from numerous examples of substrate-level phosphorylation, one of the main pathways

to produce ATP is based on the electron transport chain (ETC) in oxidative phosphorylation in the mitochondrial membrane or photosynthesis in the thylakoid membrane in eukaryotes or the plasma membrane of bacteria. This ETC process includes a series of membrane protein complexes that transfer electrons from electron donors to electron acceptors via redox reaction simultaneously releasing energy and pumping protons through the membrane and building proton gradients. These gradients activate ATP synthase to generate ATP from adenosine diphosphate (ADP). The main electron donors can be reduced forms of nicotinamide adenine dinucleotide (NAD), nicotinamide adenine dinucleotide phosphate (NADP), flavin adenine dinucleotide (FAD), or H_2O . Meanwhile, the electron acceptors can be oxidized forms of NAD, NADP, or O_2 . In the present work, we took inspiration from different ETC realizations and considered only NAD regeneration modules involving transmembrane electron transfer and ATP regeneration to power the synthetic cell. Such modules apply to two forms of NAD, namely oxidized (NAD^+) and reduced (NADH). Upon coupling with other modules, proton-pumping enzymes and ATP synthase, the NADH oxidation module can be used to construct an artificial mitochondrion³⁸ or NAD^+ reduction module for artificial photosynthesis³⁹ by mimicking the natural architectures⁴⁰⁻⁴¹.

1.6 NAD-dependent metabolism

As one of the hallmarks of life, the metabolism includes complex enzymatic reaction cascades. Aiming for a minimal synthetic cell, a simplified metabolic cascade including substrate, enzymes, and products is envisioned as shown in Figure 1.2. For instance, T. Erb and his colleagues designed an optimized synthetic CETCH (crotonyl-coenzyme A (CoA)/ethylmalonyl-CoA/hydroxybutyryl-CoA) cycle *in vitro* for continuous converting CO_2 into organic compounds which is more efficient than the natural carbon fixation pathway⁴². Furthermore, they encapsulated it into cell-sized droplets and coupled it with natural light-harvesting thylakoid membranes as ATP and NADPH regeneration modules to create an artificial photosynthesis system, mimicking the functionality of a chloroplast⁴³⁻⁴⁴. This example serves to demonstrate the utility of NAD regeneration and the modular approach discussed above. NAD has a vital role in metabolism in all forms of cellular life as it is required

as a cofactor in numerous biochemical reactions (around 360 NAD-dependent enzymes in total). These reactions involve oxidoreductases (e.g., cytosolic or membrane dehydrogenases), one of the largest classes of enzymes (~25% of all known enzymes). NAD is also a substrate in signaling and regulatory pathways in non-redox reactions⁴⁵⁻⁴⁸. Concerning the latter, NAD has been shown to be related to many important cellular processes, such as aging, cell death, degeneration, and gene expression⁴⁹⁻⁵³. For enzymatic biotechnology applications, and their high cost, stoichiometric NAD needs to be regenerated in a controlled manner via efficient and economical ways to enable continuous processes⁵⁴. This also applies to NAD⁺ and NADH, depending on the enzymatic reaction of interest (Figure 1.2).

1.7 NAD regeneration methods

There are several methods for NAD regeneration that can be grouped into enzymatic, chemical, electrochemical, and photochemical methods⁵⁵. Firstly, the enzymatic regeneration of NAD is fairly economic, quite selective, and environmentally friendly but primarily impeded by the stability of enzymes. Although engineered enzymes via mutagenesis strategies can potentially increase stability and efficiency, the cost of enzymes is relatively high, and their isolation is relatively complex. Chemical NAD regeneration may cost less, but it requires efficient catalysts for the redox reaction with high selectivity. Due to high consumption and potential pollution, some commonly used inorganic salts are therefore less recommended. Favorably, many organometallic complexes have been developed by functionally mimicking natural enzymes, such as metalloporphyrins⁵⁶, rhodium, iridium, and ruthenium-based complexes⁵⁷. In the case of NAD regeneration by electrochemical method, the volatile electrical energy is potentially available for broad applications. However, the overpotential of suitable electrodes with and without mediators is the main obstacle to obtain a sustainable process. Similar to the electrochemical method, NAD regeneration by photochemistry uses another orthogonal form of energy – solar. In nature, as mentioned, NADH can be regenerated by light-harvesting photosynthesis. In this regard, a self-assembled peptide nanotube was demonstrated to accelerate NADH regeneration under visible light⁵⁸. Inorganic TiO₂ nanoparticles were also shown to produce NADH with mediators while being encapsulated in

lipid vesicles⁵⁹. Moreover, synthetic polymer nanoparticles in polymer compartments were designed based on a conjugated microporous polymer containing benzooxadiazole for light-triggered NAD⁺ regeneration⁶⁰. Nevertheless, all these examples were not very efficient, especially in the visible light region, and relied on efficient photosensitizers and mediators. While enzymatic regeneration is still widely applied in chemoenzymatic synthesis, e.g., the historical method based on formate dehydrogenase⁶¹, suitable mediators for direct regeneration of NAD are sought in all other methods listed above to circumvent fragility of enzymes.

There are some plausible candidates that can act as electron mediators and catalysts of the NAD redox reaction, e.g., molecular wires⁶², ubiquinone⁶³, tetracyanoquinodimethane (TCNQ)⁶⁴, various phenoxazine and phenothiazine dye like methylene blue (MB)⁶⁵⁻⁶⁶ for the oxidation reaction. On the other side, reduction of NAD is still difficult to be tackled chemically and only a few metal complexes are known so far⁵⁷. Molecular wires, as the name suggests, are molecular chains, which bridge from the electron donor to the acceptor and are able to conduct electric current with typical non-linear current-voltage characteristics⁶⁷. Among them, a linear oligophenylenevinylene, named 1,4'-bis (4' - (N,N - bis (6' - (N',N',N'-trimethylammonium) hexyl) amino) - styryl) stilbene tetraiodide (DSSN) with a similar length as the bilayer lipid membrane was reported to increase the current via transmembrane charge transport (electron and/or ion) when being embedded in the bilayer membrane of living cells without significant toxicity⁶⁸⁻⁶⁹. In natural cells, one of the key electron transfer mediators in the mitochondrial respiratory chain is ubiquinone-10 (UQ), also known as coenzyme Q10, which acts inside the membrane in cohort with membrane enzymes (ETC complexes). In the field of electrochemistry, TCNQ as a prominent electron mediator being extensively used in electrodes⁷⁰, including the use as NADH sensor⁶⁴, can serve a conceptually similar role to UQ and directly oxidize NADH⁷¹. Besides, MB was shown to anaerobically oxidize NADH in a closed system⁷². These non-natural substances enable to build up NAD regeneration modules suitable for energy supply by ATP generation, and cofactor supply for NAD-dependent enzymatic reactions occurring in synthetic cells.

2 Aim of this work

The specific objective of this research work is to develop NAD regeneration modules for artificial cells to ensure its continuous supplement in a controllable way. Taking a minimal approach for the construction of such a module, we sought the simplest blueprint and most direct strategy to catalyze NAD^+/NADH redox reactions, entrapped inside the compartment, by external redox reagents (Figure 2.1).

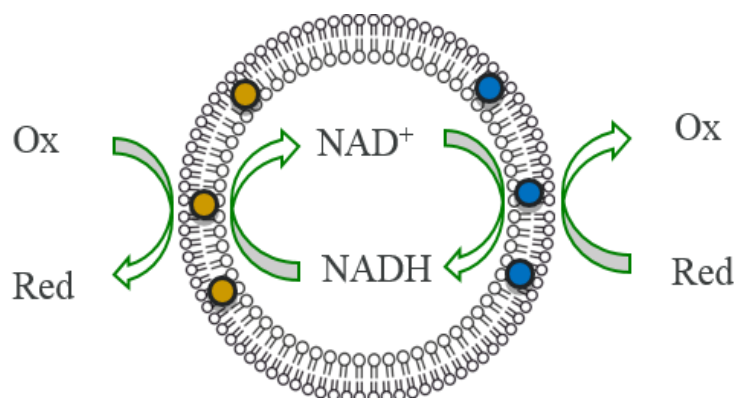


Figure 2. 1 Schematic illustration of a NAD regeneration module. (Yellow and blue circles indicate mediators).

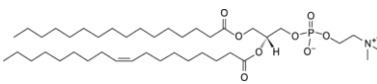
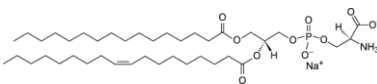
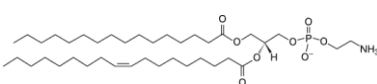
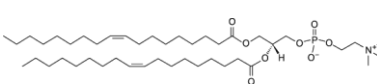
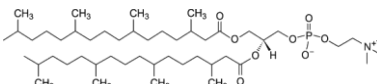
As already discussed, there are different compartments and configurations, serving as cell membrane models and different chemical candidates, and we explored some of them in a bottom-up approach, conceptually similar to piecing together different Lego bricks. The NAD^+ and NADH regeneration in BLM or vesicles were investigated based on DSSN, MB, TCNQ, or a rhodium complex. This work is largely structured based on the type of said synthetic compartments and significantly more focus has been given to the oxidation reaction. A summary of the used materials can be found in Chapter 3. NAD^+ regeneration in BLMs is presented and discussed in Chapter 4. Then in Chapter 5, an NAD^+ regeneration module based on TCNQ mediated transmembrane electron transfer was developed and studied in two size scales of vesicles (nm scale and micron scale) composed of natural lipids and/or a synthetic polymer. At last, in Chapter 6, an NADH regeneration module based on an organometallic complex was shortly addressed and discussed in nm scaled vesicles consisting of natural lipids.

3 Materials

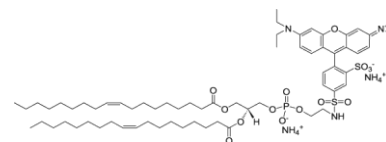
3.1 Amphiphiles

All lipids either as a powder or dissolved in chloroform were bought from Avanti Polar Lipids Inc.

Table 3.1 List of notations and basic properties of lipids used in this work.

Product	Abbreviation	Molecular Formula	MW (g mol ⁻¹)	Phase transition temperature (°C)	Molecular structure
1-Palmitoyl-2-oleoyl- <i>sn</i> -glycero-3-phosphocholine	POPC	C ₄₂ H ₈₂ NO ₈ P	760.076	-2	
1-Palmitoyl-2-oleoyl- <i>sn</i> -glycero-3-phospho-L-serine (sodium salt)	POPS	C ₄₀ H ₇₅ NO ₁₀ PNa	783.988	14	
1-Palmitoyl-2-oleoyl- <i>sn</i> -glycero-3-phosphoethanolamine	POPE	C ₃₉ H ₇₆ NO ₈ P	717.996	25	
1,2-Dioleoyl- <i>sn</i> -glycero-3-phosphocholine	DOPC	C ₄₄ H ₈₄ NO ₈ P	786.113	-17	
1,2-Diphytanoyl- <i>sn</i> -glycero-3-phosphocholine	DPhPC	C ₄₈ H ₉₆ NO ₈ P	846.252	-	

1,2-Dioleoyl- <i>sn</i> - glycero-3- phosphoethanolamine- N-(lissamine rhodamine B sulfonyl) (Ammonium Salt)	PE- Rho	C ₆₈ H ₁₀₉ N ₄ O 14PS ₂	1301.7 15
---	------------	--	--------------



Poly(dimethyl siloxane)-*g*-poly (ethylene oxide) (PDMS-*g*-PEO, MW 3000 g mol⁻¹, with an average degree of polymerization of 12 and 2 arms of PEO per PDMS chain) was donated by Dow Corning Inc. (Midland, MI, USA).

3.2 NAD

Nicotinamide adenine dinucleotide (NAD⁺) and its reduced form NADH-disodium salt were purchased from Carl Roth GmbH (Karlsruhe, Germany). The structures and redox reactions are shown in Figure 3.1.

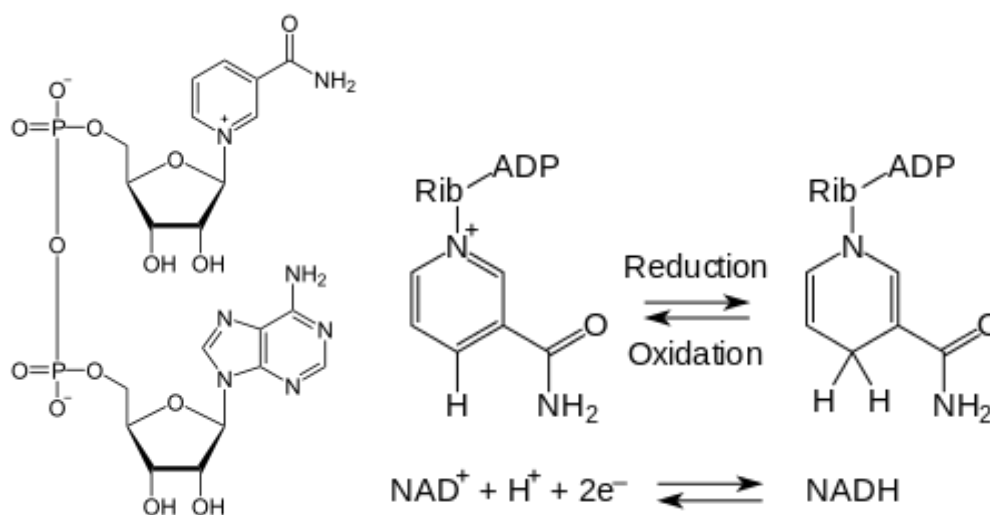
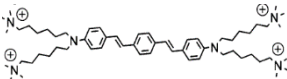
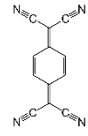
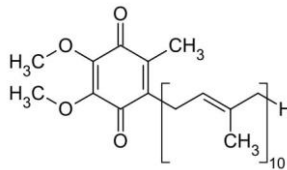
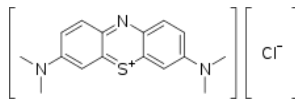


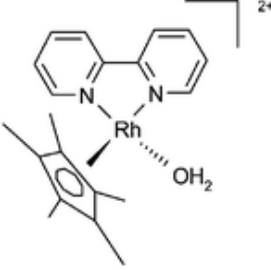
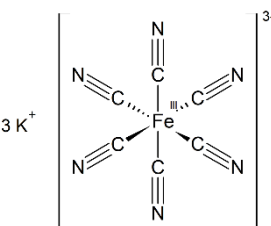
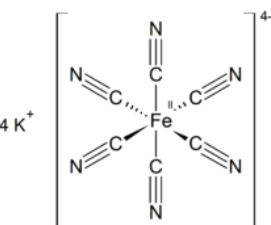
Figure 3.1 Structure of NAD⁺ (left) and the simplified structures showing the redox reaction of NAD⁺/ NADH (right).

3.3 Redox reagents

The list of redox reagents includes all the explored mediators and soluble electron agents.

Table 3.2 List of the information about mediators and other electron agents.

Product	Abbreviation	Molecular formula	MW (g mol ⁻¹)	Molecular structure	Supplier
1,4'-bis(4'-(N,N-bis(6'-(N',N',N'-Trimethylammonium) hexyl)amino)-styryl)stilbene tetraiodide	DSSN	C ₆₆ H ₁₀₆ N ₆ I ₄	1491.21		synthesized by partners from MPI-P
7,7,8,8-Tetracyanoquinodimethane	TCNQ	(NC) ₂ CC ₆ H ₄ C(CN) ₂	204.19		Sigma-Aldrich Chemie GmbH (Steinheim, Germany)
Ubiquinone-10	UQ	C ₅₉ H ₉₀ O ₄	863.365		
Methylene blue	MB	C ₁₆ H ₁₈ ClN ₃ S	319.85		

Pentamethylcyclopentenadienyl rhodium bipyridine complex	RhC	$[C_{10}H_{16} * Rh (C_5H_4N)_2Cl] Cl$ $[(Cp^*Rh(bpy)Cl) Cl]$	466.23		Synthesized by our group following the method from F. Hollmann ⁷³
Potassium ferricyanide	$[Fe(CN)_6]^{3-}$	$K_3Fe(CN)_6$	329.24		Merck KGaA (Darmstadt, Germany)
Potassium ferrocyanide	$[Fe(CN)_6]^{4-}$	$K_4Fe(CN)_6$	368.35		

3.4 Other chemicals

The chemicals in Table 3.3 were all purchased from Sigma-Aldrich Co.

Table 3.3 List of the information of all other chemicals.

Product	Molecular Formula	MW (g mol ⁻¹)
Agarose	C ₁₂ H ₁₈ O ₉	306.27
Carboxyfluorescein (CF)	C ₂₁ H ₁₂ O ₇	376.32

Chloroform	CHCl ₃	119.37
Ethanol	C ₂ H ₅ OH	46.07
Glucose	C ₆ H ₁₂ O ₆	180.156
<i>n</i> -Decane	C ₁₀ H ₂₂	142.286
3-N-Morpholino propansulfonic acid (MOPS)	C ₇ H ₁₅ NO ₄ S	209.26
LiTCNQ	C ₁₂ H ₄ N ₄ *Li	211.13
Methanol	CH ₃ OH	32.04
Nile red	C ₂₀ H ₁₈ N ₂ O ₂	318.369
Octyl glucose (OG)	C ₁₄ H ₂₈ O ₆	292.37
Potassium chloride	KCl	74.55
Sodium formate	HCOONa	68
Sucrose	C ₁₂ H ₂₂ O ₁₁	342.3

Gramicidin A from *Bacillus brevis* and α -hemolysin from *Staphylococcus aureus* were bought from Sigma-Aldrich Co.

Distilled water was obtained with the treatment in a Milli-Q water purification system (Millipore Corp.). All other chemicals were procured in analytic grade quality and used without further purification.

4 NAD⁺ regeneration in BLMs

Black lipid membranes (BLMs) or “painted” planar bilayers, introduced by Mueller and co-workers in 1962⁷⁴, are formed by the assembly of two opposing lipid monolayers spanning an aperture with a solvent annulus from a thin Teflon partitioning separating two aqueous chambers, as shown in Figure 4.1. They can be used as a model system of the natural cell membrane to study the trans-membrane currents upon application of voltage⁷⁵. To be specific, they allow simple electrical characterization of ion channels and peptide pores⁷⁶⁻⁷⁷.

BLMs are around 5 nm-thin bilayers, similar to natural membranes. They were opaque (black) due to the destructive interference with light reflecting off the front face. The two chambers separated by the bilayer are both accessible to electrodes, which also offers additional processing capability e.g., the addition of reagents to either the cis- or the trans-side. However, the limited lifetime and stability of the BLMs are still difficult to handle in practice.

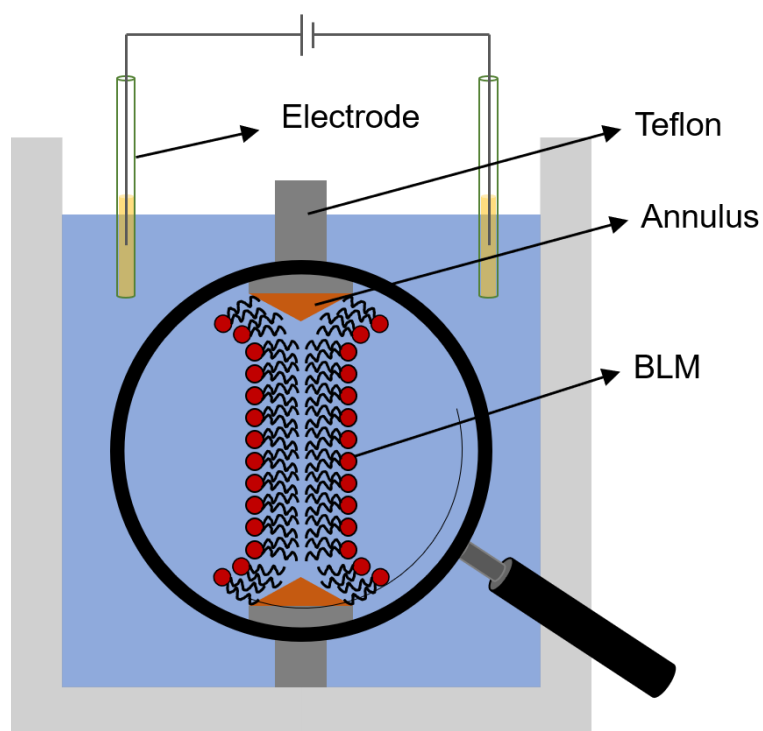


Figure 4.1 Schematic of a painted BLM in a chamber.

4.1 Amphiphile composition and modular blueprint of regeneration module

4.1.1 Phospholipids

Phospholipids, usually phosphoglycerides containing a hydrophilic head group and two hydrophobic acyl tail groups are the major natural amphiphiles forming the cell membrane. Their structural properties vary due to differences in the size and charge of the head group or length and saturation of the two acyl groups. Generally, the molecules of phosphoglycerides consist of a phosphate group, a glycerol unit, and two fatty acid tails (Figure 4.2). Based on the polar heads, phosphoglycerides can be classified as phosphatidylcholines (PC), phosphatidylethanolamines (PE), phosphatidylserines (PS), and phosphatidylinositols (PI)⁷⁸.

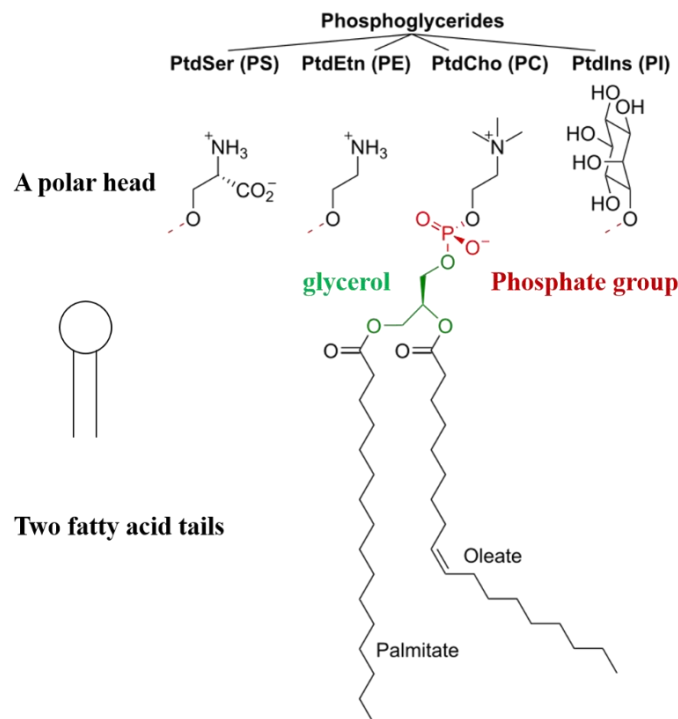
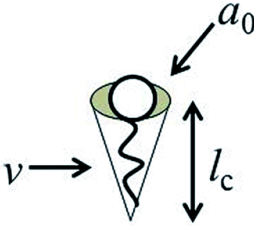


Figure 4.2 Molecular structures (right) of phosphoglycerides with palmitate and oleate tails and their schematic structure (left) indicating the hydrophilic head (a circle) and two hydrophobic tails (two lines) as the typical phospholipid able to form a lipid membrane.

When being dispersed in an aqueous solution with a proper concentration higher than their critical micellar concentration (CMC, the concentration at which micelles start to form), phospholipids will self-assemble and form a bilayer instead of a micelle, because of hydrophobic attraction of the two bulky and thick tails. Principally, the packing parameter (p) describes the ratio of a hydrophilic head and hydrophobic tails, and its value determines the type of the formed aggregate (Figure 4.3). The value of p is defined as:

$$p = \frac{V}{A * l}$$

where V is the volume of the hydrophobic portion of lipid, A is the area of the hydrophilic head group and l is the length of hydrophobic tails.



$$CPP = v/a_0 l_c$$




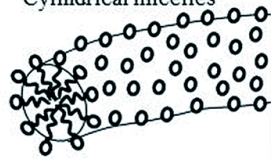

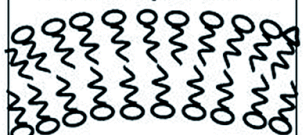



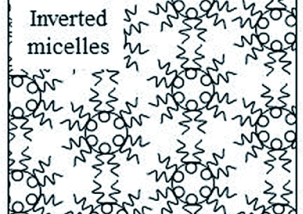
Critical Packing Parameter ($v/a_0 l_c$)	Critical Packing Shape	Structures Formed
$< 1/3$	 Cone	Spherical micelles 
$1/3 - 1/2$	 Truncated cone	Cylindrical micelles 
$1/2 - 1$	 Truncated cone	Flexible bilayers, vesicles 
~ 1	 Cylinder	Planar bilayers 
> 1	 Inverted truncated cone or wedge	Inverted micelles 

Figure 4.3 Molecular shapes and critical packing parameters of surfactants and lipids and the corresponding resulting structures⁷⁹.

For most natural phospholipids with one hydrophilic head and two hydrophobic tails (unlike other lipids such as simple fatty acids with only one tail that tend to form micelles), the packing parameters are mostly around $p \sim 1$ so that the formed membranes are typical bilayers (planar bilayers or vesicles).

Simultaneously, bilayers are also sensitive to temperature, pH, and ionic strength in the solution relating to their stability, fluidity, and permeability⁸⁰⁻⁸². Another major property of lipids is their physical state, which is particularly dependent on a critical temperature level, the so-called phase transition temperature (T_m) that defines the phase behaviour and permeability of bilayers⁸³⁻⁸⁴. When the temperature is lower than T_m , the lipid shows an ordered solid crystalline phase where the acyl tails are fully extended and closely packed. When the temperature is higher than T_m , the lipid is in the disordered liquid crystalline phase where the acyl tails are randomly oriented and thus fluidic. When the temperature is near T_m , the state of lipids can be liquid, ordered or disordered, and this state is affected by the neighboring lipids (Figure 4.4). As known, cholesterol, a solid and bulky lipid at physiological temperature, mainly interacts with other high fluidic phospholipids to increase the cell membrane packing.

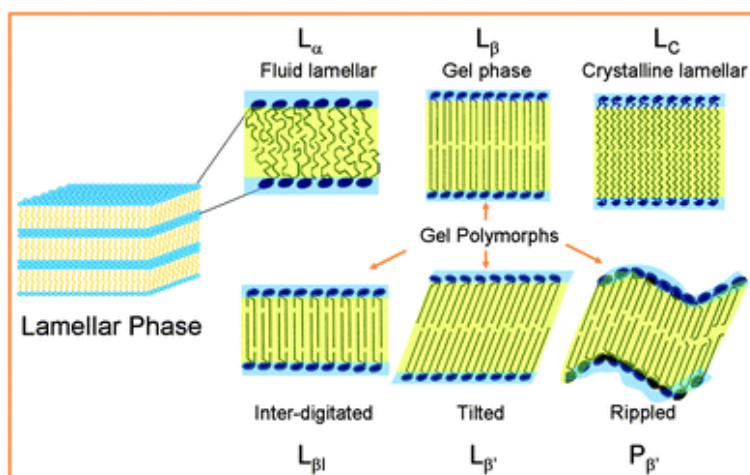


Figure 4.4 Commonly observed crystalline and liquid crystalline phases of lipids⁸³.

For easy processing and operating with experiments, usually, lipids with a T_m -value lower than room temperature are used to generate model membranes. As a commonly used and major component of natural membranes, POPC (Table 3.1) is used in this work. Furthermore, POPE and POPS are included to compensate POPC for BLMs formation. Then DPhPC which is reported to form more robust BLMs⁸⁵⁻⁸⁶ is also used for BLMs measurements.

4.1.2 Design of NAD⁺ regeneration module based on molecular wires

The NADH oxidation to NAD⁺ involves both electron and proton transfer (Figure 3.1), which also take place in the case of NADH dehydrogenase embedded in the membrane as complex I in ETC transferring electrons from NADH to UQ and simultaneously pumping protons across the membrane. To this end, BLMs provide a suitable experimental setup to build and investigate an NAD⁺ regeneration module, which essentially mimics the function of NADH dehydrogenase. In this scenario, conductive molecules that can transfer electrons and/or protons and oxidize NADH need to be included in the BLMs. Molecular wires are one such type of molecule that has attracted attention for electron transport through biomembranes. One of the first electron conducting molecular wires being incorporated into the vesicle membranes were caroviologens as transmembrane electron channels acting through conjugated charge transfer between two terminal electroactive polar groups⁶². A conjugated oligoelectrolyte: linear oligophenylenevinylene with conductive π -delocalized backbone named DSSN, was reported to increase charge collection when incorporated in bilayer membrane^{68-69, 87}. Additionally, when being associated with microbial membranes, they showed no lethal side effects, enhanced current generation, and removal of the organic contaminant in wastewater microbial fuel cells⁸⁸. Although the mechanism is still not completely understood, DSSN is apparently conductive and increases the charge transfer to the electrode. To determine its ion conductivity, electrophysiologic measurements were used to analyze the functionality of DSSN-incorporated BLMs. Since the DSSN molecule cannot catalyze the NAD⁺/NADH reaction (redox potential: -320 mV at standard conditions, 25 °C and pH 7)⁸⁹, a detectable mediator, methylene blue (MB, redox potential around 0.01 V at pH 7)⁹⁰, which can oxidize NADH, is envisioned to be associated to DSSN to construct a NAD⁺ regeneration module (Figure 4.5).

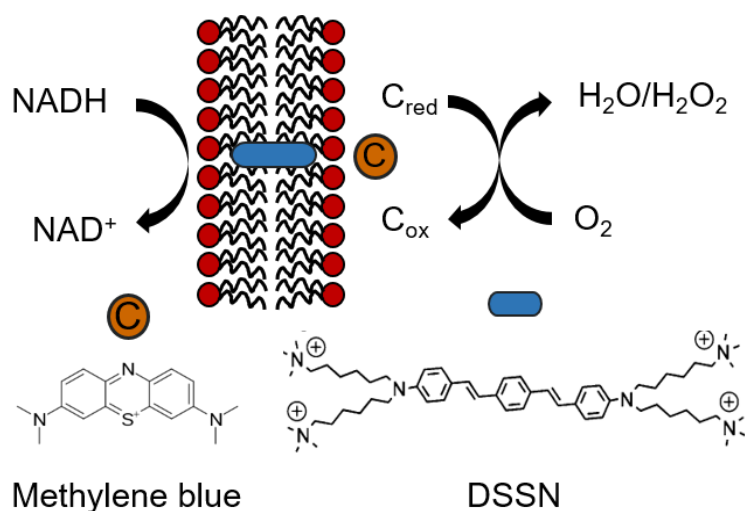


Figure 4.5 Schematic illustration of NAD⁺ regeneration in BLMs by incorporation of DSSN and methylene blue as catalytic mediator (C).

4.2 Experimental details

4.2.1 Oxidation of NADH with MB

NADH is intrinsically fluorescent, showing an absorption peak at 340 nm (with a molar extinction coefficient of $6220 \text{ M}^{-1} \text{ cm}^{-1}$) and an emission peak at 460 nm while NAD⁺ is not. As a result, NADH oxidation by methylene blue (MB) was determined by quantifying the amount of NADH via absorption spectra scanning using the SPECORD 50 PLUS UV/Vis spectrophotometer (Analytik Jena AG, Germany). The process of NADH oxidation was monitored in MOPS buffer (100 mM MOPS, 250 mM KCl, Tris, pH 7.2) by UV/Vis spectra and fluorescence intensity analysis operated on the 96-well plate reader from Synergy HT (BioTek, Winooski, VT, USA).

4.2.2 Method for BLM study

The planar black lipid bilayer membranes were formed and studied using Ionovation Bilayer scout from Ionovation GmbH (Osnabrück, Germany). The setup includes a Patchmaster software for programming and recording, EPC 10 amplifier (HEKA, Lambrecht/Pfalz, Germany) for amplifying signals, a pump system, a carriage, and a controller for BLM formation (Figure 4.6). The corresponding programs from Patchmaster software are specifically designed to fit our study.

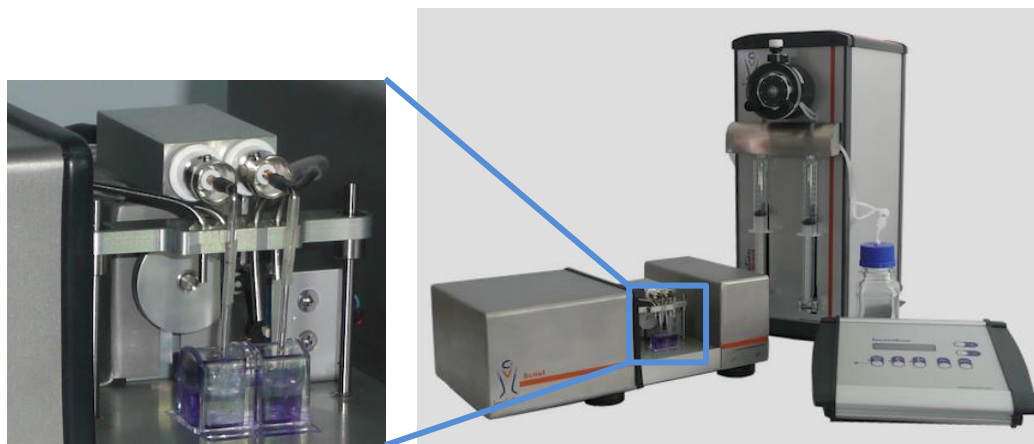


Figure 4.6 Testing chamber (left) and bilayer scout device (right) from Ionovation GmbH.

In order to study the current and conductivity of mediators, a stable BLM needs to be created. Firstly, the Ag/AgCl electrodes were pretreated for use by immersing into highly concentrated KCl solution (3 M) filled glass rods which contained dissolved agarose (1% in 3 M KCl buffered solution) in the head, and then connected with the headstage. After being filled with water, the test chamber was placed in the carriage and perfused with 250 mM KCl buffer to prepare a short circuit. For the preparation of a planar lipid bilayer, 0.2 μL of 10 mg mL^{-1} lipids composed of POPC/POPE/POPS (8:1:1 wt%) or DPhPC dissolved in *n*-decane were injected by microliter syringe onto the aperture (with a diameter of 120 μm) between the left and right chambers. By executing the protocol “Autobilayer”, which draws the buffer in one of the channels and pushes it back in order to paint the lipids onto the aperture, then stable lipid

bilayer (BLM) is formed with a capacitance around 45 pF and a membrane resistance of 1.4 GOhm. A typical recording of a lipid bilayer membrane formed is shown in Figure 4.7.

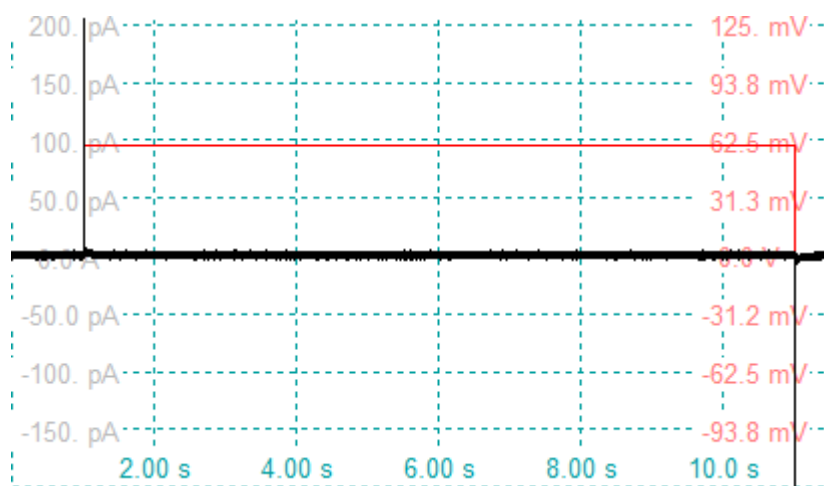


Figure 4.7 Screenshot of current profile (in black) of a stable black lipid membrane (BLM) prepared by POPC/POPE/POPS (8:1:1 wt%) with a constant applied voltage (in red) of 60 mV shown in Patchmaster.

After that, an aliquot of gramicidin A (GA) or hemolysin as test pore-forming membrane proteins, or molecular wires (DSSN) dissolved in ethanol were added to the bilayer through injection close to the aperture and incubated for some minutes. By a properly defined protocol that applies different voltages to the chamber, the current change was recorded, and respectively the conductance was automatically calculated.

4.2.3 NAD⁺ regeneration in DSSN based BLMs

As mentioned before, a DSSN-based NAD⁺ regeneration module would require a redox-active moiety like MB associated or covalently linked to DSSN in BLMs that would oxidize NADH and transfer electrons through the BLMs. Thereby, we intentionally aimed for mediators being embedded in the membrane with NADH staying on one side of the membranes and oxidants staying on the other side (Figure 4.5). DSSN's presence in the lipid membrane

was confirmed by its intrinsic fluorescence. DSSN was embedded into POPC lipid suspensions and imaged on an Axio imager A1 microscope (Carl Zeiss, Germany). Herein, DSSN in the MOPS buffer was first detected at different concentrations and their UV/Vis spectra and fluorescence intensity were recorded with a plate reader on Synergy HT. Then, an adequate concentration of DSSN was embedded into POPC suspensions prepared by gentle hydration for imaging under the respective wavelength. Briefly, 5 μmol POPC lipids in chloroform were mixed with DSSN dissolved in ethanol in a glass tube and the solvent was then removed under gentle nitrogen purging and vacuum for 2 h. Afterward, the dry film was hydrated with 500 μL MOPS buffer (100 mM MOPS, 250 mM KCl, Tris, pH 7.2) and vortexed for imaging.

At last, the process of NAD^+ regeneration was studied by monitoring both conductivity of MB associated DSSN in BLMs in the electrophysiological setup and the NADH fluorescence intensity.

4.3 Oxidation of NADH with MB

As described previously, MB can oxidize NADH and be reduced to its colorless form (MBH). The MBH can then be further oxidized by an electron acceptor like O_2 (Figure 4.5). As shown in Figure 4.8, NADH absorbs at 340 nm, while NAD^+ and MB do not. When mixed with a lower concentration of MB (NADH to MB 15:1) while purging the sample with pure oxygen, the absorption peak (340 nm) corresponding to NADH decreased.

To observe the change of NADH oxidized by MB with a molar ratio of NADH to MB at 3:1, the variation of NADH absorbance at 340 nm, MB absorbance at the wavelength of 609 nm and 665 nm, and the NADH fluorescence intensity with an excitation wavelength of 360 nm and emission wavelength of 460 nm were recorded in the open air (oxygen), as shown in Figure 4.9. Meanwhile, the absorbance of MB at the two relevant wavelengths decreased when being added to NADH solution in a three-fold higher ratio than MB and recovered slowly with the oxygen in the air. Nonetheless, the process was slow, and it took around 1 h for 50% of NADH to be oxidized. This rate is important for the experimental design in BLMs and will be discussed in the next section.

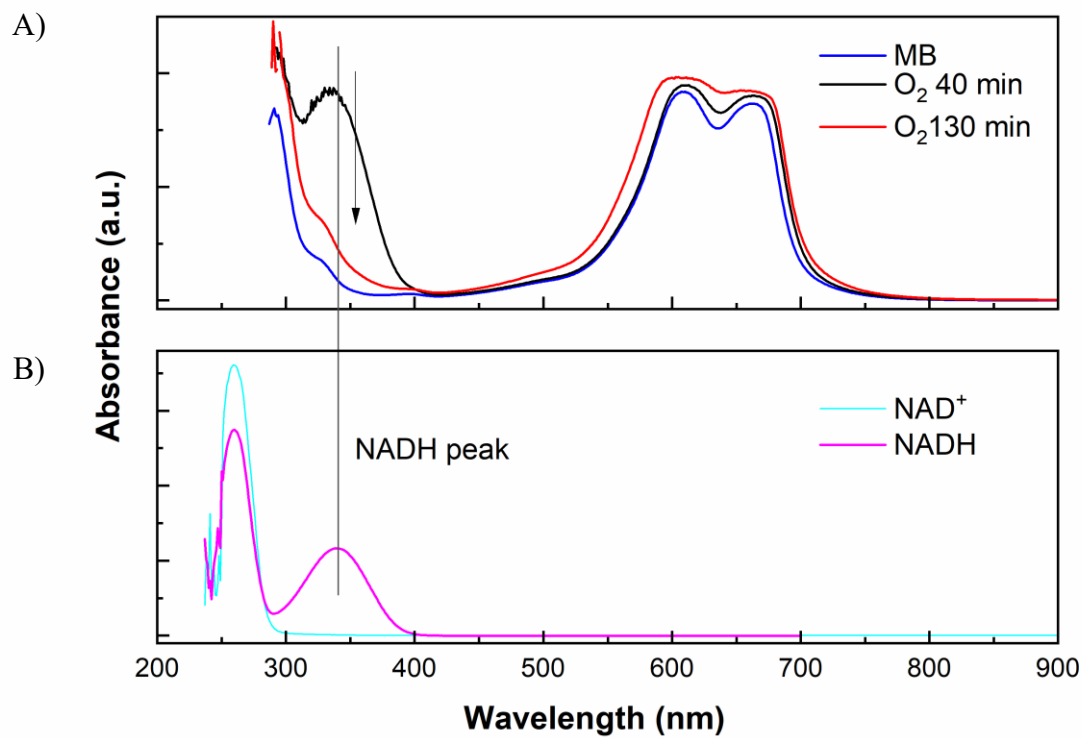


Figure 4.8 UV/Vis spectra of NAD⁺ (B, magenta), NADH (B, cyan), methylene blue (MB, A, blue), and MB mixed with NADH for 40 min (A, black) and 130 min (A, red) after purging with oxygen (with a molar ratio of NADH to MB = 15:1).

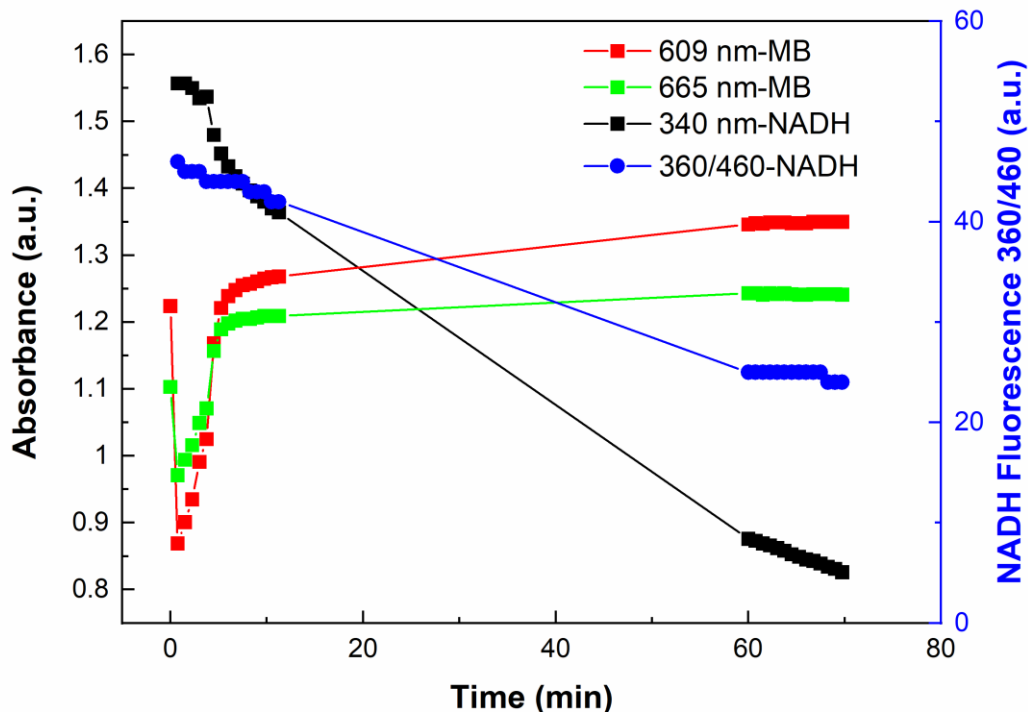


Figure 4.9 Time courses of absorbance of NADH (black, at 340 nm), methylene blue (MB, red, at 609 nm, and green, 665 nm) and fluorescence intensity of NADH (blue, $\lambda_{\text{ex}} = 340$ nm, $\lambda_{\text{em}} = 460$ nm), (right, blue) in the open air (with a molar ratio of NADH to MB = 3:1).

4.4 Conductance studies in the BLM setup

By the voltage-clamp technique, one can record the current, capacitance, and conductance change of BLMs upon application of different voltage inputs. The current changes of different BLMs composed of natural lipids POPC/POPE/POPS (8:1:1 wt%) responding to the set voltage change are shown in Figure 4.10. The current change of both tested ion channels, gramicidin A (GA) and hemolysin were stable and exhibited a linear dependence on the applied voltage. For the molecular wire (DSSN), the current was similarly responding to the voltage, though it was lower than with the ion channels. This indicated that DSSN was able to improve

the membrane ion conductivity⁹¹, but also probably perturbed and deformed the same membrane⁹². The detailed current change with time for BLMs with 5 μM DSSN embedded when being applied with a voltage of 40 mV and -40 mV showed transient current (Figure 4.11), suggesting that DSSN diffuses within the lipids and makes pores in a similar way how GA acts. Such poration activity indicated that DSSN would be possibly disruptive for BLMs and cause ion leakage. Considering the nonlinear current change, especially that the current was less stable at higher voltage (> 70 mV or < -90 mV), we used DPhPC which is known to form more robust BLMs for further DSSN measurements⁸⁵⁻⁸⁶.

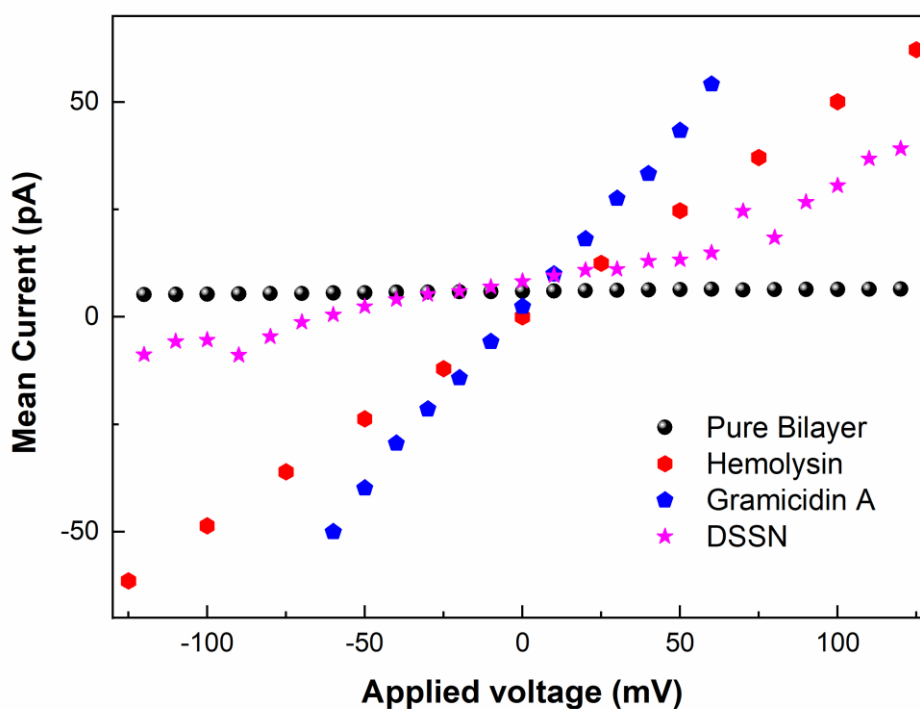


Figure 4.10 Mean current change responding to the applied voltage change of different BLMs (consist of POPC/POPE/POPS 8:1:1 wt%): pure bilayer, BLMs with embedded hemolysin, gramicidin A and DSSN.

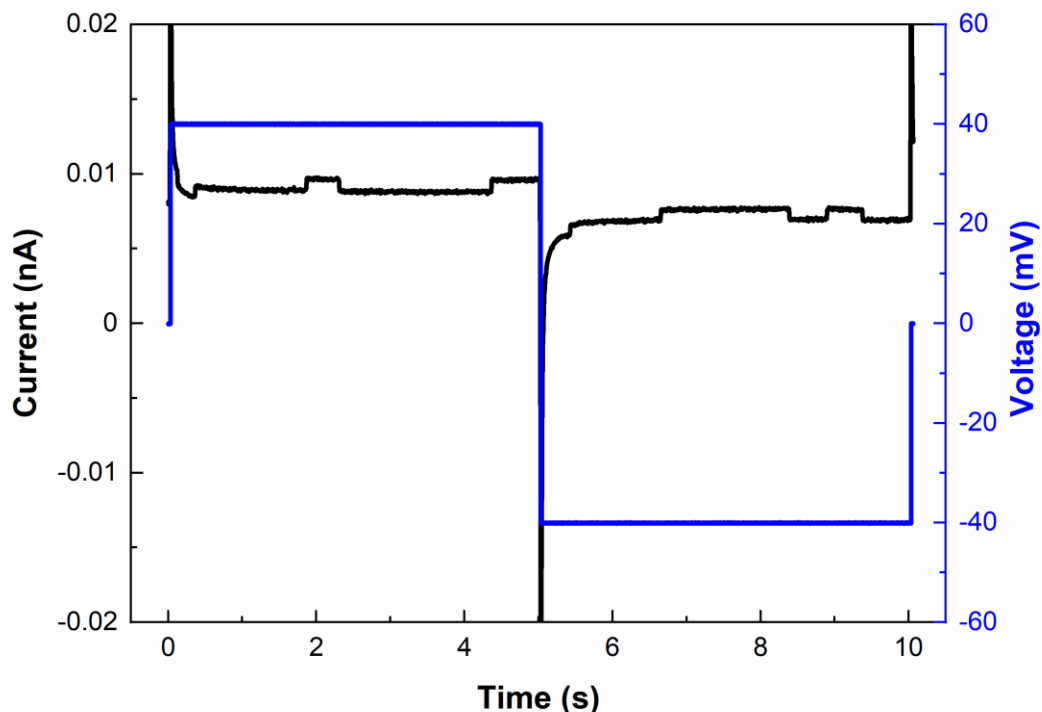


Figure 4.11 Current and voltage change of BLMs consisting of POPC/POPE/POPS 8:1:1 wt%, with 5 μM DSSN embedded, monitored over time.

In order to obtain more details about the ionic conductivity and the apparent “poration”, increasing concentrations of DSSN were tested in the DPhPC BLM in the range of voltages from -60 mV to 60 mV with an increment of 10 mV. The current changes were linearly responding to the applied voltage (Figure 4.12). Moreover, at a higher concentration of DSSN embedded in BLMs, the current change was larger. Correspondingly, the conductance changes followed the same trend (Figure 4.13). With 20 μM DSSN embedded in BLMs, the conductance and capacitance were monitored over time (Figure 4.14). These results have confirmed that DSSN increased the ionic conductivity and permeability as also demonstrated in *E. coli*⁹³. In addition, the conductance decreased after 50 min which indicated that the stability of BLMs with DSSN might not last long enough especially for later NADH oxidation (Figure 4.9).

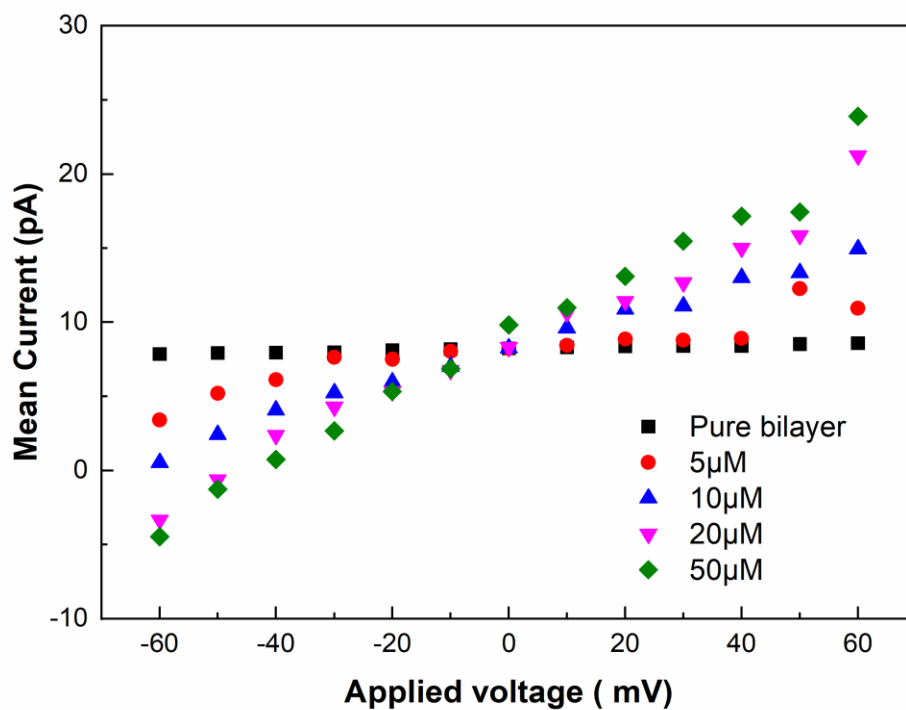


Figure 4.12 Mean current change responding to the applied voltage change of DPhPC BLMs with different concentrations of embedded DSSN: 0 (pure bilayer), 5 μM , 10 μM , 20 μM , and 50 μM .

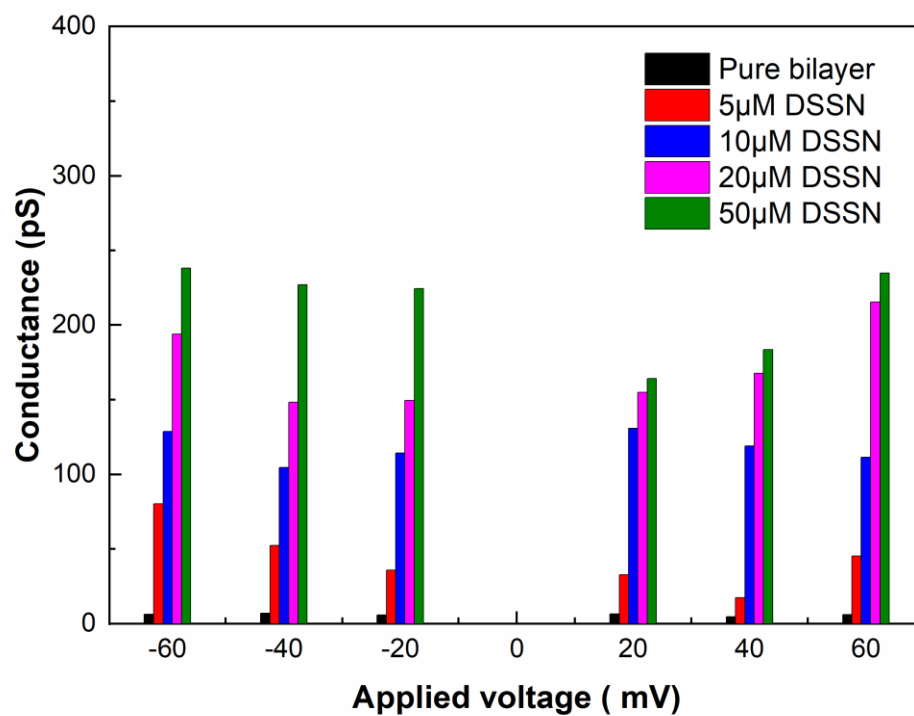


Figure 4.13 Mean conductance change responding to the applied voltage change of DPhPC BLMs with different concentrations of embedded DSSN: 0 (pure bilayer), 5 μM, 10 μM, 20 μM, and 50 μM.

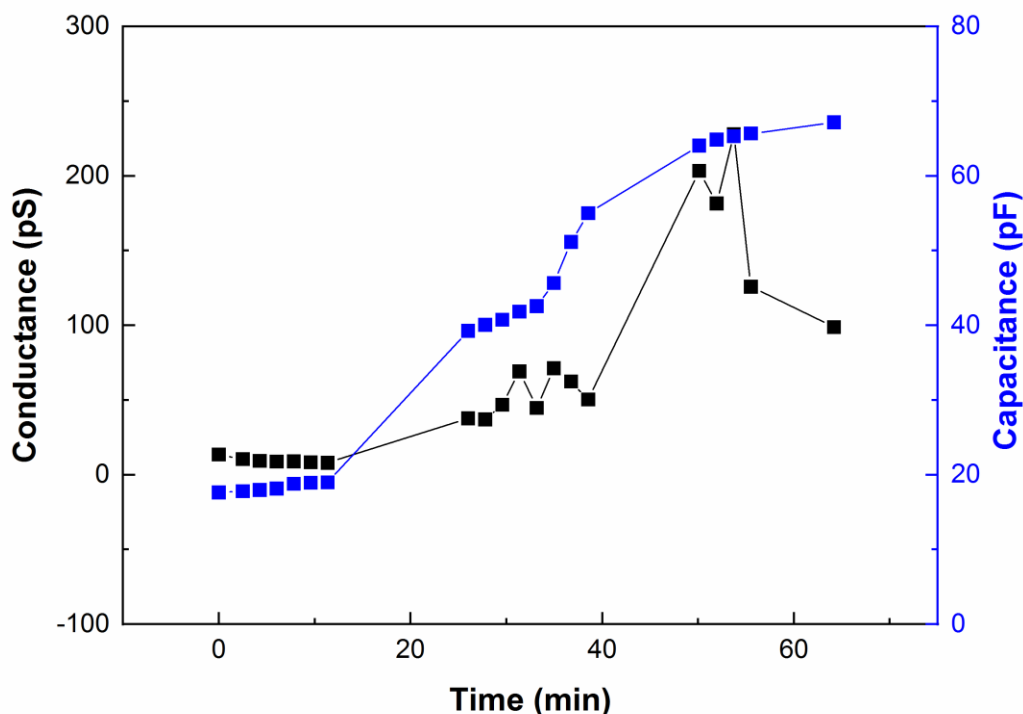


Figure 4.14 Conductance and capacitance change of DPhPC BLMs, with 20 μ M DSSN embedded, monitored over time.

4.5 Prospects for NAD⁺ regeneration studies in BLMs

As mentioned above, DSSN as a conductive mediator used for NAD⁺ regeneration was initially considered as a plausible candidate to transfer electrons and oxidize NADH in BLMs when being associated with the catalyst MB. In order to confirm the embedding of DSSN on the lipid membrane, DSSN, as fluorescent dye⁹⁴, was embedded in POPC suspensions and imaged by fluorescence microscopy. Firstly, as shown in Figure 4.15, DSSN contributed an absorption peak at around 405 nm and its absorbance increased with higher concentration. Accordingly, the fluorescent intensity of DSSN detected on the microplate reader with a fixed light filter (excitation wavelength at 485 nm and emission wavelength at 590 nm) was linear and increased with increasing concentrations (Figure 4.16). Following the information above,

the fluorescent image, given in Figure 4.17, indicates the successful localization of DSSN in the POPC membrane.

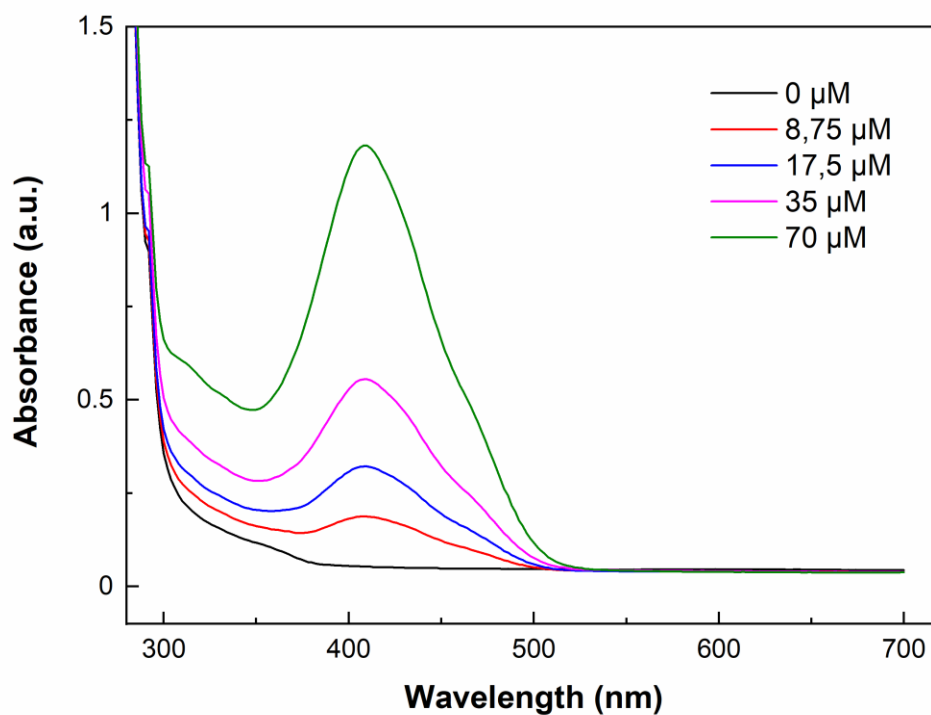


Figure 4.15 UV/Vis spectra of DSSN at different concentrations.

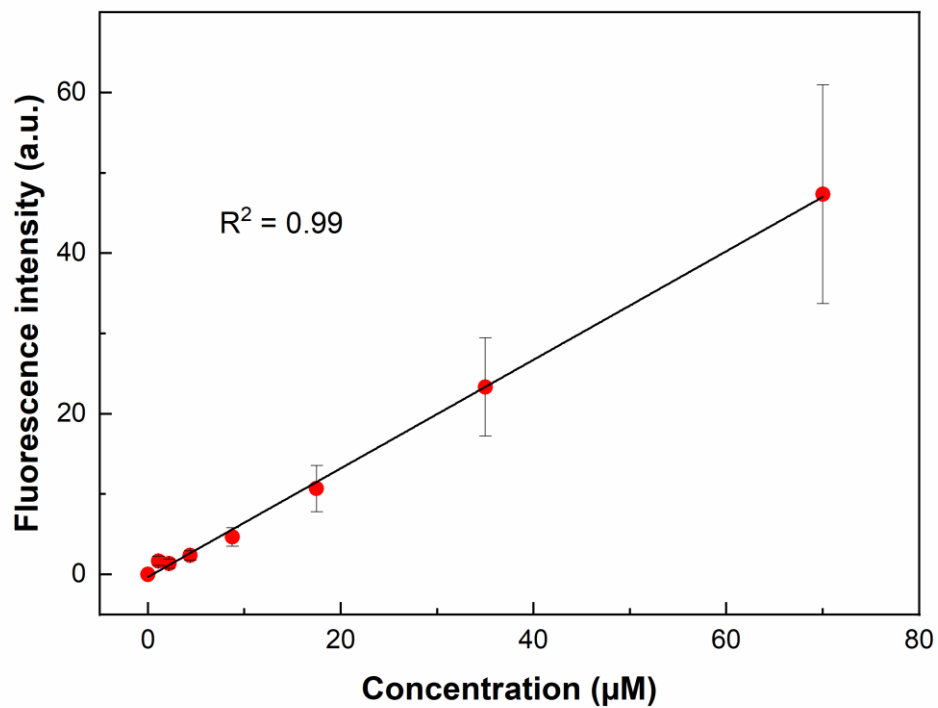


Figure 4.16 Fluorescence intensity versus DSSN concentration (λ_{EX} : 485 nm, λ_{EM} : 590 nm).

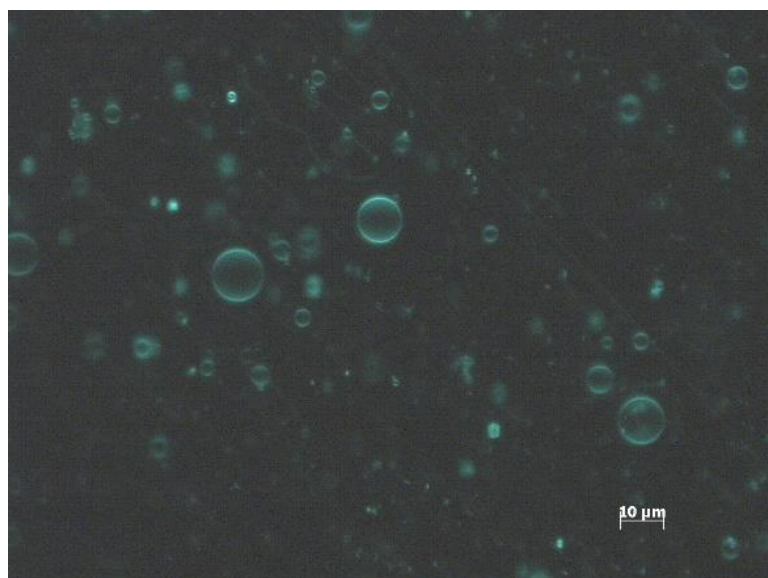


Figure 4.17 Fluorescent image of DSSN embedded in POPC suspensions.

With the aim of building up a simplified NAD⁺ regeneration module in BLMs, DSSN provided an apparently straightforward strategy to study electron transfer through lipid membranes. Despite that, in the view of the effectiveness of BLMs formed in a 120 μm aperture comparing with ca. 1 mM NADH in the chamber, the limited stability of BLMs with DSSN and the low efficiency of MB for oxidation of NADH as shown in the results above, the regeneration module of NAD⁺ with DSSN in BLMs turned out as not practical to study further at this point. Here, we confirmed that DSSN increases the ionic conductivity of the membrane. This is related to the previously speculated poration of the bilayer that would potentially release soluble endogenous mediators from living cells⁹³ and is in line with results from molecular simulations⁹². The observed ionic conductivity may be detrimental to the overall bioenergetic scenario since it may lead to dissipation of pH gradients and thus prevent ATP synthesis, however, we do not have sufficient information about the size and lifetime of these pores. The electrophysiological behaviour actually suggests that the pores are only transiently formed, and we assume that the membrane can be still sufficiently intact to retain encapsulated proteins. This in turn would direct the application toward purely bioreactor scenarios and may even provide a mechanism for small molecule exchange across the membrane, while keeping the catalytic machinery, i.e., cytosolic dehydrogenases inside the synthetic cells. On the other side, the limited possibility for reaction detection in the current setup can be alleviated, for instance, by the use of a horizontal BLM setup with smaller chamber volumes, which would enable quantitative analysis of the cis- and trans-solutions. Such a horizontal setup would also enable integration with microscopy to directly monitor the presence of DSSN in the membrane. Nevertheless, we decided to abandon this model setup and to continue with vesicular assemblies, which represent another type of model membranes but are conceptually more similar to natural cells, while further improvement of the electrophysiological setup may still allow for detailed studies with molecular wires and other transmembrane architectures.

5 NAD⁺ regeneration in vesicles

Vesicles, which are spherical structures, often practically applied as drug delivery systems, now are also extensively used as a model to establish synthetic cells. They have an aqueous core and phospholipid bilayer, acting as a barrier just like the cell membrane and are segregating enzymatic reactions from the outside environment⁹⁵⁻⁹⁶. Vesicles can be classified based on the number and organization of their membrane – multilamellar vesicles (MLVs), unilamellar vesicles (UVs), multi-vesicular vesicles (MVs) (Figure 5.1)⁹⁷. Due to the hydrophobic interaction of the amphiphiles, they spontaneously assemble to spherical structures, which are mostly MLVs, as soon as being hydrated in an aqueous solution. Using sonication or extrusion through a membrane filter⁹⁸, MLVs can be broken into UVs to reduce their lamellarity, and UVs are typically used as cell models. With respect to their size, UVs can be further classified into small UVs (SUVs, 50–100 nm), large UVs (LUVs, 100 nm–1 μ m), and giant UVs (GUVs, > 1 μ m). The resulting size of UVs can be controlled with different preparation techniques⁹⁹. Monodisperse SUVs and LUVs are usually prepared by extrusion through a polycarbonate filter with a defined pore size by re-hydration of a dry amphiphiles film formed after evaporation of organic solvent⁹⁸. As for GUVs, they can be generated by gentle hydration, electroformation, microfluidics, double emulsions, etc.¹⁰⁰⁻¹⁰¹ Gentle hydration of amphiphiles could indeed produce GUVs, yet with a significant fraction of MLVs, which is not feasible for a transmembrane activity study. In the case of microfluidics and double emulsions, amphiphiles which are firstly dissolved in an organic solvent for better dispersion would be used directly without drying to mix with an aqueous solution which results in forming emulsions at last. Further removal of the organic solvent is needed, which would easily burst GUVs. Therefore, we used the electroformation method by hydration of the dried (solvent-free) amphiphilic film by application of an electrical field, which is an established method for GUVs preparation for studying membrane phenomena. For SUVs and LUVs, one of the main advantages with respect to the current study is their relatively longer lifetime than BLMs and GUVs, which can span days or even weeks during storage at suitable temperatures and conditions. Though GUVs are gaining an increasing role as cell models due to the same size scale as many natural cells and the microscopic accessibility.

In synthetic biology, synthetic UVs can be formed with different amphiphiles including natural lipids and also synthetic amphiphilic polymers, and these UVs are used as minimal cell models to mimic the natural complex membranes¹⁰². The resulting vesicles are called lipid vesicles (also called liposomes), lipid/polymer hybrid vesicles, and polymer vesicles (also called polymersomes) respectively. The different compositions are discussed in more detail in the following section.

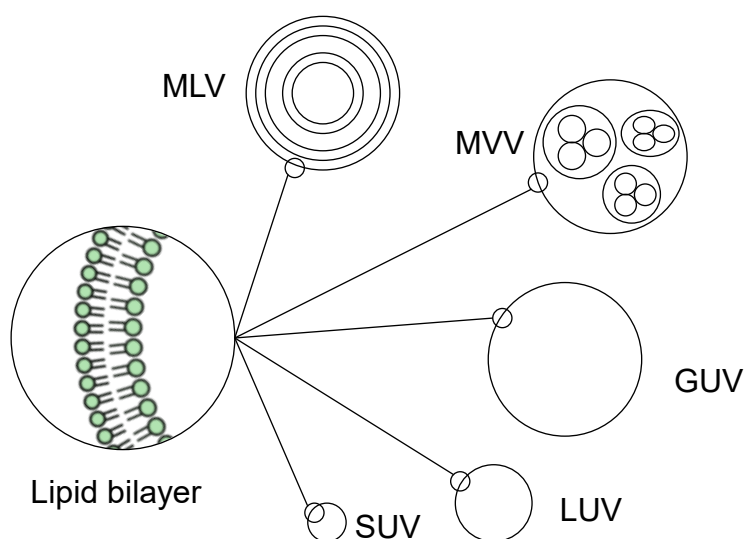


Figure 5.1 Lipid bilayer structure and types of vesicles⁹⁷.

5.1 Amphiphile compositions and architecture of the regeneration module

5.1.1 Amphiphiles

Different pure lipids or mixtures of lipids are used for vesicles formation. Despite their polymorphism and diversity, natural lipids are already well studied, yet they exhibit certain limitations for building up synthetic compartments like possible oxidation and the formation of more permeable and less stable bilayer membranes, which qualities are especially relevant

for the studies about membrane phenomena¹⁰³. In this context, synthetic chemistry provides opportunities to introduce optimized versatile materials: amphiphilic copolymers.

In recent years, amphiphilic copolymers have gained increasing interest in the construction of synthetic membrane (lipid/polymer hybrid vesicles or polymersomes) mainly due to their low cost, controllability, and flexibility to be designed for multi-functional application in biotechnology and bioengineering¹⁰². The type of the polymer, for instance, its molecular weight or the hydrophilic/hydrophobic blocks ratio influences the physical and chemical properties of the resulting vesicles. The early reported synthetic block copolymers used to prepare polymersomes were based on polyethyleneoxide-polyethylethylene (EO₄₀-EE₃₇), and the respective membranes were more stable and less permeable to water than natural phospholipid bilayers¹⁰⁴. Such copolymer is typically formed with block or grafted architecture, comprising mostly PEO as the hydrophilic component and other hydrophobic polymers such as poly(dimethyl siloxane) (PDMS), poly(isobutylene), and polybutadiene, etc. as the hydrophobic backbone¹⁰⁵⁻¹⁰⁶. Furthermore, the blending of polymers with natural lipids offers higher flexibility of physicochemical characteristics than pure liposomes and polymersomes. Because of a lower glass transition temperature ($-125\text{ }^{\circ}\text{C}$), PDMS is often used to prepare fluidic hybrid membranes. Moreover, PDMS presents low Hildebrand solubility parameters ($\delta = 7.3\text{ cal}^{1/2}\text{ cm}^{-3/2}$), which are compatible with the fatty acid groups in phospholipids ($\delta = 9.1\text{ cal}^{1/2}\text{ cm}^{-3/2}$) so that it will be therefore more miscible to the phospholipid membrane. Here, we selected PDMS-g-PEO (a grafted polymer) that forms ca. 5 nm-thick monolayers similar to the thickness of natural phospholipid bilayers¹⁰⁷, which also exhibited sufficient fluidity at room temperature (diffusion coefficient of $\sim 3.6\text{ }\mu\text{m}^2\text{ s}^{-1}$ while the value of natural lipids lies at $\sim 10\text{ }\mu\text{m}^2\text{ s}^{-1}$) (Figure 5.2)^{38, 108}. The thickness of polymer vesicles is important for the functional study of membrane phenomena particularly with membrane proteins¹⁰⁹. Moreover, flexible polymers are shown to interact with lipid bilayers and affect their fluidity, curvature, permeability, and stability which brings a promising future to design controlled biomimetic membranes¹¹⁰.

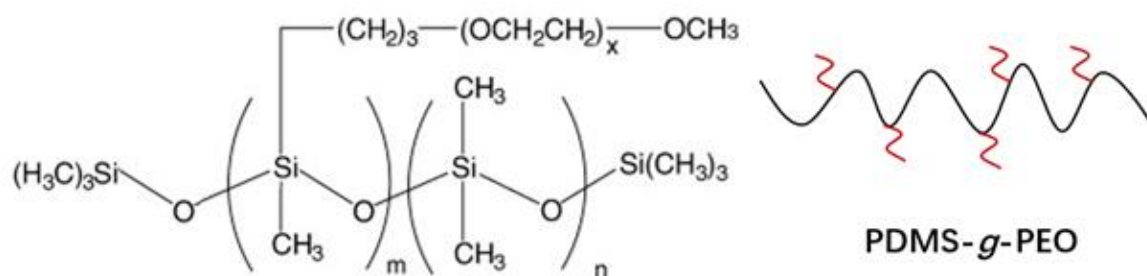


Figure 5.2 Molecular structure (left) of PDMS-*g*-PEO and its schematic structure (right) indicates hydrophilic head (red) and hydrophobic backbones (black).

5.1.2 Blueprint of the vesicular NAD⁺ regeneration module

In the past, transmembrane electron transfer studies were mainly focused on photosynthetic and oxidative phosphorylation processes¹¹¹. In the cellular respiratory chain, UQ acts as an electron transfer mediator within the hydrophobic region of lipid membranes and is coupled with the mitochondrial NADH dehydrogenase (Complex I) and other ETC complexes (Figure 5.3 A). In addition, when being reconstituted in a bilayer lipid membrane UQ was reported to mediate the electron transfer with NADH, as detected by electrochemical impedance spectroscopy and cyclic voltammetry⁶³. Schiffrein *et al.* also investigated the transmembrane electron transfer by UQ through phospholipid bilayer membranes using patch-clamp micropipette techniques and reported a transfer coefficient of 0.5, coupled with Fe(II)/Fe(III) citrate¹¹². On the other side, when being embedded in a biomimetic hybrid lipid bilayer, UQ was mediating reversible redox conversions of NADH and NAD⁺, as confirmed by voltammetry studies¹¹³⁻¹¹⁴. Similarly, tetracyanoquinodimethane (TCNQ) has been shown to mediate electron transfer from ascorbate encapsulated in liposomes to external ferricyanide¹¹⁵, from ions in one side of BLMs and ferricyanide on the other side¹¹⁶ or by coupling with TTF supported bilayers¹¹⁷. Moreover, TCNQ has also been used to modify electrodes and applied as an NADH sensor⁶⁴. To our knowledge, none of the work was done to combine the study of the transmembrane electron transfer by UQ or TCNQ and directly oxidizing NADH on freely suspended vesicles. Therefore, we developed a straightforward

method for direct regeneration of NAD^+ via transmembrane electron transfer mediated by TCNQ¹¹⁸. Thereby, we simplified the electron transfer process and oxidized encapsulated NADH in a controlled manner which scenario can be potentially used to activate a proton pump protein (and thus ATP synthase to regenerate ATP³⁸) and to directly power NAD^+ -dependent reactions inside synthetic cells (Figure 5.3 B) alongside our overall motivation discussed above. This module was studied in different compartments with different compositions (lipid/polymer) and at different size scales (hundreds of nm, LUVs and tens of microns, GUVs).

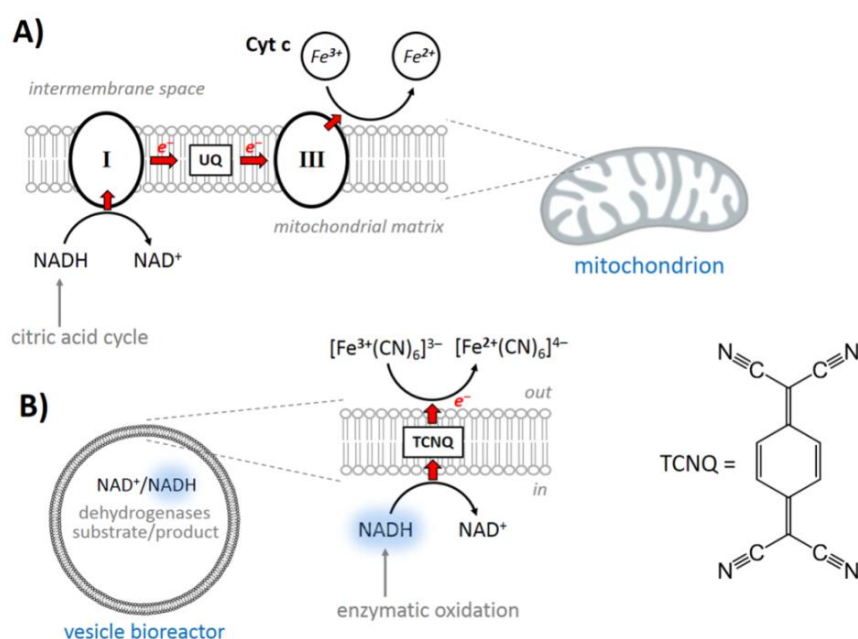


Figure 5.3 Schematic presentation of the analogy of natural electron transport chain in mitochondria (A) and TCNQ based NAD^+ regeneration module (B)¹¹⁸.

5.2 Experimental details

5.2.1 Oxidation of NADH with ferricyanide

The oxidation of NADH to regenerate NAD^+ by reduction of ferricyanide was monitored based on the fluorescence intensity of NADH measured with a Cary Eclipse

Fluorescence Spectrophotometer (Agilent Technologies, Santa Clara, USA). The reaction was monitored for 1 h, with a fixed amount of NADH and adding different amounts of ferricyanide in 100 μL MOPS buffer (100 mM MOPS, 250 mM KCl, Tris, pH 7.2), so that the final molar ratio of NADH:[Fe(CN)₆]³⁻ was 1:0, 1:1, 1:2, 1:5, and 1:10, respectively.

5.2.2 Preparation and characterization of LUVs

First, transmembrane NADH oxidation with ferricyanide was studied by reconstitution of different mediators, TCNQ, UQ, or membrane dye Nile red (NR) in the lipophilic shell and encapsulation of NADH in the hydrophilic core of POPC vesicles in order to compare the efficiency of NADH oxidation. Here, NR was used not just for lipid staining, but also employed owing to its structural similarity to other phenoxazine and phenothiazine dye with known activity for NADH oxidation^{65-66,72}. The LUVs were prepared by the extrusion method using a mini-extruder (Figure 5.4). Firstly, a total of 5 μmol POPC lipids were added to 200 μL chloroform in a glass tube for better dispersion. Then, the solutions were dried under gentle nitrogen purging and vacuum application for 2 h to remove the solvent. When different mediators were reconstituted, another 66 μL 0.33 mg mL^{-1} TCNQ dissolved in acetonitrile, 80 μL 1 mg mL^{-1} UQ dissolved in chloroform or 64 μL 0.5 mg mL^{-1} NR dissolved in methanol were mixed with POPC in chloroform before drying, so that the final molar ratio of POPC to mediators was 50:1 and the corresponding LUVs were designated POPC-TCNQ, POPC-UQ, and POPC-NR respectively. Then, the dried thin films were hydrated by adding 500 μL MOPS buffer (100 mM MOPS, 250 mM KCl, Tris, pH 7.2). To detach the whole thin film from the wall of the tube, the hydration solutions were gently pipetted against the wall repeatedly and gently vortexed for several seconds to re-suspend homogeneously. Afterward, the suspensions were treated with repetitive freeze-thaw cycles (6 times), and each cycle consisted of freezing in liquid nitrogen for 1–2 min and thawing for 2–4 min in a 40 °C water bath. To confirm the location of TCNQ in the membrane, thanks to the intrinsic fluorescence of TCNQ in nonpolar solvents¹¹⁹, an aliquot of POPC vesicles with TCNQ reconstituted vesicle suspensions were taken for fluorescence microscopic imaging by use of an Axio imager A1 microscope (Carl Zeiss, Germany). In order to obtain uniform vesicles, the lipid suspensions were filtered 11

times by Avanti extruder (Avanti Polar Lipids, Inc., Alabaster, Alabama, USA) through a Nuclepore Track-Etch Membrane filter (0.2 μm pore size, Whatman PLC, UK) to obtain large vesicles (≤ 200 nm). The filtrates containing the vesicle suspensions were collected and stored at 4 $^{\circ}\text{C}$ for later use. When NADH encapsulated LUVs (POPC-NADH) were prepared, the hydration solution was the same volume of 10 mM NADH dissolved in the same MOPS buffer, and after extrusion, free NADH was separated by the gel exclusion chromatography. A disposable PD-10 desalting column (GE healthcare Life Sciences) filled with 8.3 mL Sephadex G-25 matrix (\varnothing 14.5 mm \times ca. 50 mm) was used for this purpose. At last, approximately 1 mL of purified vesicles was collected and stored at 4 $^{\circ}\text{C}$ for later use.

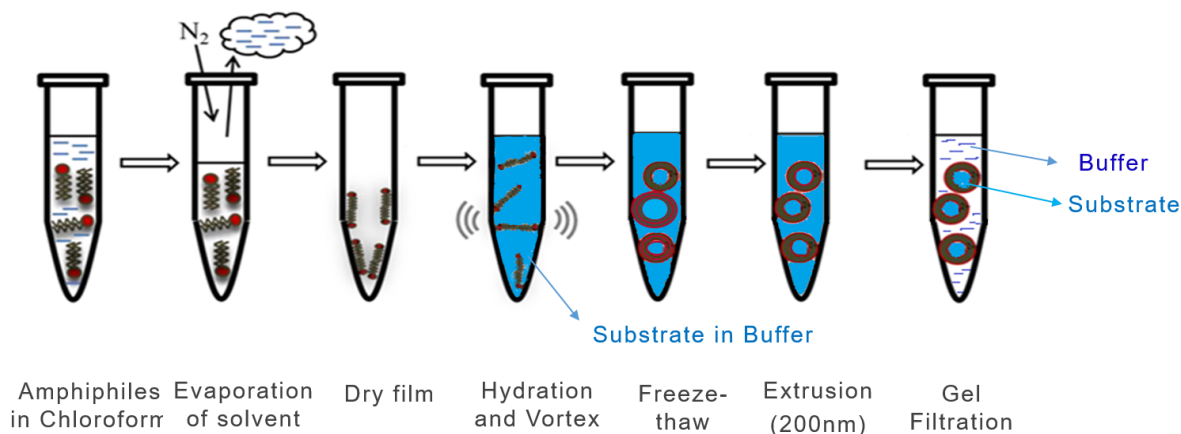


Figure 5.4 Schematic presentation of the LUVs preparation procedure.

Furthermore, to build more versatile synthetic modules, different synthetic compositions of natural lipids and polymers were prepared. The preparation procedure was essentially the same as for pure POPC vesicles, except that in the first step instead of 5 μmol POPC, 5 μmol of different amphiphiles composed of POPC/DOPC (with the molar ratio at 1:4, 1:1, 4:1), POPC/PDMS-*g*-PEO (with the same molar ratio at 1:4, 1:1, 4:1) or pure PDMS-*g*-PEO were used, and the corresponding vesicles formed were called mixed vesicles (MV1:1, MV1:4, MV4:1), hybrid vesicles (H1:4, H1:1, H4:1), and polymersomes (P), respectively.

The sizes of all these different types of LUVs were determined by dynamic light scattering (DLS) using a Zetasizer Nano ZS (Malvern, Worcestershire, UK) with a 663 nm

helium-neon laser at a fixed scattering angle of 173° at 25 °C. Every measurement was run three times with 70 s duration of every single run at room temperature. The average value of three measurements with standard deviation was reported for the hydrodynamic size of vesicles.

Additionally, for the sake of quantifying the kinetics and efficiency of NADH oxidation by different mediators in vesicles, the precise size and concentration of different POPC vesicles were further determined by tunable resistive pulse sensing (TRPS) with a qNano instrument (Izon Science Ltd., Christchurch, New Zealand). For the measurement, a NP200 stretchable nanopore was used that was calibrated with carboxylated polystyrene beads (CPC400F, mean size 350 nm, the concentration of 6×10^{11} vesicles mL⁻¹). The lower fluid cell was filled with 75 µl MOPS buffer and then 35 µl of the vesicle suspension diluted with the proper volume of MOPS buffer was added to the upper cell. The mean diameters and concentrations were calculated from the measurement data with the instrument software (Izon Control Suite 2, Chrsitchurch, New Zealand).

5.2.3 NAD⁺ regeneration in different LUVs

The different efficiency of NADH oxidation with TCNQ or UQ incorporated in POPC vesicles was determined by monitoring fluorescence intensity of NADH with a Cary Eclipse Fluorescence Spectrophotometer (Agilent Technologies, Santa Clara, USA). Briefly, all different vesicles with and without TCNQ or UQ reconstituted and NADH encapsulated prepared in the previous step were placed in a 10 mm quartz cuvette (500 µL, Hellma, Germany) at room temperature, and the change of NADH fluorescence intensity was monitored for over 12 h at 460 nm (slit width: 20) with an excitation wavelength of 340 nm (slit width: 20) at room temperature. The stability of free NADH and background fluorescence value of vesicles with or without TCNQ or UQ embedded was also determined over 12 h. Then, the same amount of ferricyanide as external electron acceptor was added to these vesicles to monitor the oxidation efficiency of NADH, accelerated by the mediators.

Additionally, the transmembrane electron transfer efficiency of NADH oxidation by TCNQ through different LUVs (POPC vesicles, mixed vesicles, hybrid vesicles, and polymersomes) consisting of different compositions of POPC and/or DOPC or PDMS-g-PEO

were also detected by the same method for the comparison of all LUVs with NADH encapsulated and with or without TCNQ reconstituted in the presence of ferricyanide.

5.2.4 Modelling of TCNQ based NAD⁺ regeneration in POPC LUVs

In order to analyze and model the reaction kinetics of NADH oxidation by TCNQ and ferricyanide, different amounts of ferricyanide in MOPS buffer were mixed with POPC-TCNQ vesicles encapsulating fixed amounts of NADH which is assumed as being homogeneously dispersed. The relationship of the concentration of NADH with its fluorescence intensity was determined by the calibration curve of free NADH in MOPS buffer (data shown in the later chapter). A fluorescence intensity of around 1000 (a.u.), corresponding to 20 μM of NADH based on the standard relationship of concentration (c)-fluorescence intensity (F): $F = 39.36 + 48.15 \cdot c$ ($R^2 = 0.99$). Accordingly, different aliquots of ferricyanide with a stock concentration of 10 mM in MOPS buffer were added to the vesicles suspensions and titrated with buffer to a final volume of 500 μL in the cuvette so that the final molar ratio of NADH to ferricyanide was roughly 1:5, 1:10, and 1:20, respectively.

When TCNQ is being reduced, it can assume two states: TCNQ^- after one-electron reduction, and TCNQ^{2-} after two-electron reduction. Hence, the absorption spectra of pure TCNQ and its anion form with lithium (LiTCNQ) dissolved in methanol were recorded. Then, the UV-Vis spectra of TCNQ-embedded POPC vesicles (POPC-TCNQ) with the molar ratio at 50:4 were scanned with or without ferricyanide. For comparison, free ferricyanide absorption spectra were also recorded. Considering the open-air condition, the effect of oxygen on the state of TCNQ in vesicles was further investigated by purging the POPC-TCNQ vesicles with pure oxygen and their spectra were obtained after different aeration times.

5.2.5 Leakage test

Considering the potential TCNQ effect on the permeability of vesicles, the leakage test was performed by encapsulation of a typical hydrophilic dye with smaller size,

carboxyfluorescein (CF) as a marker instead of NADH with the same concentration in MOPS buffer to prepare POPC vesicles with different amount of reconstituted TCNQ (with the molar ratio of POPC:TCNQ at 1:0, 50:1, 25:1). CF is a self-quenched fluorescence and is often used to test the leakage of vesicles thanks to the effect of concentration quenching when being encapsulated in vesicles¹²⁰ so that it would de-quench in the case of leaking out. During the preparation procedure, non-encapsulated CF was filtered by column purification following the same procedure used for NADH encapsulated vesicles. Then, CF encapsulated POPC LUVs without or with reconstituted TCNQ were placed in a 10 mm quartz cuvette (500 μL , Hellma, Germany) at room temperature and the fluorescence was monitored for over 12 h at 524 nm (slit width: 2.5) at an excitation wavelength of 494 nm (slit width: 2.5). Afterward, 1% octyl glucoside (OG) was pipetted into POPC vesicle suspension to disrupt vesicles and achieve complete release and full de-quenching of CF. The value of fluorescence intensity of CF before and after adding OG was compared to check the potential leakage.

In addition, as ferricyanide would be added to vesicles suspension, the potential diffusion of ferricyanide into vesicles was tested by incubating ferricyanide with empty vesicles overnight and afterward filtered by use of a column, using the same procedure as previously described for NADH filtration. Ferricyanide absorbs at a wavelength of 420 nm with an extinction coefficient of $1040 \text{ M}^{-1} \text{ cm}^{-1}$, which provides the possibility to detect it by use of a UV/Vis spectrophotometer (SPECORD[®] 50 PLUS, Analytik Jena AG., Germany). Here vesicles composed of POPC and POPC/PDMS-g-PEO hybrid vesicles at ratio 1:4 (H1:4) were checked, with TCNQ embedded at the molar ratio of amphiphiles to TCNQ at 50:1, 25:1, respectively.

5.2.6 Preparation of different GUVs

For comparison to LUVs and a visible investigation of different vesicles with a size scale similar to natural cells (tens of microns), giant POPC vesicles (GV), POPC/DOPC mixed vesicles (GMV), POPC/PDMS-g-PEO hybrids (GH) were prepared via the electroformation method (Figure 5.5)¹⁰⁰. Briefly, 25 μL 1 mg mL^{-1} of amphiphilic molecules with different

compositions dissolved in chloroform were spread under vacuum on a defined area (within the area defined by a circular silicone spacer) on each of paired glass slides coated with indium tin oxide (ITO) with a surface resistivity of $20 \Omega/\text{sq}$. Following the LUVs study, the different compositions included different amounts of pure POPC or POPC with DOPC or PDMS-*g*-PEO (molar ratio at 1:4) and mixed without or with TCNQ (molar ratio of amphiphilic molecules to TCNQ at 50:1). For the practical location of the giant vesicles, 0.05 mol% of PE-Lissamine Rhodamine B (PE-Rho), a fluorescent lipid probe was mixed with all vesicles. The organic solvent was further evaporated under nitrogen. After placing the silicone spacer, glass slides in pairs were fixed with a clamp and filled with 1 mM NADH dissolved in 0.2 M sucrose in Milli-Q water. Then, a sine wave with 2 V, 10 Hz was applied for 45 min followed by a squared wave with 1 V, 2 Hz for 15 min. Afterward, different GV, GMV, and GH were gently collected and stored at 4 °C for later use. Before imaging micron-scale vesicles, they were diluted with a three-fold volume of glucose with proper concentration, resulting in the same osmolality as the sucrose solution used for hydration. The osmolality values were measured with the Osmomat 3000 (Gonotech GmbH, Berlin, Germany).

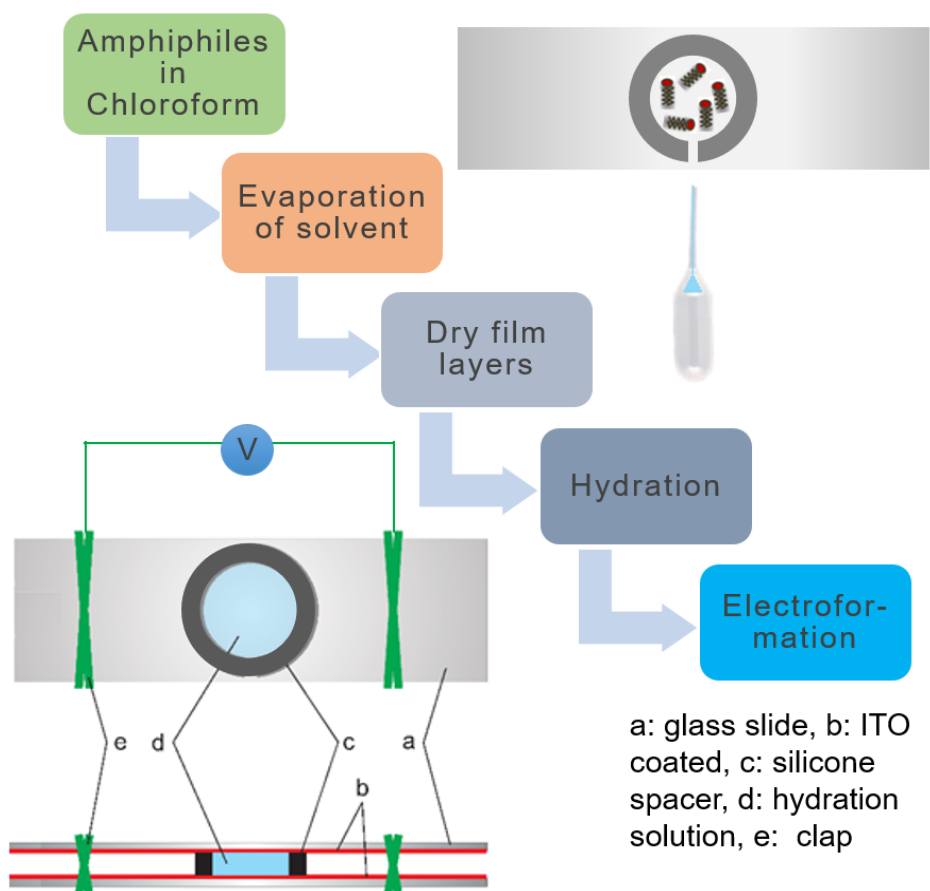


Figure 5.5 Schematic presentation of the GUVs preparation procedures.

Micron-scale GUVs were investigated under a Zeiss inverted fluorescence microscopy, equipped with mercury (HBO) arc lamps and an AxioCam 506 color camera. Two filters were used for detecting membrane fluorescence (PE-Rho Ex 560 nm/Em 583 nm) and encapsulated NADH (Ex 340 nm/Em 460 nm) from red fluorescent protein (Em 570-640 nm) and 4',6-diamidino-2-phenylindole (DAPI, Em 420-470 nm). Images were processed using the Zeiss software Zen.

5.2.7 NAD⁺ regeneration in TCNQ based GUVs

For the giant vesicles, the NADH oxidation efficiency by TCNQ in three membrane compositions, GV with POPC, GH with the molar ratio of POPC/PDMS-g-PEO 1:4 (GH), and GMV with the molar ratio of POPC/DOPC 1:4 (GMV), was assessed by monitoring the NADH fluorescence intensity with conventional fluorescence microscopy, confocal laser scanning microscopy (CLSM) or time-correlated single-photon counting wide-field microscopy before and after adding 10 mM ferricyanide in the proper concentration of glucose with the same osmolality of 1 mM NADH in sucrose worked as electron acceptor.

CLSM was done with an inverted confocal microscope (Leica SP8) with a 100 × oil immersion objective excited with laser beams at 355 nm and emission filter with range 400 to 800 nm. The device is located in the Institute of Molecular and Clinical Immunology, Medical Faculty, Otto-von-Guericke University Magdeburg. Later the images were obtained and processed with the LAS X software and the time-lapse was extracted.

For exciting NADH with single-photon counting by time-correlated single-photon counting wide-field microscopy, located in Special Laboratory for Electron and Laser scanning Microscopy in the Leibniz Institute for Neurobiology, a white light laser in combination with a SuperK Extend-UV (NKT Photonics, Denmark) was tuned at 355 nm and generated light pulses with a pulse repetition rate of 19.5 MHz and about 40 ps pulse width (FWHM). The collimated laser pulses were focused on the back focal plane of the UV-transparent objective (100x S-Fluor, NA 1.3, Nikon GmbH, Düsseldorf, Germany) to produce a uniformly illuminated field of view. A dichroic mirror (LP 355 nm, AHF, Tübingen, Germany) was used to discriminate between the excitation and the fluorescence signal and both a bandpass filter (BL 447/60, AHF, Tübingen, Germany). The fluorescence signal collected at the objective was projected on a sensitive wide-field camera based on a position-maintaining microchannel plate photomultiplier tube (MCP-PMT) with a direct charge readout of the position and an electronic interface for the data transfer (LINCcam25; PhotonScore Magdeburg, Germany). Later for image analysis, single photons were binned to a 2D histogram of 256 × 256 pixels. Further images were analyzed using the ImageJ-Fiji freeware to read the fluorescence intensity.

5.3 NAD⁺ regeneration in different LUVs

This chapter is based on two manuscripts published by the author of the present thesis. The first work was published in *Langmuir* under the title “Transmembrane NADH Oxidation with Tetracyanoquinodimethane” (<https://doi.org/10.1021/acs.langmuir.8b00443>). The text is reproduced in part with permission from the American Chemical Society (Copyright 2018). The second work was published in *Bioconjugate Chemistry* under the title “Scale up of Transmembrane NADH Oxidation in Synthetic Giant Vesicles” (<https://pubs.acs.org/doi/abs/10.1021/acs.bioconjchem.1c00096>). The text is reproduced in part with permission from the American Chemical Society (Copyright 2021). Data, images, and text relevant to this study are included in this chapter. Under the advice of the co-authors, the author of this dissertation conducted the experiments, analyzed the resulting data, and drafted the two manuscripts. The co-authors contributed editorial comments and additional text where needed.

5.3.1 Oxidation of NADH with ferricyanide

The redox potential of the ferri/ferrocyanide couple at room temperature is around + 410 mV¹²¹⁻¹²⁴, which is higher than the redox potential of NADH/NAD⁺ couple (− 320 mV under standard conditions, 25 °C and pH 7)⁸⁹. In *E. coli*, an NADH dehydrogenase works efficiently for oxidation of NADH with ferricyanide as electron and hydrogen acceptor¹²⁵, the optimal activity of it was at 45 °C and pH 7.5 (Michaelis constant K_m value for NADH: 10 μM). Besides, NADH oxidation by oxygen or potassium ferricyanide can be catalyzed by gold nanoparticles in an aqueous solution¹²⁶. In addition, the ferri/ferrocyanide redox couple has a long history in transmembrane electron transfer studies¹²⁷ and can be easily regenerated electrochemically, thus providing a possible means for the use of electrical energy to drive biological reactions for NADH oxidation as shown in the literature¹²⁸⁻¹³⁰. Here NADH is oxidized by potassium ferricyanide in MOPS buffer at pH 7.2 and room temperature (Figure 5.6) with different ratios of NADH:[Fe(CN)₆]³⁻, different normalized fluorescence profiles of NADH were obtained. With a higher amount of ferricyanide, the oxidation of NADH was faster,

which indicated the electron exchange happened easier between NADH and ferricyanide. Meanwhile, there was almost no degradation of NADH during 1 h (at ratio of NADH: $[\text{Fe}(\text{CN})_6]^{3-} = 1:0$, black symbols in Figure 5.6).

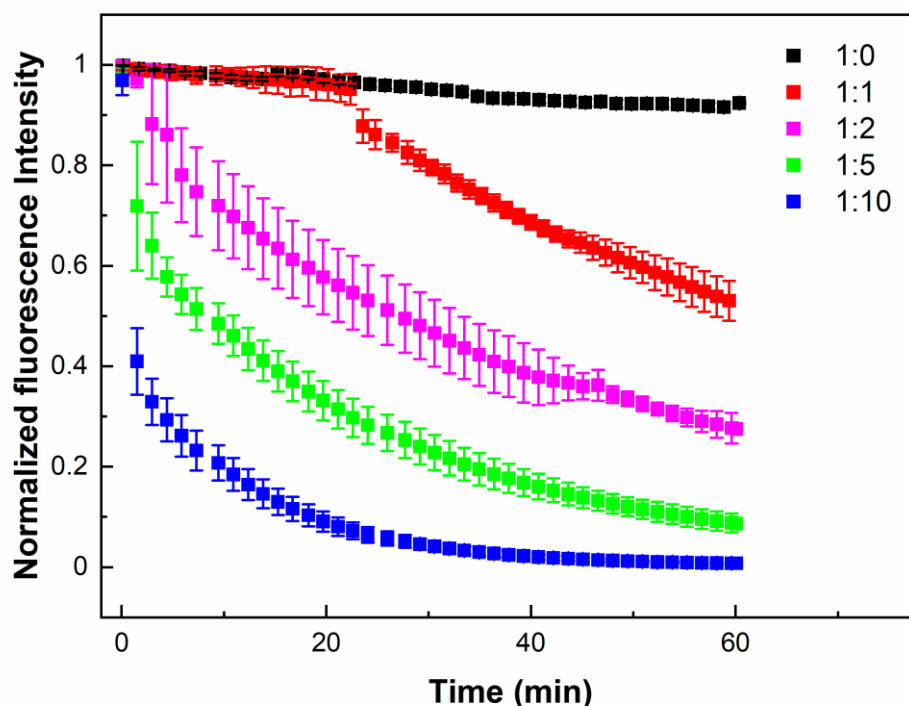


Figure 5.6 Normalized NADH fluorescence profiles of time-dependent reaction of NADH oxidation with ferricyanide in MOPS buffer (100 mM MOPS, 250 mM KCl, Tris, pH 7.2) at different molar ratios of NADH to ferricyanide (1:0, 1:1, 1:2, 1:5, and 1:10).

5.3.2 Characterization of POPC LUVs with different mediators

The fluorescent image of POPC LUVs reconstituted with TCNQ and membrane dye NR is shown in Figure 5.7, which demonstrates that POPC vesicles were well-formed mostly as unilamellar vesicles with only a few multilamellar or multivesicular vesicles. Likewise, for

POPC vesicles reconstituted with TCNQ, LUVs were formed with relatively larger sizes and TCNQ was mostly staying in the inner layer of the vesicles because of its hydrophobicity¹³¹. As for UQ, no fluorescence was detected in the microscope. After the later procedures for LUVs preparation, particularly the extrusion, the size distributions of POPC LUVs with different mediators (TCNQ, UQ) or membrane dye (NR) were determined by DLS, as shown in Figure 5.8. The z-average hydrodynamic diameters of different vesicles were all around 150 nm which is well matching the pore size of the filter membrane. The polydispersity index (PDI) was much lower than 0.2, indicating good uniformity of the LUV size. Overall, when NADH is encapsulated in vesicles, the mean diameters of TCNQ, UQ, and NR reconstituted POPC vesicles (the mean sizes were 156 nm, 150 nm, and 155 nm respectively) were nearly the same as POPC vesicles (POPC-NADH, 156 nm). For LUVs without encapsulated NADH, the mean diameter at all compositions was almost identical to those of NADH-encapsulated LUVs. This demonstrates that the encapsulation of NADH in LUVs and the column purification did not affect the size of LUVs. In all LUVs, the diameters of UQ reconstituted POPC vesicles were slightly smaller than other LUVs, which might be due to the fact that UQ can increase the packing order of POPC and condense the membrane as in mitochondrial membranes¹³².

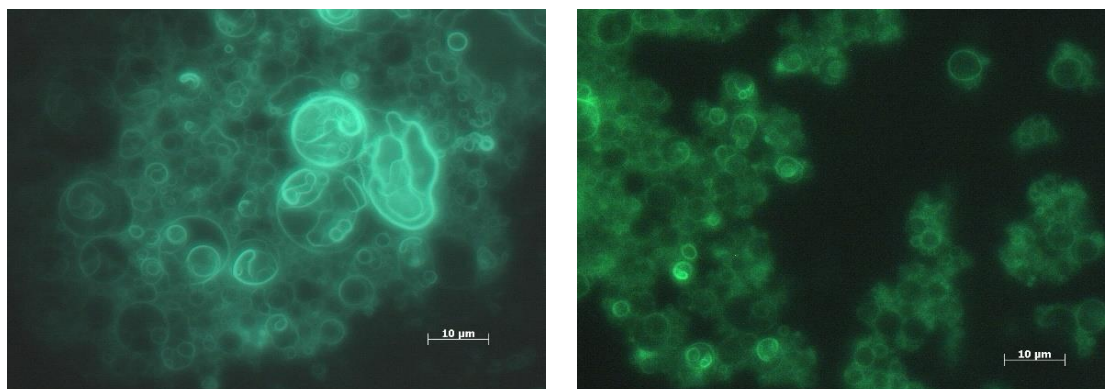


Figure 5.7 Fluorescence microscopy image of POPC vesicles with TCNQ reconstituted (left) and membrane dye NR (right) under the excitation of blue light.

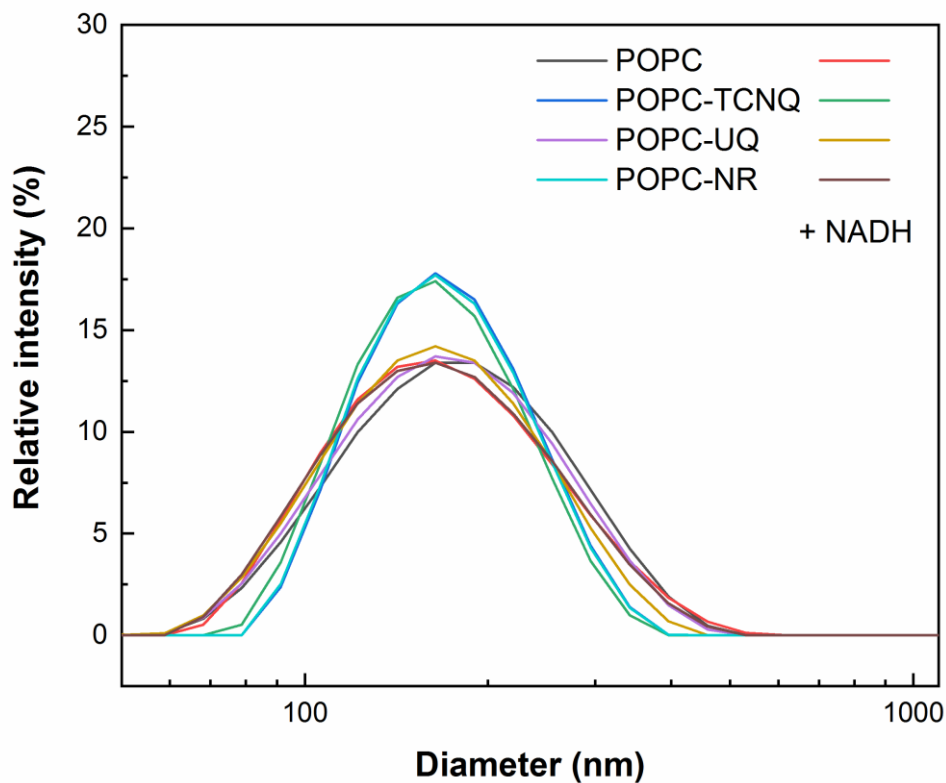


Figure 5.8 Size distributions of different LUVs: POPC vesicles, vesicles with TCNQ, UQ, and NR reconstituted with and without encapsulation of NADH.

In addition, the measurement results from TRPS (tunable resistive pulse sensing) are summarized in Table 5.1. The vesicle sizes match the results obtained from DLS. Meanwhile, the concentrations of vesicles were all similar to each other which indicated the comparability of different LUVs; also, NADH encapsulation and subsequent column purification did not affect the vesicle size and concentration significantly.

Table 5.1 Size and concentration data for vesicles with reconstituted mediators and encapsulated NADH obtained from TRPS.

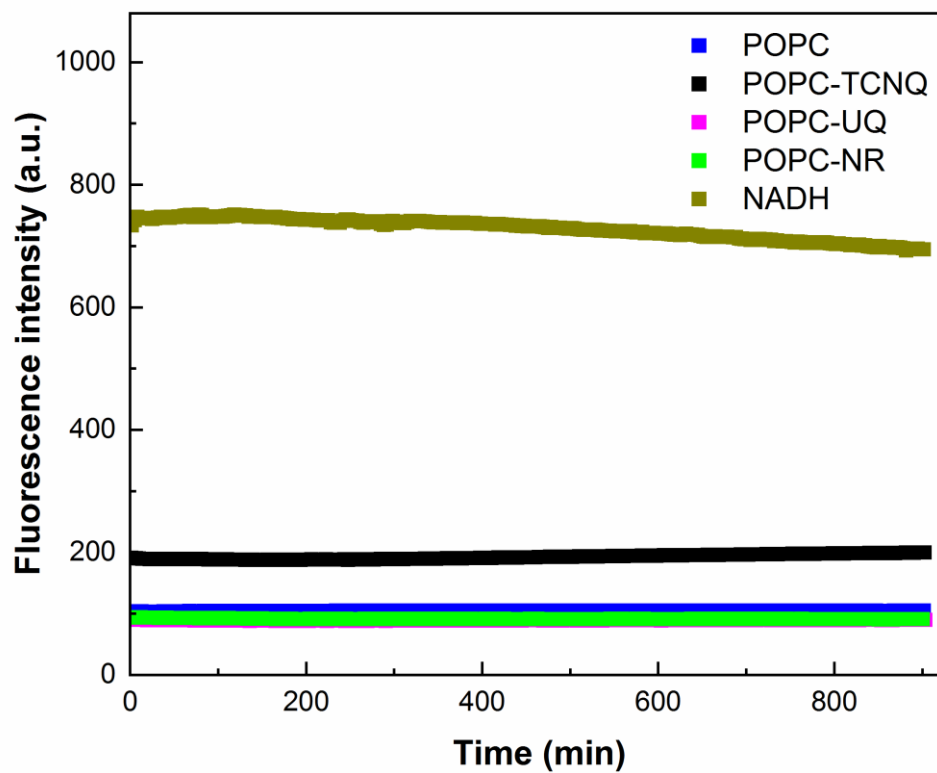
Vesicles Containing:	Mean diameter (nm)	Particle concentration (mL ⁻¹)
TCNQ	169 ± 5	5.9 ± 0.4 × 10 ¹¹
UQ	143 ± 4	18 ± 5.3 × 10 ¹¹
Nile red	169 ± 5	4.5 ± 1.2 × 10 ¹¹
TCNQ + NADH	170 ± 5	7.7 ± 0.7 × 10 ¹¹
UQ + NADH	150 ± 5	9.4 ± 3.6 × 10 ¹¹
Nile red + NADH	171 ± 5	2.9 ± 1.3 × 10 ¹¹

5.3.3 NAD⁺ regeneration in POPC LUVs with different mediators

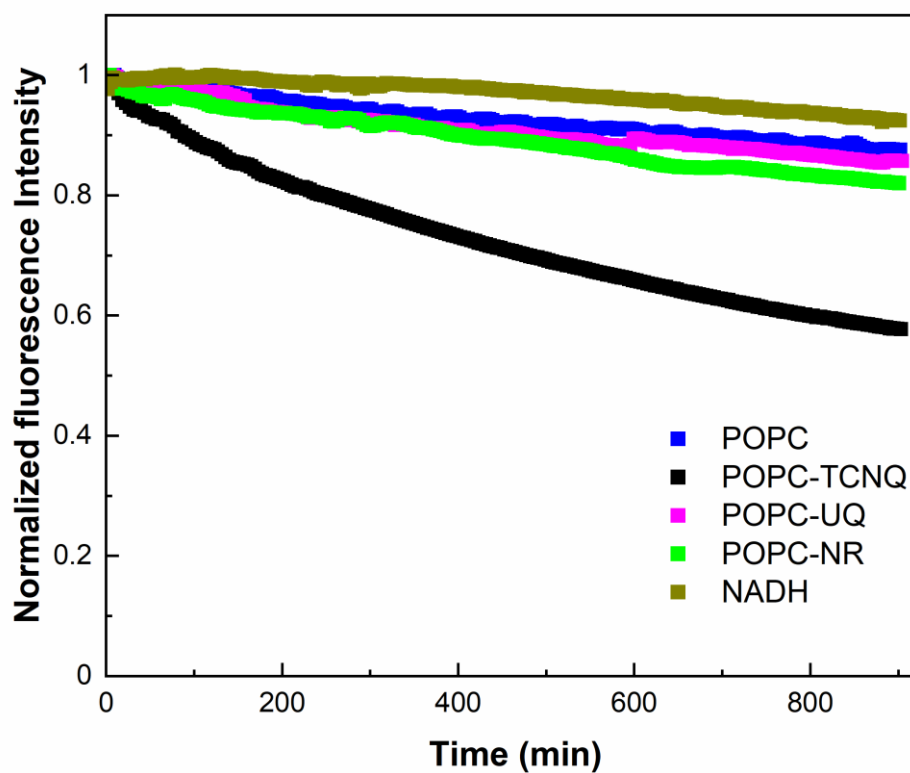
In the transmembrane oxidation module, when being loaded in vesicles, NADH was oxidized by ferricyanide outside of these vesicles by the electron transfer mediator in the membrane. As known in many mitochondrial membranes, UQ works together with NADH dehydrogenase to oxidize NADH and simultaneously generate proton gradients. Herein, TCNQ works as a more efficient replacement agent to UQ and can directly oxidize NADH without any aid of enzymes. As illustrated in Figure 5.9 A, NADH showed a slight decrease of the fluorescence intensity by atmospheric oxygen over 12 h (brown) due to inherent degradation of NADH^{126, 133}. TCNQ-reconstituted vesicles (POPC-TCNQ) had a background fluorescence intensity around 200 a.u. (black, Figure 5.9 A), relatively higher than the one for pure POPC vesicles (blue, Figure 5.9 A), UQ-reconstituted vesicles (red, Figure 5.9 A) and NR-reconstituted vesicles (green, Figure 5.9 A) which might be due to the overlap of TCNQ fluorescence^{119, 134} as shown in the image of TCNQ reconstituted vesicles in Figure 5.6 (left

panel). For NADH being encapsulated in these three types of vesicles, the stability of normalized fluorescence intensity profiles is shown in Figure 5.9 B under open air conditions at room temperature. NADH encapsulated in POPC vesicles (blue), UQ reconstituted vesicles (magenta), and NR reconstituted vesicles (green) slightly decreased, similar to the free NADH solution (brown, Figure 5.9 A) which might be due to the fact that oxygen is freely diffusing through the vesicular membrane^{27, 95-96}. Meanwhile, with TCNQ reconstituted in vesicles (black), the normalized fluorescence intensity of encapsulated NADH decreased, which is due to the higher electron transfer ability of TCNQ to oxygen compared with UQ, NR, or pure POPC vesicles¹³⁵⁻¹³⁶. Furthermore, when NADH encapsulated vesicles were mixed with 200 μM of ferricyanide, the difference of normalized fluorescence intensity profiles was more pronounced (Figure 5.9 C). Based on the fluorescence intensity value of TCNQ reconstituted vesicles (black, Figure 5.9 A), it could demonstrate that almost all NADH molecules encapsulated in TCNQ reconstituted vesicles were oxidized by external vesicular ferricyanide through transmembrane electron transfer, which corresponds to the results reported by Hichiri K. *et al.* for a planar lipid bilayer¹³⁷. In addition, the fluorescence spectra of NADH encapsulated and TCNQ or UQ reconstituted vesicles before and after being mixed with 100 μM ferricyanide were determined. The experiments revealed that the fluorescent peak of NADH decreased significantly (Figure 5.9 D). Besides, the value of the fluorescence intensity for TCNQ embedded vesicles after adding ferricyanide at 460 nm was around 200, which is exactly corresponding to the background fluorescence of TCNQ in vesicles (black, Figure 5.9 A). This further confirms that all NADH molecules encapsulated were oxidized.

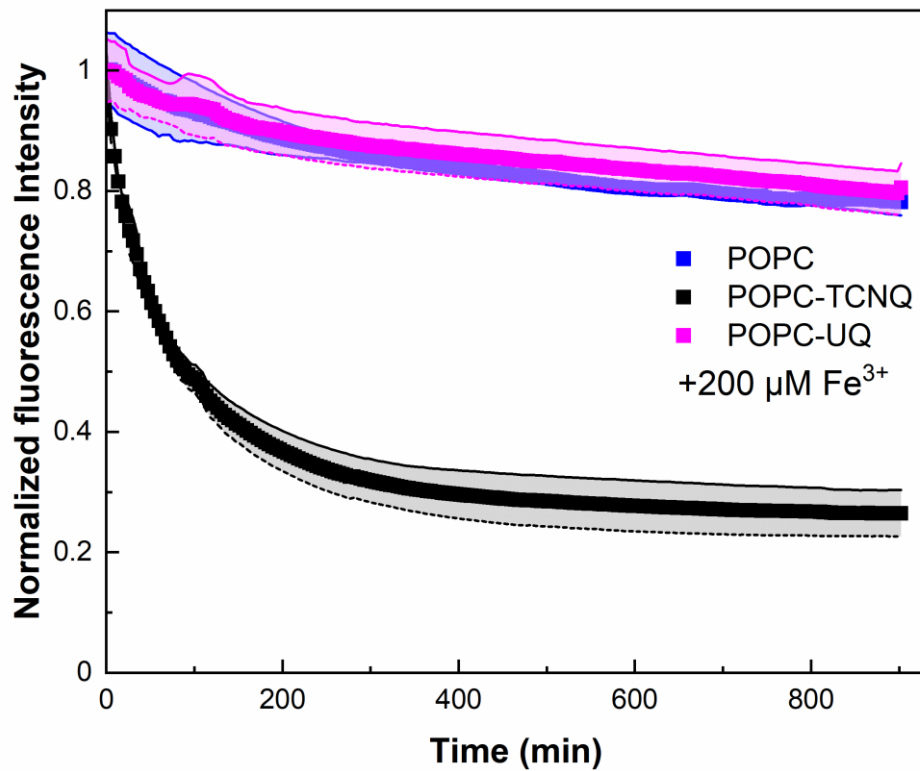
A)



B)



C)



D)

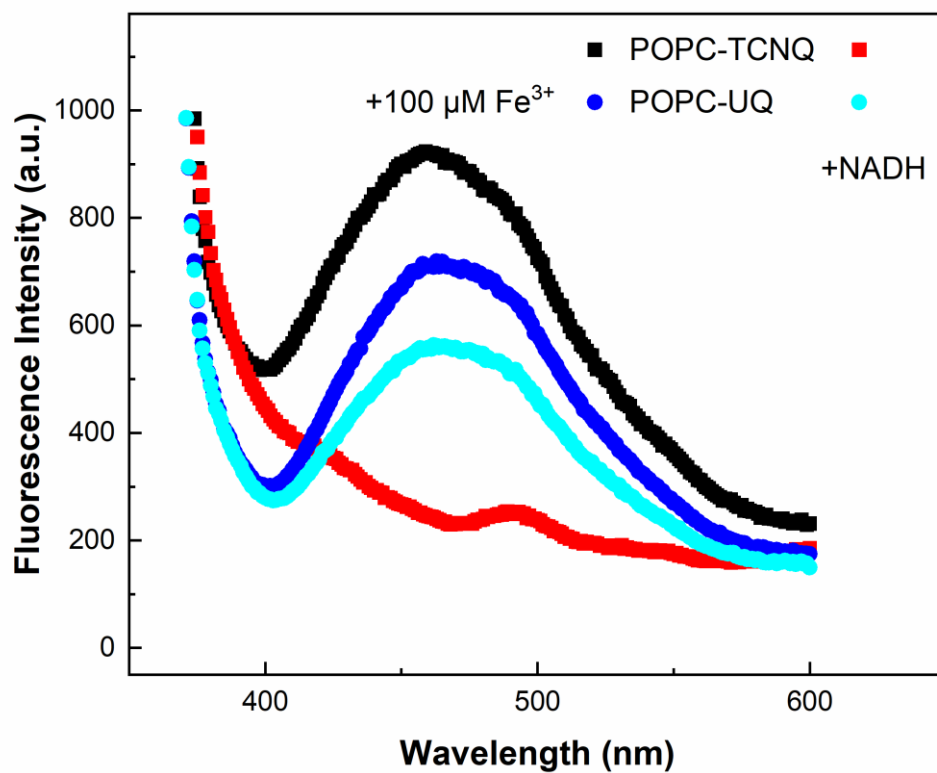
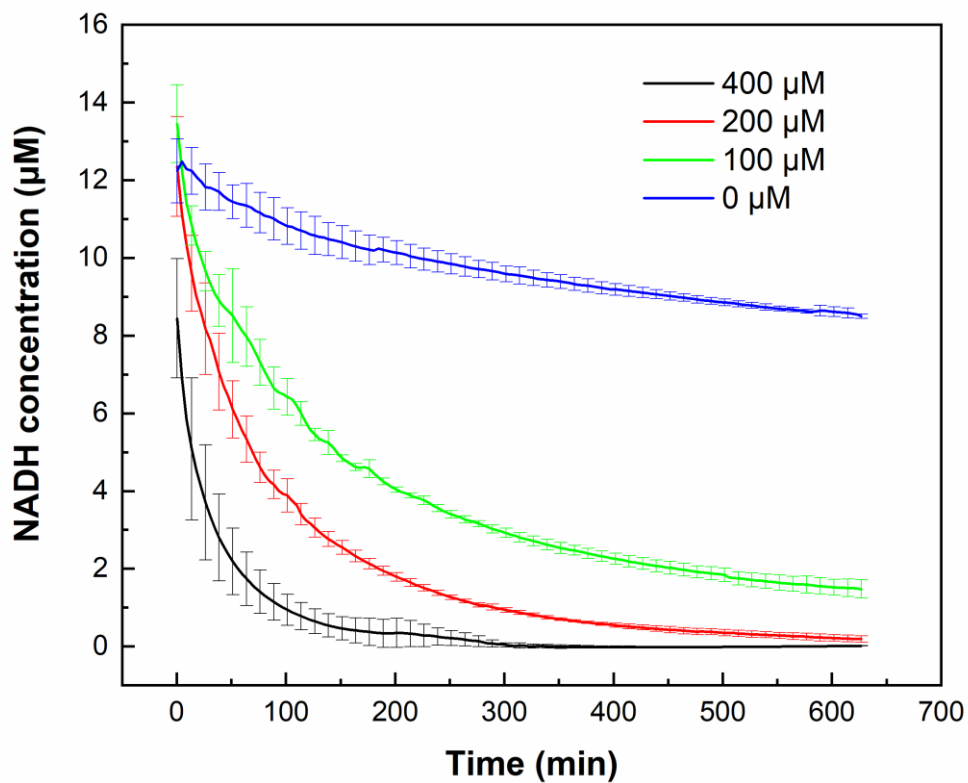


Figure 5.9 Fluorescence intensity and normalized profiles of NADH in different vesicular configurations over time.

5.3.4 Modelling of TCNQ based NAD⁺ regeneration in POPC LUVs

To obtain more details on the regeneration kinetics, different concentrations of ferricyanide were added to the TCNQ-functionalized POPC LUVs (Figure 5.10 A). The concentration of NADH was converted based on the calibration curve of the fluorescence of free NADH in MOPS buffer (Figure 5.10 B). At around 15 μM NADH in the entire vesicle suspension (calculated from the measured initial fluorescence intensity) and based on the data obtained from TRPS (the vesicle concentration was around $7.7 \times 10^{11} \text{ mL}^{-1}$ which referred to $\sim 1.98 \times 10^{-3} \text{ mL mL}^{-1}$ suspensions), the amount of encapsulated NADH was around 2×10^{-20} mol per vesicle and the concentration was 7.6 mM in TCNQ-functionalized POPC LUVs. Despite the fact that the NADH calibration curve was not recorded at identical conditions (free NADH in the μM range versus encapsulated in the mM range), we assumed that its use was justified because we did not observe any quenching effects in the relevant concentration range. Information about the NADH concentration change enables the comparison between the present system and NADH/UQ oxidoreductase (complex I) in mitochondria, which can be regarded as a biological counterpart of TCNQ. If we take, as an example, the experiment with 200 μM ferricyanide during the first 60 min (steep decrease), the average rate of NADH oxidation is about $0.13 \mu\text{M min}^{-1}$. This value is comparable to the reported activity of an isolated enzyme ($\sim 0.2 \mu\text{M min}^{-1}$)¹³⁸, but normalizing the molecular weight of the respective catalysts would result in a better figure of merit.

A)



B)

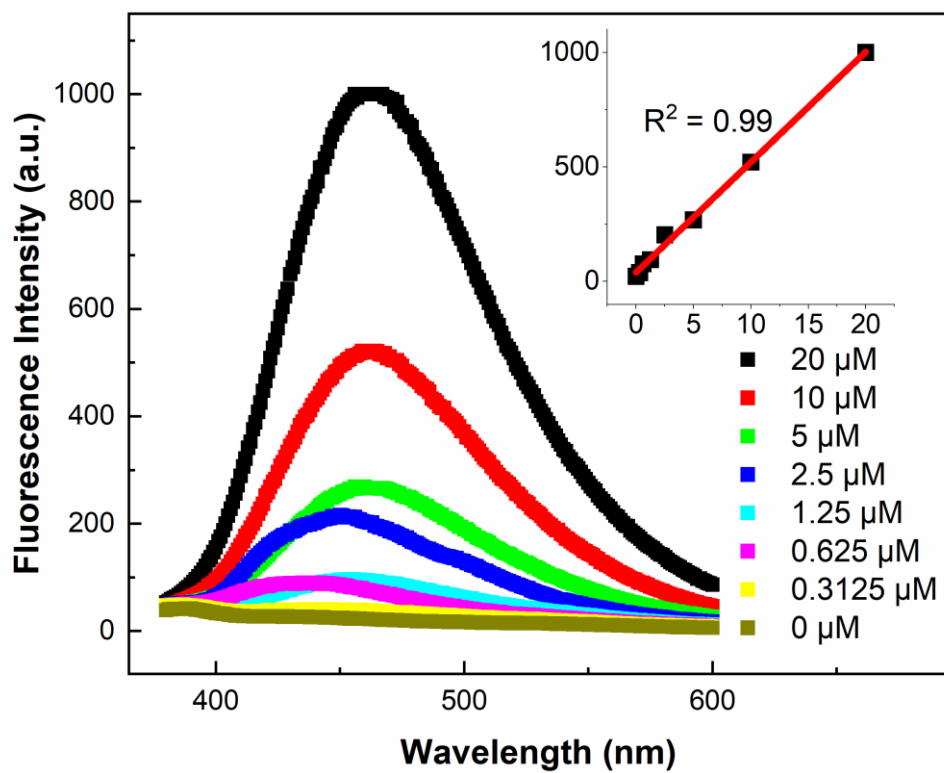
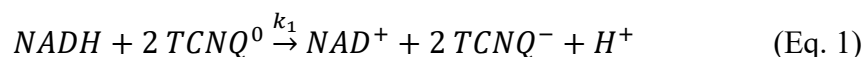


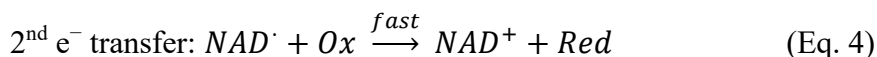
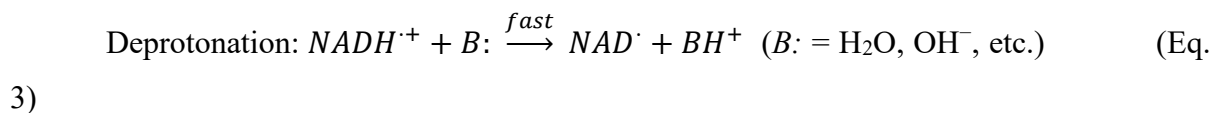
Figure 5.10 A) NADH concentration profile: NADH loaded (20 μM input) in POPC-TCNQ vesicles react with different concentrations of ferricyanide (0-blue, 100 μM -green, 200 μM -red, 400 μM -black). B) Fluorescence spectra of NADH at different concentrations, inset: NADH fluorescence intensity in dependence on the NADH concentration.

In the next step, we developed a homogeneous phase model to describe the properties of the system. TCNQ is known to undergo two one-electron reduction steps: (1) to a radical anion ($\text{TCNQ}^{\cdot-}$) at + 0.21 V vs. SHE, and (2) subsequently to a dianion (TCNQ^{2-}) at - 0.45 V vs. SHE^{136, 139}. Since the potential of the second redox conversion is more negative than the NADH potential (- 0.32 V vs. SHE), we concluded that the mediator is mono-reduced, according to the stoichiometry of **Eq. 1**. Actually, the mechanism of 1-benzyl-1,4-dihydronicotinamide (NADH model compound) oxidation with tetracyanoethylene also involved a radical anion¹⁴⁰. In addition, the electrochemical behaviour of immobilized TCNQ by the oxidation of NADH⁶⁴ or enzyme-bound FAD¹⁴¹ also suggests that monoanion species are involved (intact di-anion redox peak, oxidation onset).

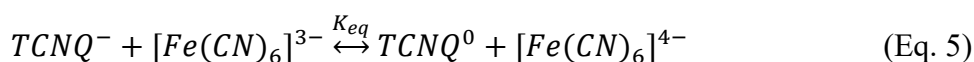


The mechanism of hybrid transfer during NADH oxidation is still not completely elucidated, and there is a dichotomy between concerted and stepwise pathways, as shown with NADH analogues¹⁴². After the confirmation of the NADH radical cation ($\text{NADH}^{\cdot+}$)¹⁴³, it is widely accepted that the chemical oxidation involves a multistep mechanism with consecutive $e^-/\text{H}^+/e^-$ steps (**Eqs. 2-4**). The absence of isotope and pH effects during the oxidation of NADH by ferrocene ruled out hydride transfer and rate-limiting deprotonation and justified the first electron transfer as a rate-determining step¹⁴⁴. In the present case, we assumed a similar situation and modeled the oxidation of NADH by TCNQ^0 through an irreversible bimolecular one-electron transfer using the rate constant k_1 .

Equations: Multistep oxidation of NADH by one-electron oxidants



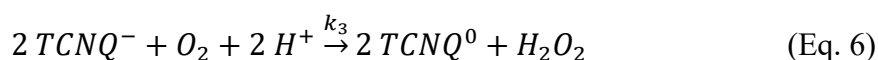
While TCNQ has been rarely used directly for NADH oxidation^{64, 145} (mostly bound in charge transfer complexes¹⁴¹), it has an established record in combination with ferri/ferrocyanide in a black lipid membrane (BLM)¹⁴⁶ and ITIES (interface between two immiscible electrolyte solutions) systems^{139, 147} electrochemical setups, according to **Eq. 5**.



where $K_{eq} = k_2^+/k_2^-$. Unlike the previous reaction, which has been considered as irreversible due to the large driving force (0.53 V) and the known difficulties in chemical reduction of NAD^+ (i.e., the backward reaction)⁵⁵, we considered the regeneration of $TCNQ^0$ as reversible. The redox potential of ferricyanide (around 0.41 V vs. SHE¹⁴⁸) lies close to that of TCNQ and despite the fact that the reaction in **Eq. 5** is thermodynamically favorable, potential-determining ions can influence the equilibrium through a Galvani potential and thus drive uphill electron transfer¹⁴⁷. The latter has been confirmed in ITIES (interface between two immiscible electrolyte solutions) systems, which are useful models for the half-reactions in the present case¹³⁹. In this regard, the ability of TCNQ to transport protons and other cations has been demonstrated through electrochemical experiments in a BLM setup^{137, 149}, which postulates the generation of an interfacial potential difference by partitioning cations as a plausible phenomenon.

Apart from the ferricyanide oxidation of NADH, we also observed a decrease of the NADH concentration in the absence of an added electron acceptor (Figure 5.10A). As discussed in the previous section, spontaneous NADH degradation took place¹³³ but the observed rates were lower and therefore the possibility of a TCNQ oxidation by dissolved oxygen cannot be ruled out. A computational DFT study has recently revealed that metal salts

such as FeTCNQ can efficiently catalyze the four-electron oxygen reduction¹⁵⁰, while in the past it has been shown that electrogenerated TCNQ dianions interact with oxygen to form α,α -dicyano-*p*-toluoyl-cyanide¹⁵¹. In addition, TCNQ radical anions (TCNQ^{•-}), which take part in **Eq. 1** and **Eq. 5** also exhibit charge transfer interactions with oxygen¹⁵². Based on this notion we hypothesized the irreversible two-electron reduction of oxygen to peroxide as a competing reaction to the ferricyanide reduction (**Eq. 6**).



The redox potentials for oxygen reduction at pH 7 are 0.82 V and 0.28 V vs. SHE to water and peroxide, respectively¹⁵³, rendering both pathways thermodynamically feasible, but the former one is more likely. Since oxygen was in excess with respect to TCNQ and the experimental system was buffered, we disregarded protons and expressed the reaction through a pseudo-second-order kinetic approach with the rate constant k_3 . Due to the fact that the exact nature of the participating species is unknown (TCNQ^{•-} or TCNQ²⁻, H₂O or H₂O₂), we assumed a radical anion in order to avoid additional equations and parameters, and peroxide in order to maintain lower TCNQ stoichiometry in **Eq. 6**.

Table 5.2 Initial concentrations used in the simulation.

NADH + NAD ⁺	15 μM
TCNQ ⁰	1.8 μM
TCNQ ^{•-}	5.6 μM
O ₂	245 μM
[Fe(CN) ₆] ³⁻	0, 100, 200, 400 μM
[Fe(CN) ₆] ⁴⁻	0 μM

After the definition of the equation system, we estimated a parameter set (Table 5.3) to fit the experimental data for NADH oxidation (initial conditions summarized in Table 5.2). This work was conducted by another co-author of the aforementioned publication in *Langmuir*, but it is briefly described here for clarity. It should be noted that in order to retain the simplicity of the model, in the actual rate expressions we omitted protons due to the buffered experimental system, and peroxide since the product of oxygen reduction was unknown. While the concentrations of NADH, oxygen, and ferricyanide were readily available, the TCNQ concentration was calculated as 7.4 μM (~ 5700 molecules per vesicle) based on TRPS results (6.99×10^{16} nm^2 total area of vesicles in 1 mL, 0.63 nm^2 area of POPC¹⁵⁴, POPC: TCNQ = 50:1). The parameter estimation was performed by minimizing the residual sum of squares (RSS) between simulation and experimental datasets using the Copasi toolbox¹⁵⁵. A genetic algorithm was used to find an approximation for a suitable global minimum of the RSS¹⁵⁶ and afterward, the gradient-oriented simplex algorithm was applied to certainly reduce the RSS into global minimum and the best suiting parameter set¹⁵⁷. The fitted kinetic constants can be considered reliable, because all reaction or equilibrium constants are identifiable so that the RSS around the minimum fulfilled the condition of an F-test in 95 % confidence interval with n constants and m data points of measurement¹⁵⁸.

Table 5.3 Estimated rate and equilibrium constants.

Parameter	Fitted value	Confidence interval
k_1	$2.2 \times 10^{-5} \mu\text{M}^{-2} \text{s}^{-1}$	$\pm 3.7 \times 10^{-6}$
K_{eq}	0.024	± 0.0047
k_3	$8.8 \times 10^{-9} \mu\text{M}^{-2} \text{s}^{-1}$	$\pm 2.3 \times 10^{-9}$

The fitted curves described the experimental data well (Figure 5.10A), but at the present stage, it is difficult to compare the obtained constants with literature values (if existing), because the latter have been expressed in different ways. For instance, the rate constant for NADH oxidation by TCNQ in an amperometric sensor has been determined to be $4.8 \times 10^6 \text{ M}^{-1}$

¹ s⁻¹ on the basis of peak current analysis⁵⁸. It should be noted that this work used an unconventional reaction scheme expression through an electrically unbalanced reaction between NADH and TCNQ, while the typical scheme for mediated enzymatic electrodes is neutral and accounts for the respective electron stoichiometry as in Eq. 1. The rate constants greatly varied in other homogeneous systems. For instance, the oxidation of NADH by ferrocene was previously determined to be 50 times slower than in the present case (5.4 M⁻¹ s⁻¹)¹⁴⁴, but when a radiolytically generated dibromide radical anion was used as the oxidant, the rate constant was 7 orders of magnitude higher [(~1.1–1.5) × 10⁹ M⁻¹ s⁻¹]¹⁵⁹.

On the contrary, the obtained K_{eq} , characterizing Eq. 2, was in the range of values resulting from the expected concentrations of species, keeping in mind the excess ferricyanide. In addition, we transformed K_{eq} to an electron transfer rate constant in order to compare it with existing values in the ITIES setups. The Marcus cross-relation¹⁶⁰ allows for the calculation of the homogeneous electron transfer rate constant according to $k_{12} = (k_{11}k_{22}K_{12}f_{12})^{0.5}W_{12}$, where k_{12} , K_{12} is analogous to k_2^+ , K_{eq} in the present case. The contributions of various work terms for reactants and products expressed in parameters f_{12} (known as the frequency factor) and W_{12} are typically close to 1, and thus f_{12} , $W_{12} = 1$ is a customary assumption¹⁶¹. The self-exchange rate constants (k_{11} , k_{22}) for TCNQ/TCNQ⁻ and ferri/ferrocyanide have been cited to be 10⁹ M⁻¹ s⁻¹ and 5.8 × 10⁴ M⁻¹ s⁻¹, respectively¹⁶². We divided the obtained homogeneous k_{12} by the surface-to-volume ratio of the bilayer (relationship derived from mass balance) to convert it to a heterogeneous rate constant and calculated a value of 0.27 cm M⁻¹ s⁻¹. In addition, since it is known that the self-exchange reaction of ferri/ferrocyanide is influenced by cations, we used a cation-independent k_{22} value of lower magnitude (2.4 × 10² M⁻¹ s⁻¹)¹⁶³, and obtained a ca. 15 times lower value (0.018 cm M⁻¹ s⁻¹) for the heterogeneous bimolecular rate constant. The latter has been previously determined for TCNQ/ferricyanide by impedance spectroscopic analysis in the ITIES setup to be 0.129 cm M⁻¹ s⁻¹ on the basis of an apparent standard rate constant of 5.4 × 10⁻³ cm s⁻¹¹⁶⁴. The same authors reported a decreased apparent rate constant of 1.8 × 10⁻³ cm s⁻¹ in the presence of an adsorbed phospholipid monolayer at the interface and discussed it in the context of the Marcus theory¹³⁹. It should be noted that the heterogeneous bimolecular constant (0.129 cm M⁻¹ s⁻¹) has been defined at zero driving force (referred to as standard) in the context of the Butler-

Volmer theory¹⁶⁴. Thus, in the expression for K_{eq} , the bimolecular constants cancel out and K_{eq} is dependent only on the driving force, expressed as a potential, which we determined to be around -130 mV in the present case. Assuming a transfer coefficient of 0.5, the driving force of -130 mV was used to transform the literature standard rate constant to a forward rate constant ($\sim 0.01 \text{ cm M}^{-1} \text{ s}^{-1}$)¹⁶² to be able to compare it with the values calculated through the Marcus cross-relation (0.27 or $0.018 \text{ cm M}^{-1} \text{ s}^{-1}$), which included the driving force by definition and neglected work-related terms. As can be seen, the orders of magnitude roughly correspond to each other, but we will refrain from further conclusions due to the different experimental setups that have been used and the assumptions that have been made. With respect to the equilibrium, Barker *et al.* have studied its manipulation through partitioning ions and have reported a useful Tafel relationship for k_2^+ and k_2^- . However, direct reading of the driving force in the present case is obstructed since their scale was defined with respect to the partitioning perchlorate ion¹⁶².

Despite the apparent simplicity of the developed model, as it did not include detailed microkinetics, thermodynamic parameters, or mass transport limitations, it exhibited a useful predicting power. It was not possible to find a feasible parameter set under the assumption that the total amount of TCNQ is initially uncharged. Therefore, we supposed that during the vesicle preparation a certain amount was reduced to TCNQ^- . By estimating the initial conditions, we found that approximately 85 % of the total TCNQ pool was in the form of a radical anion (Table 5.2). Indeed, the spontaneous reduction of TCNQ in Langmuir-Blodgett monolayers has been reported and discussed in terms of stabilizing effects of the lipid cationic head group and the interfacial hydroxyl group concentration¹⁶⁵. According to simulation results, TCNQ^- is rapidly reoxidized to TCNQ^0 when ferricyanide is added to the vesicle suspension, assuming a range of values for k_2^- ($1 \text{ M}^{-1} \text{ s}^{-1}$). This effect increases the pool of the active mediator and enables the oxidation of NADH, according to **Eq. 1**.

To determine the redox state of TCNQ in the present setup, we monitored the absorbance of rehydrated phospholipid suspensions before extrusion in the presence of the two oxidants (ferricyanide and oxygen). For these experiments, we used a 4-times higher TCNQ concentration (50:4 molar ratio between lipids and mediator) in order to magnify the respective signals. Neutral TCNQ in methanol exhibits a maximum at 395 nm, which corresponds to the

transition from the ground state to the first excited state ($S_0 \rightarrow S_1$) (Figure 5.11). In the case of the TCNQ anion, there are two main bands, one at 420 nm ($D_0 \rightarrow D_2$) and a broader one with two maxima at 740 and 840 nm ($D_0 \rightarrow D_1$), corresponding to doublet transitions due to the unpaired single electron¹⁰⁰. The spectrum of the suspension after rehydration revealed the characteristic TCNQ radical anion features: a pronounced band above 600 nm and a peak at 425 nm with a lower magnitude (Figure 5.12). This proved the spontaneous reduction during preparation, anticipated by the estimation of the initial conditions and previous observation¹⁶⁵. After the addition of 400 μ M ferricyanide to the sample, the peaks corresponding to $S_0 \rightarrow S_1$ or $D_0 \rightarrow D_2$ transitions could not be analyzed because they were masked by the oxidant, but the > 600 nm band was immediately reduced (< 1 s), which manifested the oxidation of TCNQ^- , as predicted by the model. In a parallel experiment, the initial TCNQ/lipid suspension was aerated with oxygen for 5 h. The decrease in the $D_0 \rightarrow D_1$ band (Figure 5.13) indicated TCNQ^- oxidation consistent with the outcome of the vesicle experiments (Figure 5.9).

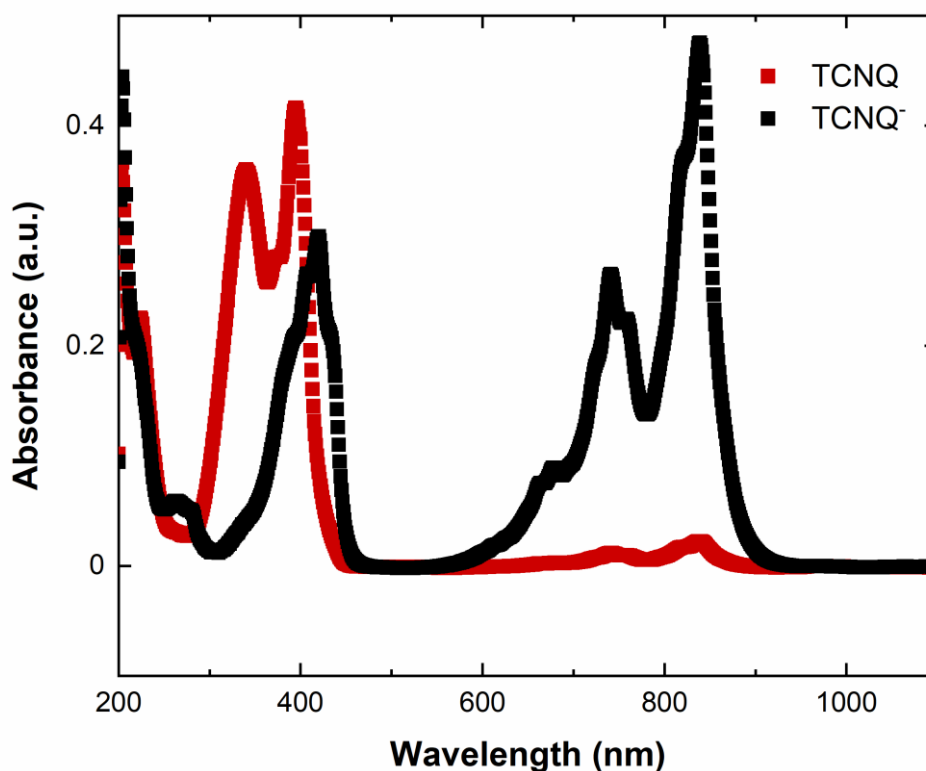
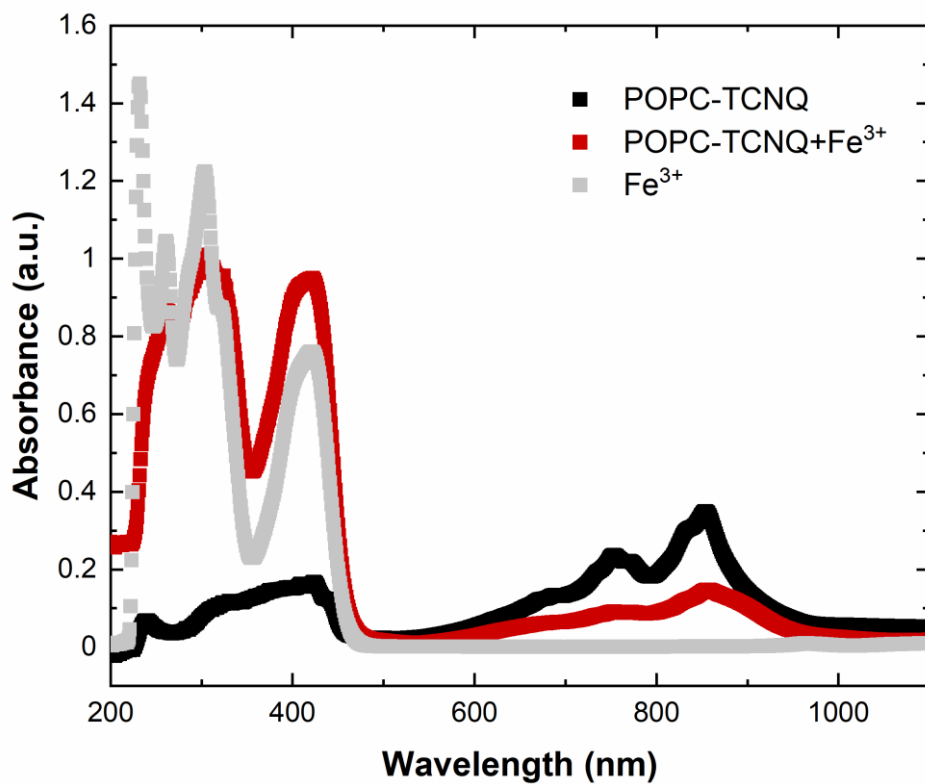


Figure 5.11 UV/Vis spectra of TCNQ and LiTCNQ in methanol.

Figure 5.12 UV/Vis spectra of hydrated POPC-TCNQ suspensions in the presence of 400 μM ferricyanide.

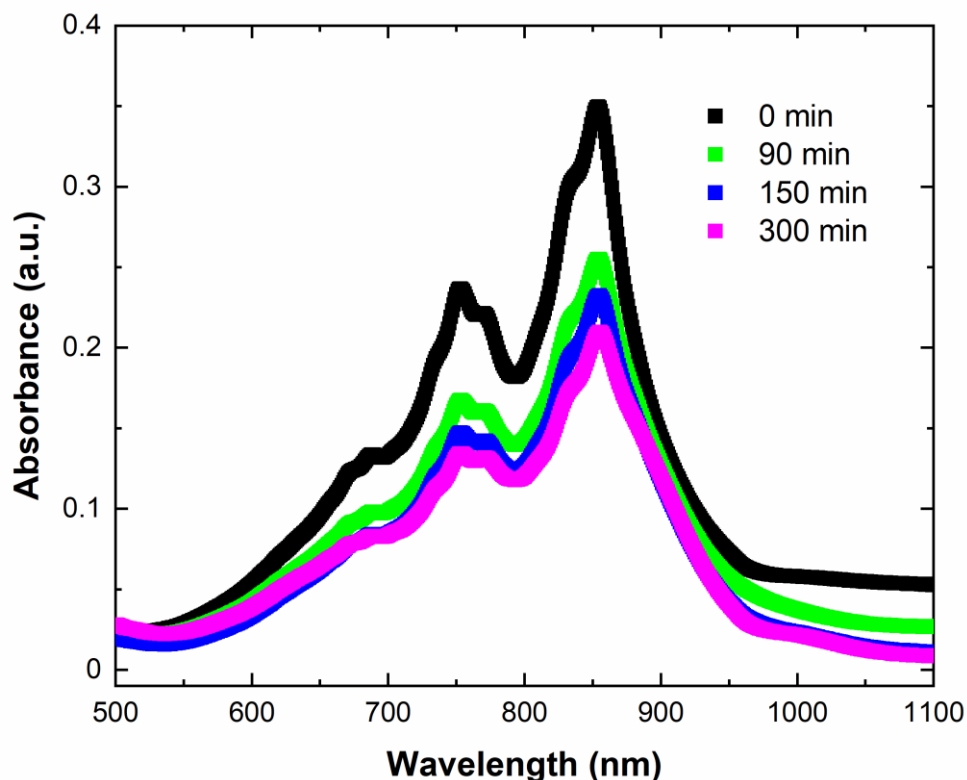


Figure 5.13 UV/Vis spectra of hydrated POPC-TCNQ suspensions during aeration with oxygen.

5.3.5 Characterization of TCNQ based LUVs with different amphiphiles

Next, we studied the effect of the membrane composition in vesicles containing different amounts of POPC and/or DOPC or PDMS-g-PEO at some hundreds of nm size. The vesicles were prepared by film hydration and extrusion, and DLS was used to determine the size distribution of these mixed vesicles, hybrids, and polymersomes. The results of extruded different vesicles indicated that all vesicles were monodispersed, and the z-average diameters of

these vesicles were all around ~ 120 – 185 nm which were matching the pore size of the filter membrane of the Avanti extruder. The polydispersity index (PDI) was much lower than 0.2, indicating a good quality of the result report (Figure 5.14). Moreover, the Derived Count Rates were in the same order of magnitude.

All hybrids' sizes were similar to each other, even with the different molar ratios of POPC and polymer. This is relatively smaller than pure POPC vesicles, shown to be 170 nm with and without incorporated TCNQ¹¹⁸. As demonstrated by the study of nanoscale hybrids composed of polybutadiene-*b*-poly(ethylene oxide) (PB-PEO) and POPC from S-K Lim and co-workers¹⁶⁶, the diameters of hybrids PB-PEO/POPC were also smaller than those of pure POPC vesicles. Interestingly, among these hybrids, the smallest hybrids were hybrids with a polymer/POPC molar ratio of 1:1, which was the same trend as in our results, with a value around 150 nm, while other hybrids were larger than 160 nm. Meanwhile, the smallest vesicles were PDMS-*g*-PEO polymersomes with diameters of 132 nm, which might be due to the relatively lower membrane strength of PDMS-*g*-PEO compared with POPC under the same applied extrusion pressure¹⁶⁷.

As well known, DOPC with two C=C bonds in the two C18 hydrocarbon tails has higher fluidity and higher lysis tension compared to POPC with one C=C bond in C18 and one saturated C16 chain¹⁶⁷⁻¹⁶⁹. Both lipids are in the fluid state at room temperature (The phase transition temperature of POPC and DOPC are -2.5 and -18.3 °C).

In general, one can conclude that the TCNQ incorporation has no significant effect on the size of the different vesicles.

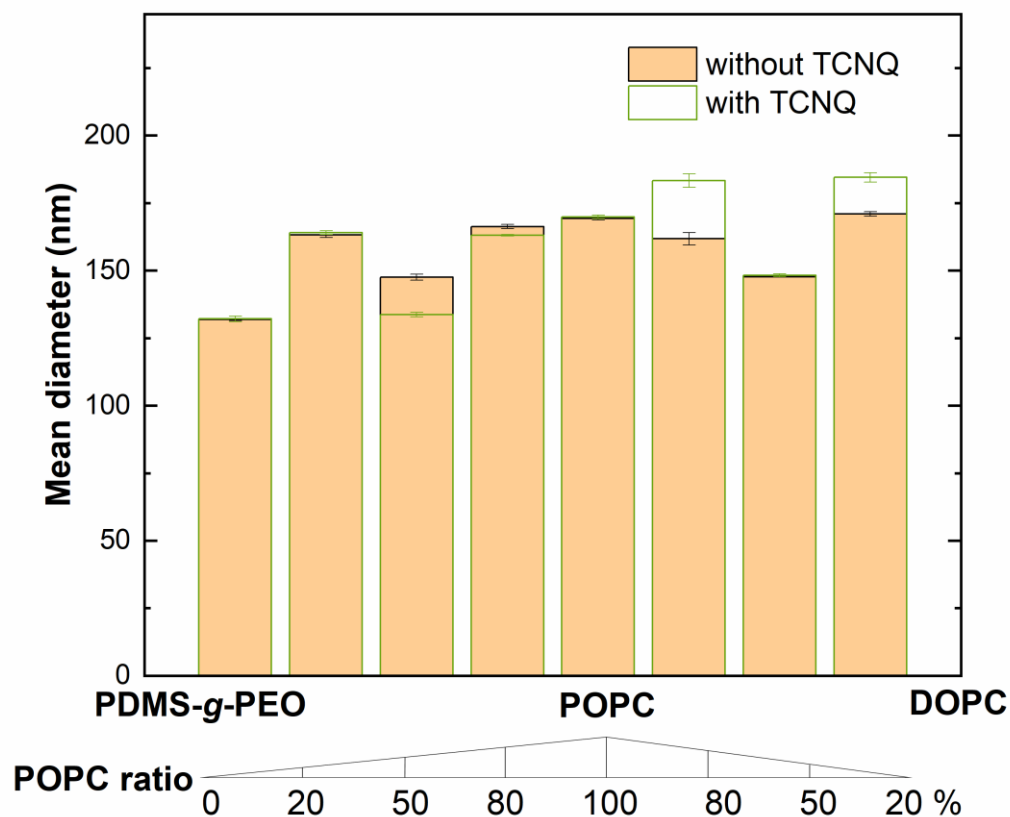


Figure 5.14 Mean diameter and standard deviation (S.D.) of different LUVs (all with encapsulation of NADH) with different compositions obtained from DLS.

Table 5.4 Size data for vesicles with TCNQ reconstituted and encapsulated NADH obtained from DLS.

Vesicles Containing:	Molar ratio	With/without TCNQ	Mean diameter (nm)
POPC	1:0	without	170
		with	170
POPC:DOPC	1:4	without	171

		with	185
POPC:DOPC	1:1	without	148
		with	148
POPC:DOPC	4:1	without	162
		with	183
POPC:PDMS-g-PEO	1:4	without	163
		with	164
POPC:PDMS-g-PEO	1:1	without	148
		with	134
POPC:PDMS-g-PEO	4:1	without	166
		with	163
PDMS-g-PEO	1:0	without	132
		with	132

5.3.6 NAD⁺ regeneration in TCNQ based LUVs with different amphiphiles

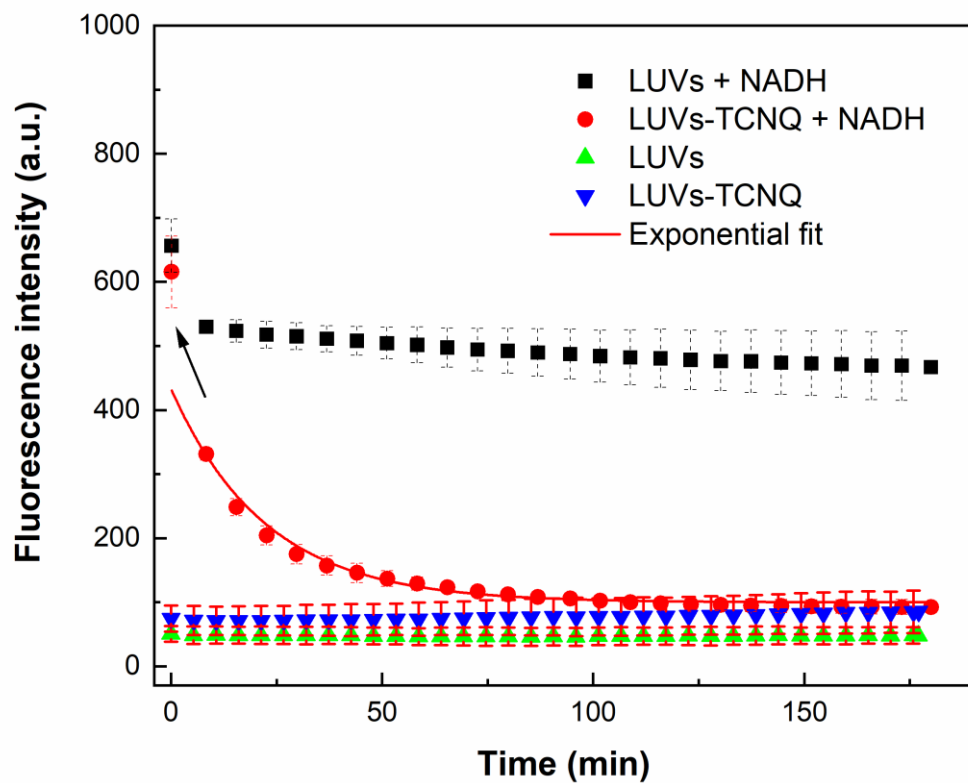
Next, we tested and compared the time courses of fluorescence intensity change of NADH encapsulated in all different vesicles (mixed vesicles (MV), hybrid vesicles (H), and polymersomes (P)) with and without incorporated TCNQ and in the presence of ferricyanide. For vesicles containing TCNQ but no NADH, we obtained the background fluorescence signal of vesicles. The results about the different hybrid vesicles (H1:4, H1:1, H4:1) and polymersomes are shown in Figure 5.15. Time-dependent data of NADH oxidation by TCNQ and external ferricyanide were fitted by a single exponential decay function. It also allowed discriminating the initial transmembrane kinetics from the oxidation of insignificant amounts of non-encapsulated NADH, as the first point with steep drop was excluded from the fitting procedure which in turn may have led to a slight underestimation of the rates.

As a negative control, all vesicle constructs containing NADH but no TCNQ were also tested by adding ferricyanide to confirm that no potential leakage of NADH from different vesicles happened. However, for hybrids composed of the same molar of POPC and PDMS-g-PEO (H1:1) and polymersomes composed of only PDMS-g-PEO, the negative control tests of H1:1 and polymersomes exhibited exponential decays. Particularly at H1:1, the result was similar to the actual test with TCNQ (Figure 5.15 B). Although bleaching and degradation can also be described by an exponential decay function, the comparison with the respective controls of the other compositions indicated a possibly compromised vesicle stability. Additionally, we anticipated that for lipid/polymer hybrids containing ≥ 50 mol% POPC, the potential leakage can be ascribed to membrane defects due to spontaneous phase separation.³⁸

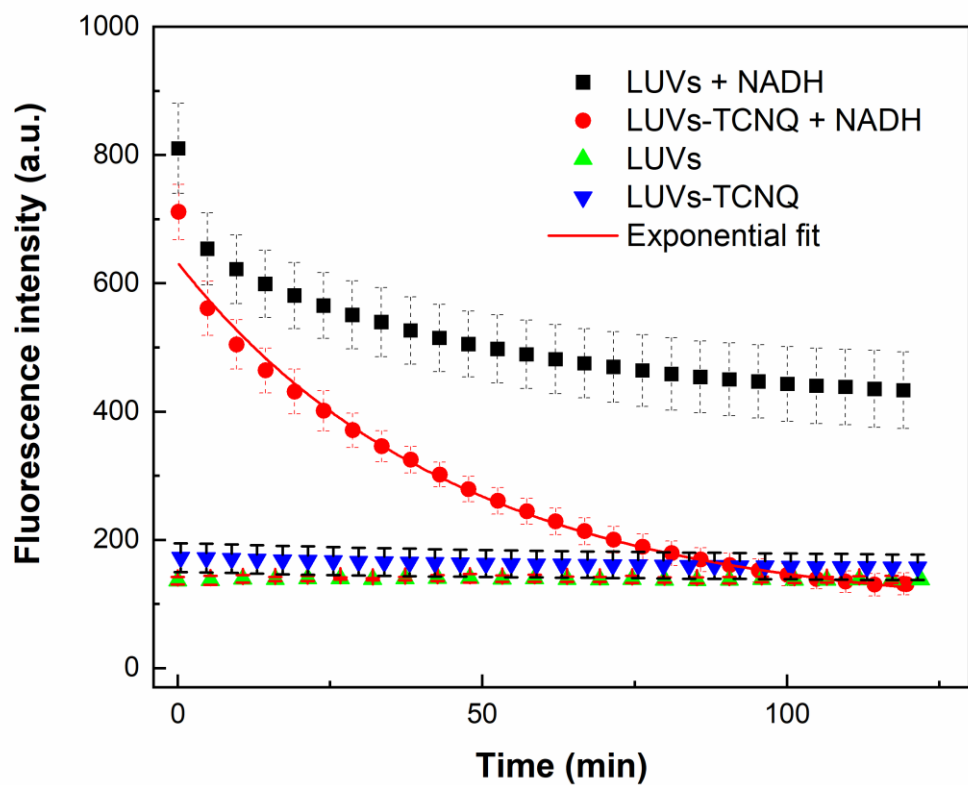
170

Based on the fitting function, $F = F_0 + A \exp(-R_0 \cdot x)$, where F_0 corresponds to the background fluorescence intensity of different vesicles, A the initial quantity and R_0 the decay rate, the NADH oxidation in H1:4 vesicles was most efficient ($7.5 \times 10^{-4} \text{ s}^{-1}$), compared to the R_0 values $3.7 \times 10^{-4} \text{ s}^{-1}$ for H1:1, $4.9 \times 10^{-4} \text{ s}^{-1}$ for H4:1, and $5.7 \times 10^{-4} \text{ s}^{-1}$ for polymersomes. The increasing polymer content was associated with a growing membrane disorder, evidenced by the bilayer probe Laurdan¹⁰⁸, which would increase the exposure of TCNQ to ferricyanide and NADH, though we could not evidence exactly the location of TCNQ. Thus, for vesicles composed of more polymers than POPC (H1:4, polymersomes), the decay rate was relatively higher. Furthermore, considering the homogeneous distribution without phase separation of POPC and PDMS-g-PEO in hybrid H1:4 membranes (polymer 80 mol%), H1:4 demonstrates better compatibility, stability, and membrane integrity than H1:1 and H4:1 (assumed as heterogeneous due to possible phase separation). As for the polymersomes, the lower membrane fluidity possibly dominated the exposure effects¹⁷¹⁻¹⁷².

A H1:4



B H1:1



C H4:1

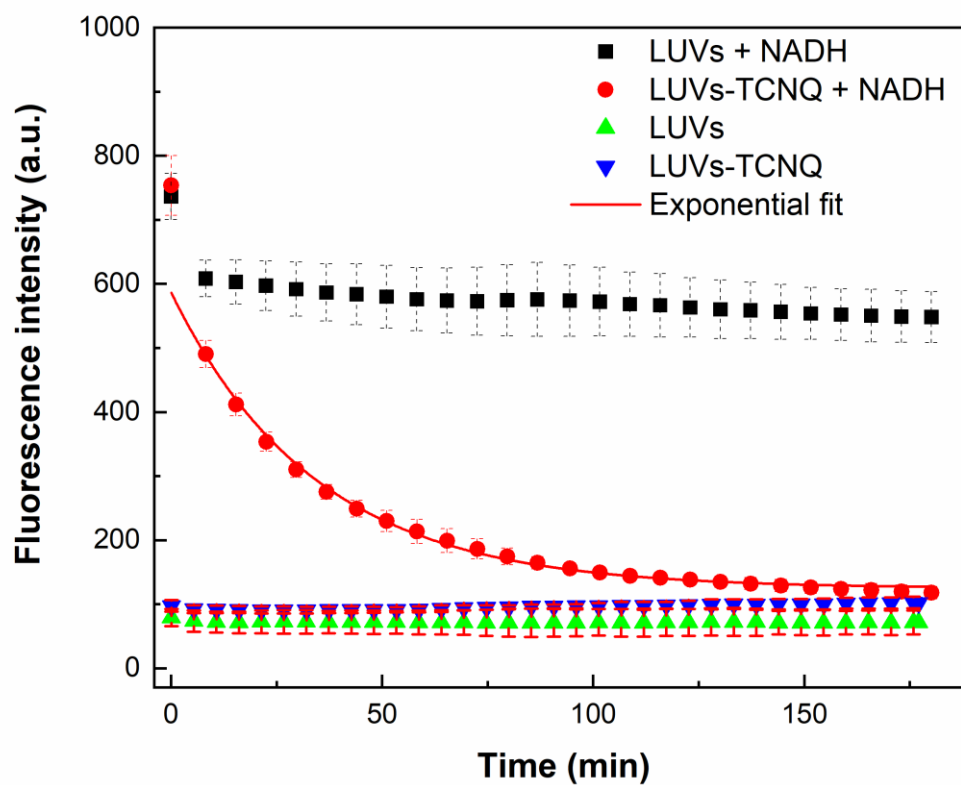
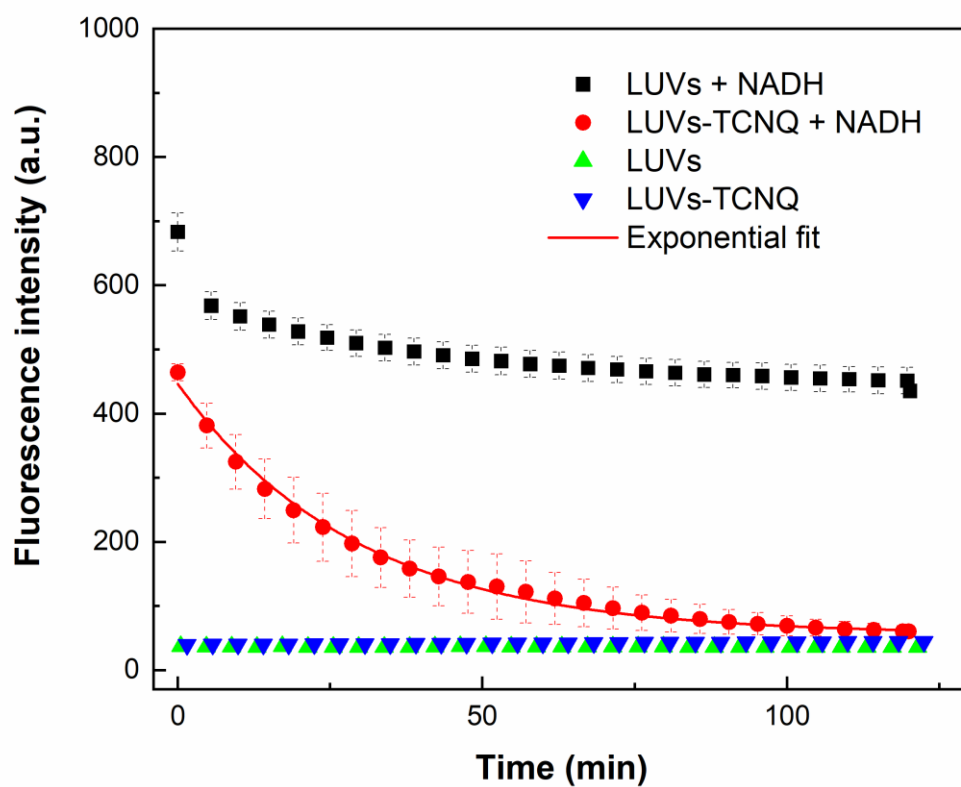
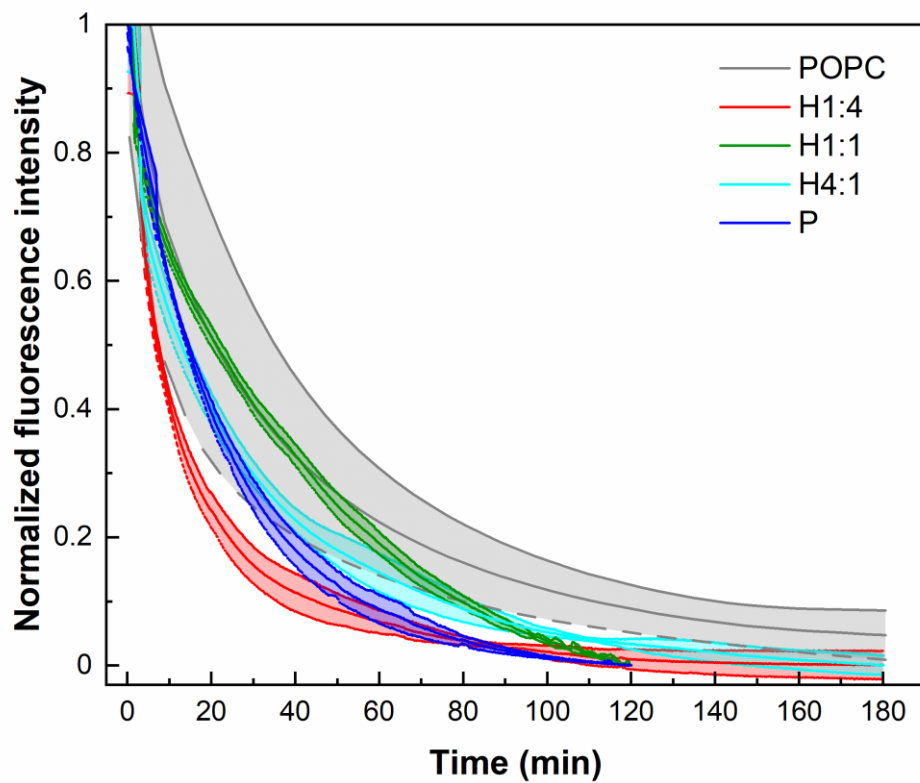
D PDMS-*g*-PEO

Figure 5.15 Time courses of fluorescence intensity profiles of bare and functionalized vesicles at different compositions, in the absence and presence of 400 μM potassium ferricyanide.

For better comparison of the efficiencies of NADH oxidation, the fluorescence intensities of NADH in different hybrids were normalized as shown in Figure 5.16 A, and for the mixed vesicles (MVs) containing POPC and DOPC, the same normalization is shown in Figure 5.16 B. The data for POPC vesicles obtained from previous work was also fitted (R_0 value of $4.2 \times 10^{-4} \text{ s}^{-1}$), then normalized and included too. It implies apparently that H1:4 was more efficient than POPC vesicles. Conversely, in the case of MVs (Figure 5.16 B), without any leakage of NADH under negative control test, MV 4:1 (Figure 5.16 B, cyan) worked better than MV1:4 and MV1:1. Yet, MV1:4 works similarly with POPC vesicles, and MV1:1 works least efficiently which might suggest that lipid asymmetry affects the lipid layer fluidity in MV.^{169, 172} Nevertheless, the efficiency of NADH oxidation in MV 4:1 was slightly lower than in H1:4 (Figure 5.16 B, light red).

A)



B)

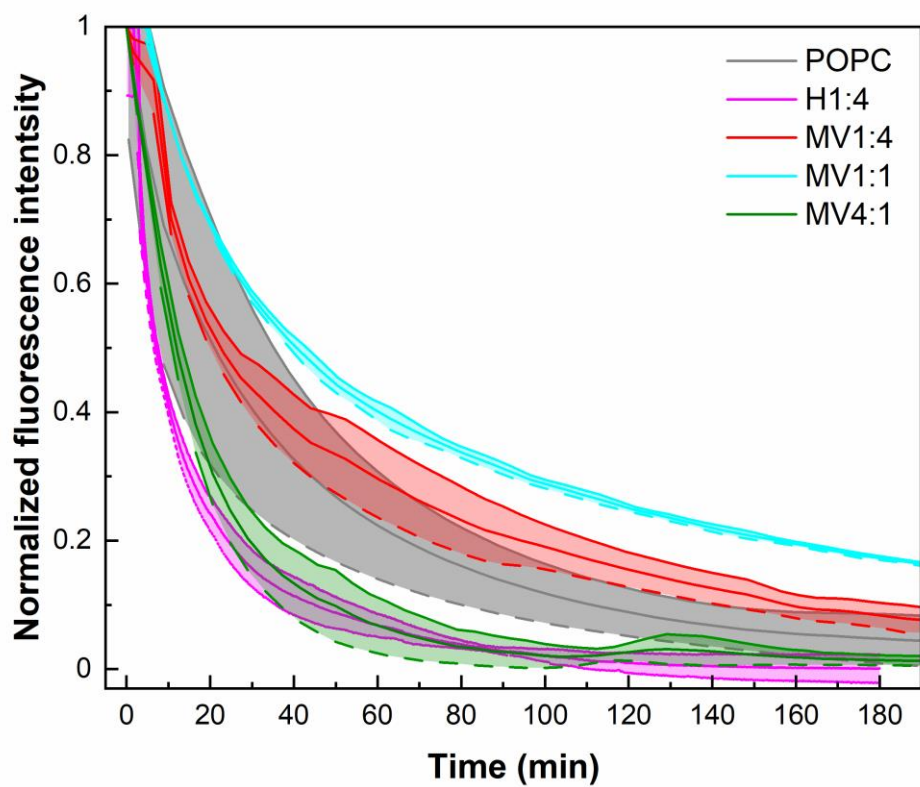


Figure 5.16 Time courses of normalized NADH fluorescent intensity profiles monitored by a fluorescence spectrometer in different nm-scale vesicles with TCNQ incorporated after 400 μM ferricyanide being added at $t = 0$.

5.3.7 Leakage test

To rule out the possibility of NADH released from LUVs through membrane defects due to the presence of TCNQ, the leakage test was run with carboxyfluorescein (CF) as a mark instead of NADH being encapsulated in TCNQ based LUVs. Although the de-quenching of NADH has been previously used to determine the liposome stability against ethanol¹²⁸, we did not observe a sufficient increase in fluorescence intensity after disrupting the vesicles with surfactants (about 7% difference at 460 nm) to be able to quantify the possible leakage of NADH. In contrast, carboxyfluorescein (CF) as a commonly used dye for testing about leakage of vesicles exhibits sharp self-quenching (Figure 5.17) and is therefore used as standard method for the assessment of liposome stability and permeability¹⁷³. On the basis of the experimental limitations of direct NADH monitoring on one side and the established use of the CF assay on the other side, alongside the smaller size of CF compared to NADH, we evaluated the influence of TCNQ on membrane permeability through CF as a model for encapsulated species. In triplicate experiments, the dye fluorescence was monitored over 13 h, and afterward 1% octyl glucoside (OG) was added in order to disrupt the vesicles and achieve complete release and de-quenching. CF is known to spontaneously leak from POPC vesicles at a low rate, but the precise mechanism is unknown¹⁷⁴. The presence of TCNQ in the membrane resulted in a slight increase in content release (Figure 5.18), which could not account for the observed NADH oxidation rate. In a relevant time frame of 5 h, vesicles with 50:1 and 25:1 ratios of POPC/TCNQ exhibited 5.6 ± 2.3 and $4.1 \pm 1.6\%$ releases, respectively, while pure POPC liposomes released $2.2 \pm 0.9\%$ of their content.

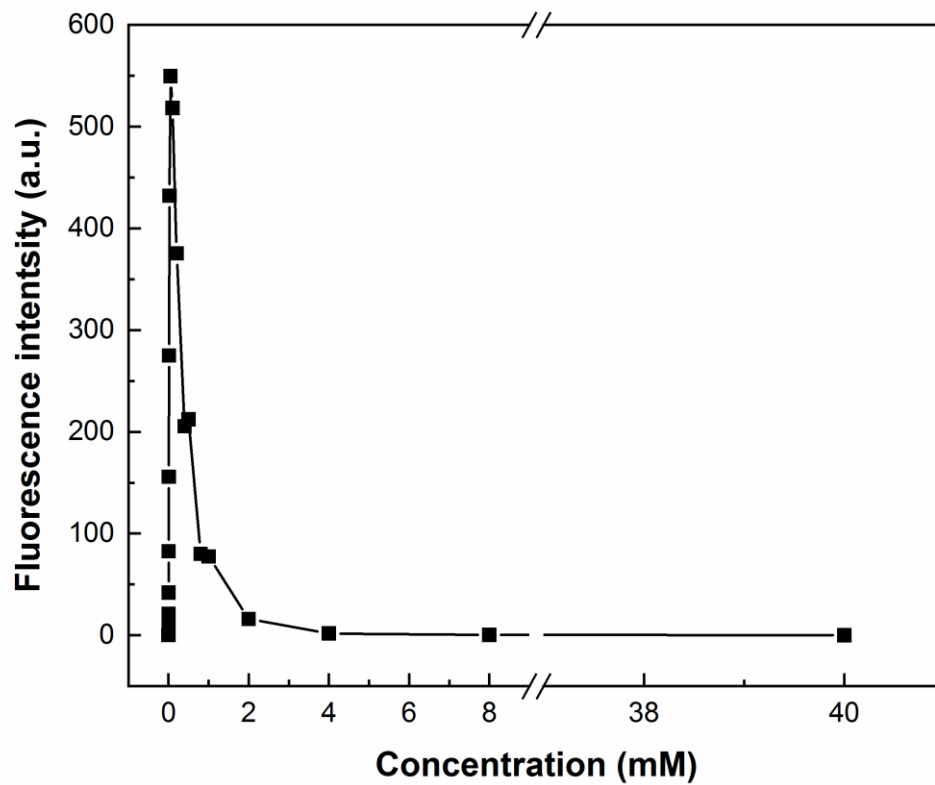


Figure 5.17 Fluorescent intensity in dependence on the carboxyfluorescein (CF) concentration at an excitation wavelength of 494 nm and an emission wavelength of 524 nm (both slit width at 2.5).

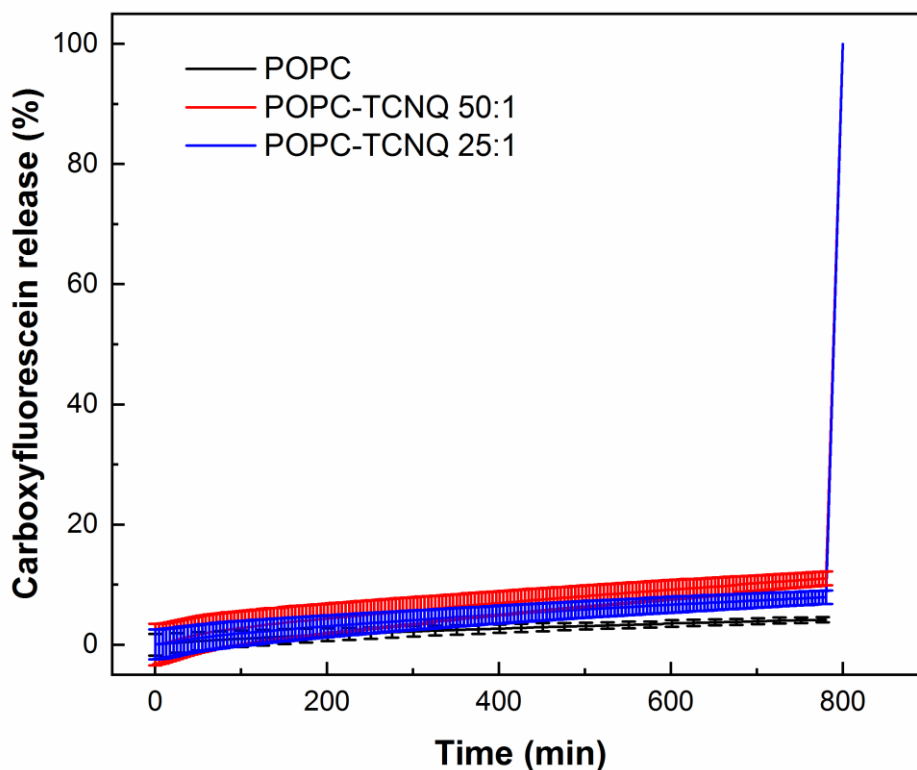


Figure 5.18 Fluorescence courses of carboxyfluorescein encapsulated in POPC LUVs at 524 nm without or with embedded TCNQ in 100 mM MOPS, 250 mM KCl, Tris, pH 7.2.

Considering no NADH leakage out of TCNQ-functionalized POPC vesicles and H1:4 hybrids, we explored the potential diffusion of ferricyanide into vesicles. Consequently, ferricyanide was added to empty POPC vesicles and H1:4 with the total amphiphile ratios to TCNQ of 50:1, 25:1, and the final concentration of ferricyanide was 20 mM. After staying overnight at room temperature, these vesicles underwent gel filtration to remove out-membrane ferricyanide, and then the purified vesicles were collected and evaluated. As shown in Figure 5.19, ferricyanide absorbs at maximum around 420 nm, however, all vesicles with different TCNQ amounts showed no absorption peak at this value. Taking account of the turbidity of vesicles at nm-size scale, the low absorption value at 420 nm (< 0.05 a.u.),

corresponding to around 62.5 μM pure ferricyanide concentration), ferricyanide with the concentration lower than 62.5 μM would not be detected. Nevertheless, comparing the initially added concentration of ferricyanide (20 mM), we can conclude that virtually no ferricyanide diffused into those vesicles. Consequently, NADH oxidation in H1:4 hybrids would only rely on TCNQ.

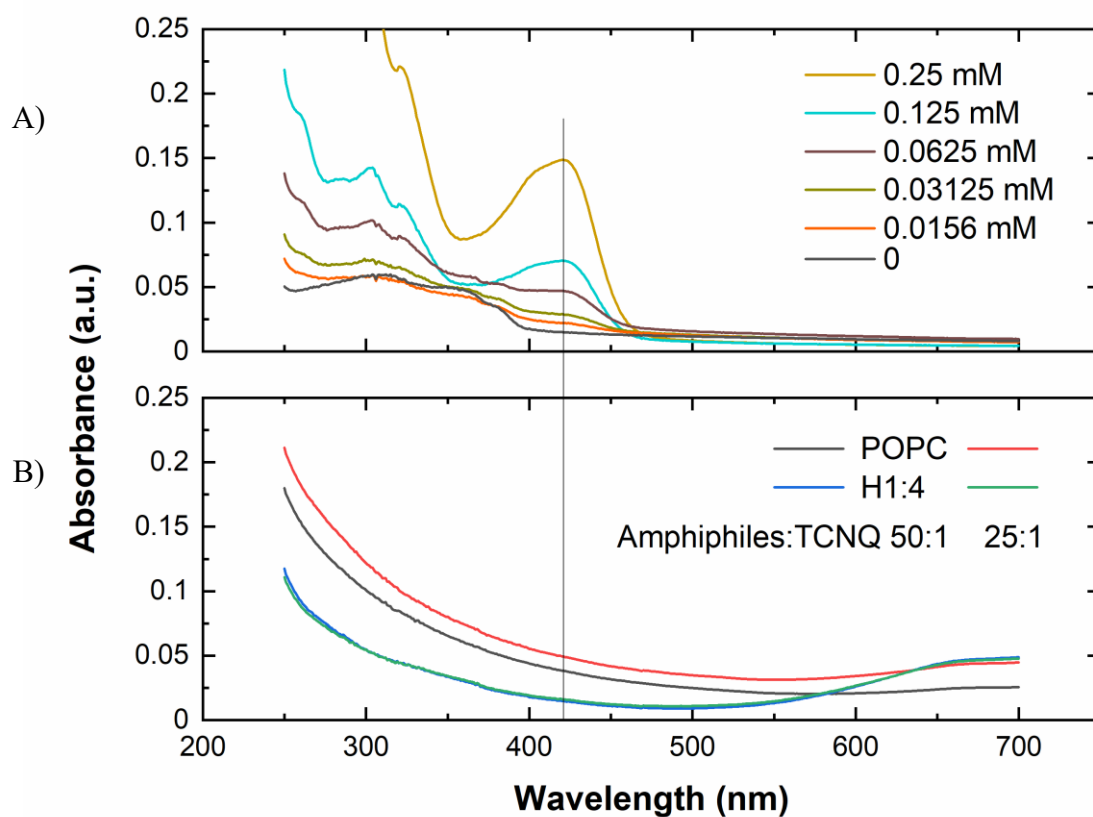
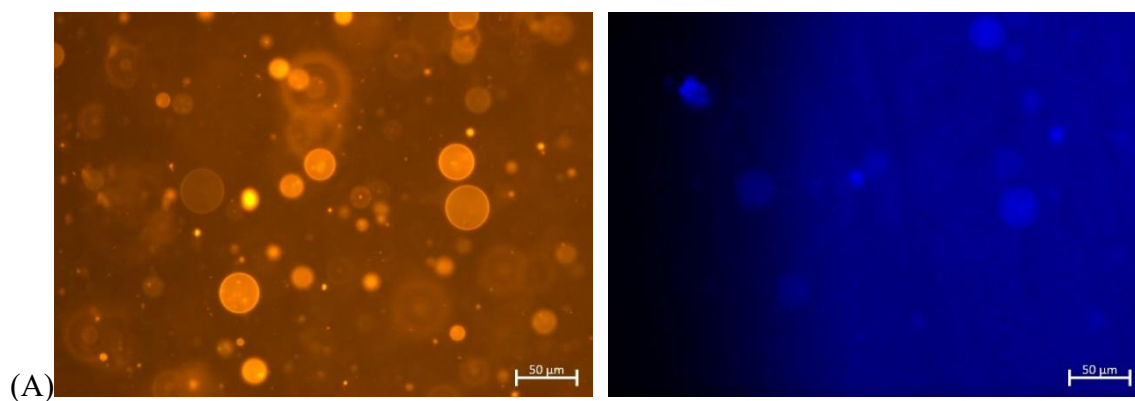


Figure 5.19 UV-Vis spectra of ferricyanide with different concentrations (A) and purified vesicles (POPC, H1:4) with different amounts of TCNQ (B). Line: 420 nm.

5.4 NAD⁺ regeneration in GUVs

5.4.1 Characterization of different GUVs

Fluorescence images of different micron-scale vesicles (GV, GH1:4, GMV1:4) both containing NADH and TCNQ and prepared by electroformation are shown in Figure 5.20. As suggested by previous research, GH1:4 exhibits the homogeneous distribution of POPC and PDMS-*g*-PEO without forming raft-like lipid domains or budding to form pure vesicles and polymersomes^{36, 175}. As illustrated in Figure 5.20 (B) left, GH1:4 were well-formed and showed no lipid domains but some bright points which is due to spontaneous curvature also present in GV and GMV¹⁷⁶. Electroformation resulted in a wide size distribution, but most GUVs had an average size of around 20 μm . Meanwhile, NADH fluorescence was detected as shown in Figure 5.20 right. Toward this, the GUVs were all diluted with glucose, which decreased the outside NADH concentration and also helped GUVs with sucrose inside the membrane to settle down and concentrate. This increased also the phase contrast of vesicles.



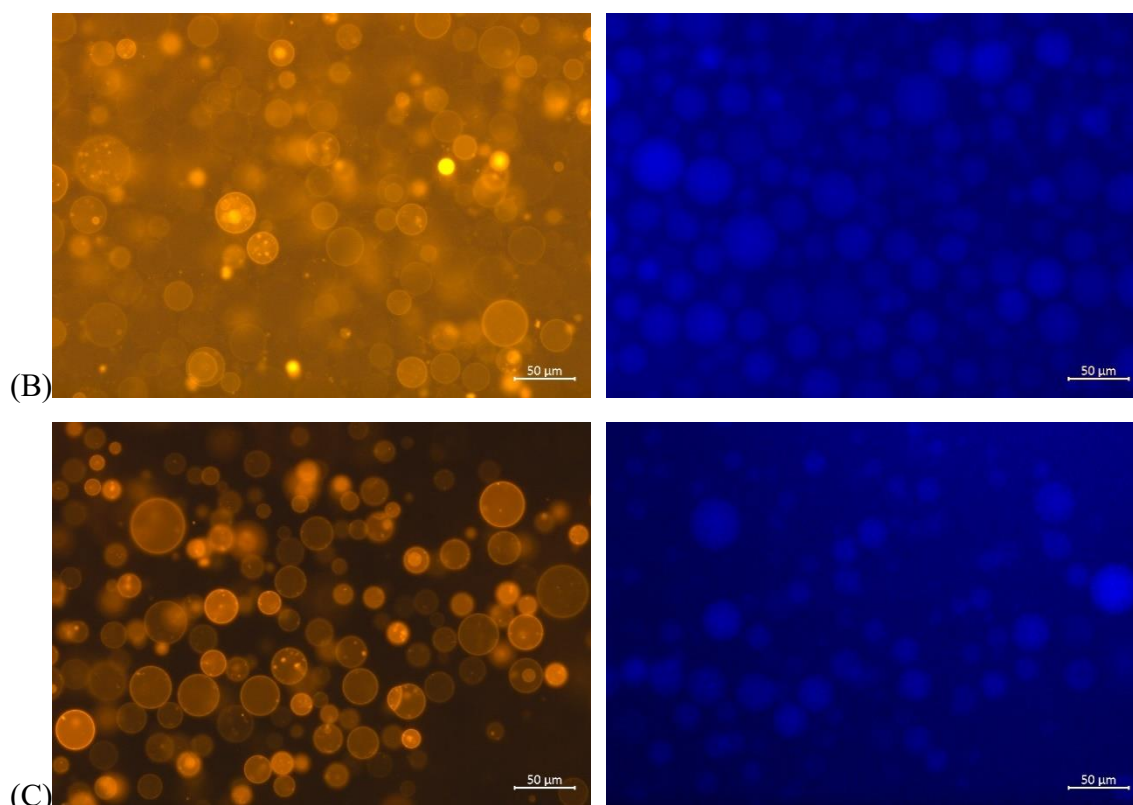


Figure 5.20 Fluorescent images of different vesicles (A) GV, (B) GH1:4, (C) GMV1:4 with TCNQ incorporated and NADH encapsulated (left: red fluorescence of PE-Rho, right: blue fluorescence of NADH) (scale bar: 50 μm).

5.4.2 NAD⁺ regeneration in different TCNQ based GUVs

After adding ferricyanide to NADH encapsulated and TCNQ incorporated vesicles (GV, GH, or GMV), NADH oxidation by ferricyanide mediated with TCNQ was further imaged by use of inverted fluorescence microscopy. Since NADH is readily bleached during the prolonged focusing, it was virtually impossible to monitor the NADH oxidation under conventional epifluorescence microscopy. Therefore, the images of different vesicles shortly (in the order of several minutes) after adding a high concentration of ferricyanide (2–10 mM) were taken to avoid long imaging. As shown in Figure 5.21, it was found that after adding ferricyanide (> 3 min) the fluorescence of NADH decreased significantly. Meanwhile, most large GUVs ruptured which indicated adsorption of GUVs to the glass surface except little

small-sized GUVs ($< 10 \mu\text{m}$) and remained as dried films of lipid (arrows on the left side in Figure 5.21). Comparing with the image of phase contrast in the middle in Figure 5.21, few vesicles remained intact (the arrows). Only a small portion of the vesicles remained unaffected, which was ascribed to the presence of multivesicular vesicles and the potentially non-uniform distribution of TCNQ. As already demonstrated in a previous work¹¹⁸, NADH oxidation would generate protons, and with the consumption of NADH to generate NAD^+ , the rupture of giant vesicles was mainly due to the pH and high ionic strength inside the vesicle which induced the fusion of vesicles to glass surfaces.¹⁷⁷ In fact, upon direct oxidation of 1 mM NADH by a 20-fold excess of ferricyanide in bulk, the pH decreased from 5.5 to 4.2. Besides, this rupture of vesicles would release encapsulated NADH and make it difficult to recognize NADH fluorescence (right side in Figure 5.21).

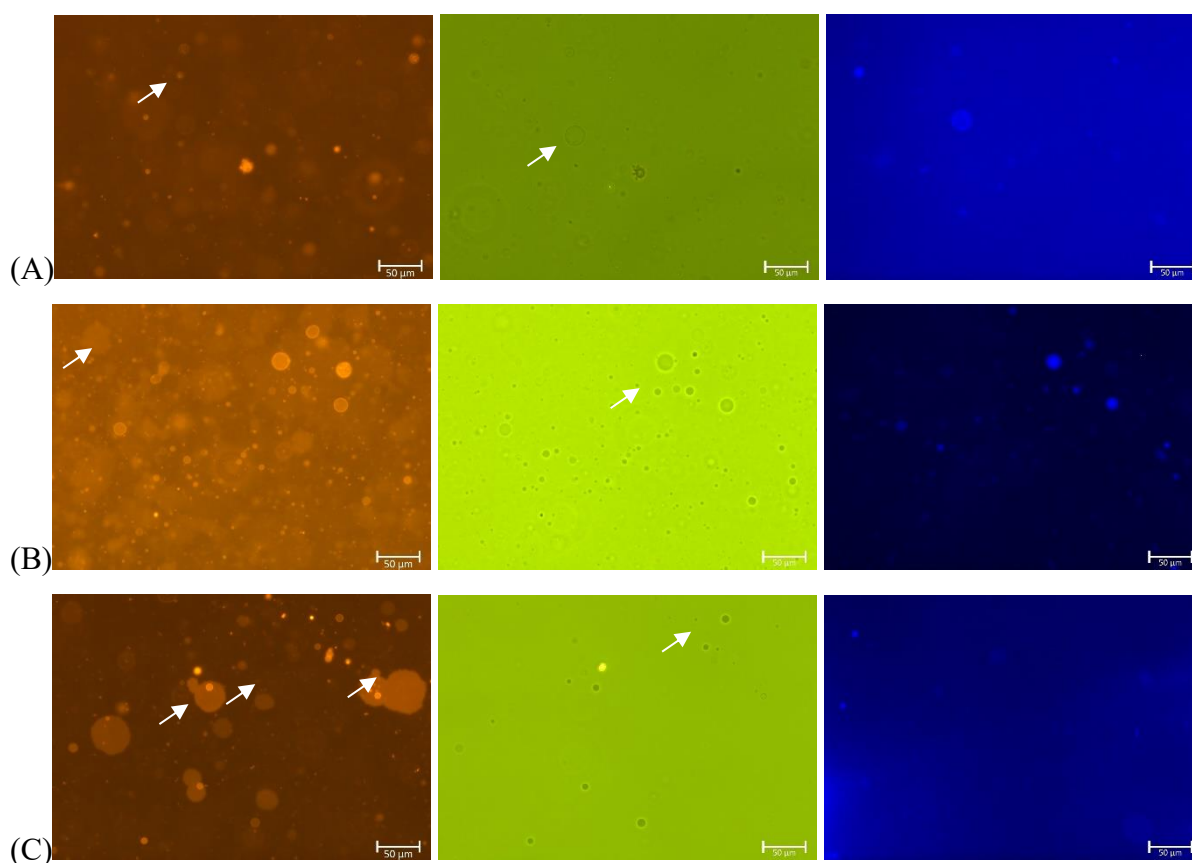


Figure 5.21 Fluorescent images of (A) GV, (B) GH1:4, and (C) GMV with TCNQ incorporated and NADH encapsulated after adding 10 mM ferricyanide (left: red fluorescence of PE-Rho, middle: phase contrast, right: blue fluorescence of NADH) (scale bar: 50 μm).

Aiming to follow giant vesicles and monitor the process of NADH oxidation in vesicles, we used CLSM to study the change of NADH fluorescence intensity in GH1:4. Firstly, CLSM images of GV, GH1:4 are shown in Figure 5.22. The GH1:4 did not exhibit membrane protrusions and the encapsulation was more uniform in comparison to GV¹⁷⁸. The formation of buds and tubes in lipid bilayers is due to the excess area and the spontaneous curvature, which in turn is affected by the solute asymmetry among other factors. Different salt and sugar concentrations across the membrane were present in the current system as well, but the predominant polymer self-assembles into a soft bilayer, which appears to be less responsive to the unbalanced conditions. On the other side, the low encapsulation efficiency of large and charged molecules is a known drawback of both the spontaneous and the electrically assisted swelling of lipid films¹⁷⁹. In the case of hybrids though, NADH evidently penetrates better into the amphiphile film during the formation, possibly due to a less organized multilayer structure. In both types of GUVs, the intensity of the membrane fluorescence varied significantly. This can be partially ascribed to positioning out of the focal plane or focus instabilities during image acquisition between channels (tiny focus drift), but the potentially non-uniform distribution of the lipid dye should not be discounted.

After adding 10 mM ferricyanide, one GH1:4 was followed and monitored via time-lapse. The results are shown in Figure 5.23. The rupture of GH1:4 with irregular shape was also evidenced 2 min after adding ferricyanide. Additionally, when reading the gray value with corresponding NADH intensity, it decreased significantly from 250 units short after adding ferricyanide to ~ 100 and further to ~ 55 , which corresponds to the background signal (~ 51). From exponential decay curve fitting, the relationships of the gray value with time were $F = 51 + 198.5 \exp(-0.07 t)$, with the absolute value of $R_0 = 0.07 \text{ s}^{-1}$.

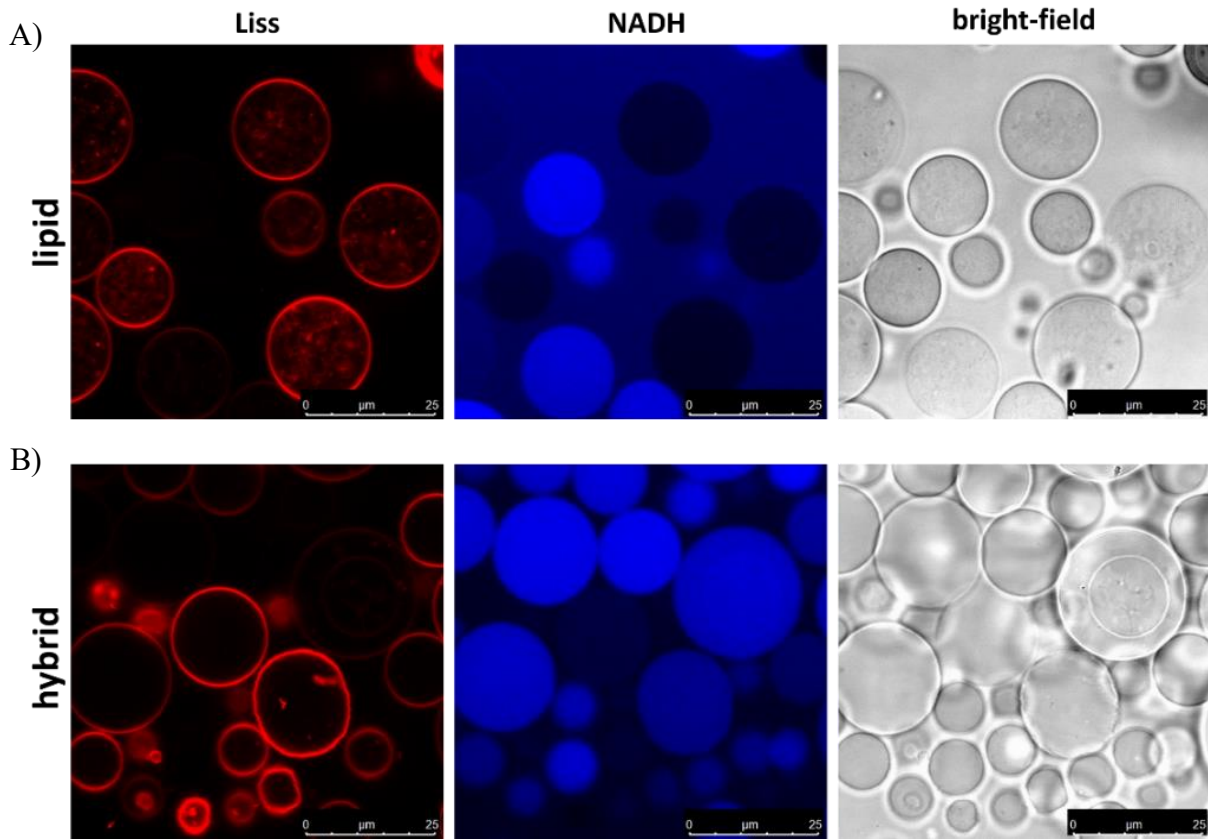


Figure 5.22 CLSM images of GV (A) and GH1:4 (B) with TCNQ incorporated and NADH encapsulated (left: fluorescence of PE-Rho, middle: fluorescence of NADH, right: bright field) (scale bar: 25 μm).

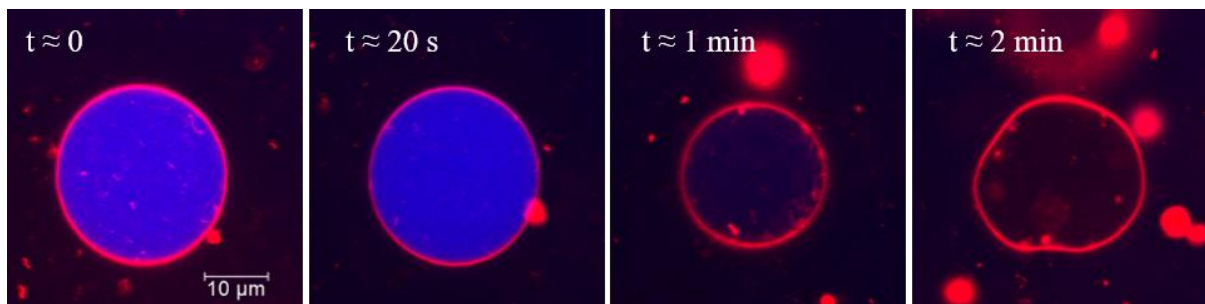
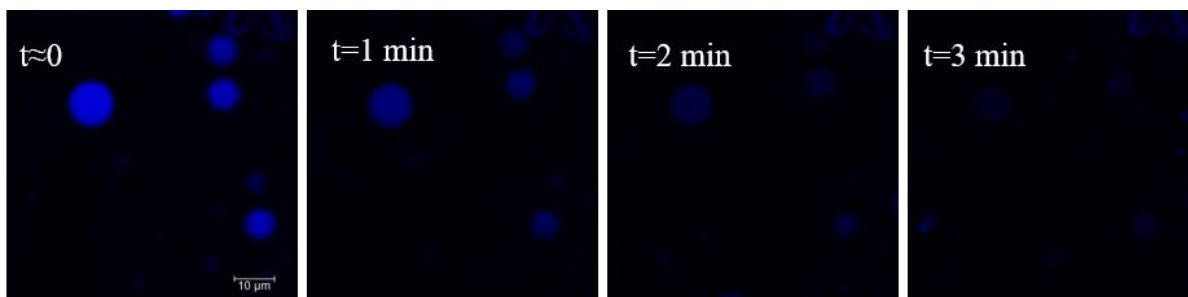


Figure 5.23 Time-lapse of NADH in GH1:4 CLSM images after adding 10 mM ferricyanide (red: fluorescence of PE-Rho, cyan: fluorescence of NADH), scale bar: 10 μm.

For a more detailed investigation, fluorescent images of NADH in more GH1:4 were recorded by CLSM, and the images are shown in Figure 5.24 (A). By the significant decrease of NADH fluorescence, NADH oxidation by TCNQ mediation after adding 2 mM ferricyanide in GH1:4 was evidenced directly. Considering fast rupture of giant vesicles and potential slight bleaching of NADH, time-lapse of NADH oxidation in GH1:4 was recorded by extracting images every 10 seconds, and a relatively lower concentration (2 mM) of ferricyanide was added. The corresponding normalized mean gray value was plotted in average and fitted with an exponential decay curve (Figure 5.24, lower panels). With different initial encapsulation of NADH in different GH1:4, the mean values were different at the beginning, but the relationship of the gray value with the decay time was comparable to each other. After normalization, the absolute value of R_0 was $1.3 \times 10^{-2} \text{ s}^{-1}$ which is much higher than in LUVs due to the high concentration of ferricyanide and the relatively lower concentration of NADH inside GUVs (max. 1 mM as initially added). As for GV, unfortunately, no comparable data were obtained by CLSM due to the difficulties during the operation procedure for imaging, potential bleaching of NADH, and their relatively lower encapsulation efficiency.

Overall, CLSM indeed allowed monitoring of NADH, and the transmembrane oxidation proceeded faster (within a few minutes) compared to the nano-size scaled vesicles due to the different ratio of ferricyanide to NADH. The amount of encapsulated cofactor was limited by the preparation procedure, and we deliberately employed a higher oxidant concentration to accelerate the process and avoid long imaging. However, the resulting narrow time window for locating the GUVs and adjustment of imaging parameters made it difficult to analyze sufficient GUVs. Altogether, the mass transport conditions in the microscopic slide could not be controlled, which resulted in exposure to different ferricyanide concentrations at different times. Still, little bleaching of NADH prevented precise quantification also in the CLSM setup (though not as pronounced as with conventional epifluorescence) due to the inability to discriminate it from the oxidation events.

A)



B)

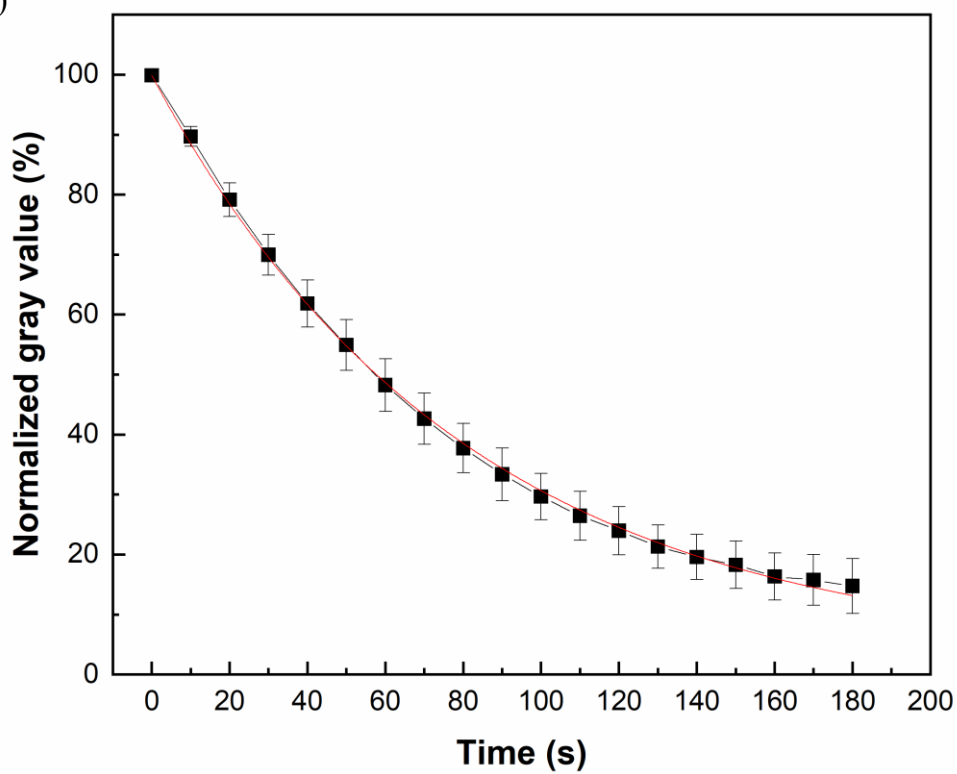


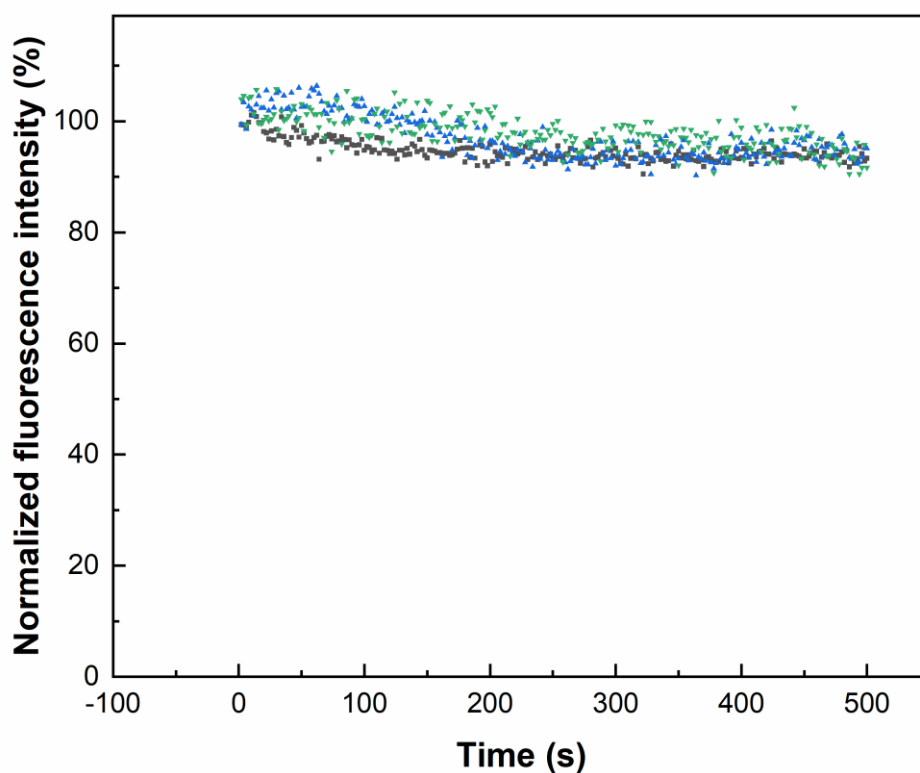
Figure 5.24 Time-lapse of NADH (blue) in GH1:4 CLSM images after adding 2 mM ferricyanide (A) from left to right shows $t \approx 0$, $t = 1 \text{ min}$, $t = 2 \text{ min}$, $t = 3 \text{ min}$ (scale bar: $10 \mu\text{m}$) and their corresponding normalized gray value in average profiles of GH1:4 (B).

To avoid NADH bleaching, time-correlated single-photon counting wide-field microscopy with higher sensitivity of a microchannel plate photomultiplier tube for single-photon counting under low illumination was used to monitor GUVs with different control tests with and without the TCNQ effect on the NADH fluorescence intensity change. With this imaging technique, we did not get feasible data for GH1:4 hybrids, due to the faster decay rate as observed by CLSM. However, more precise quantification of NADH in GV was obtained, as shown in Figure 5.25. With evidence of no significant change of NADH fluorescence intensity traces in GV encapsulated with NADH and without TCNQ either with or without the addition of ferricyanide, negligible bleaching of NADH was detected due to the mild excitation by short laser pulses (averaged laser power $< 5 \text{ MW cm}^{-2}$). In addition, GV with TCNQ before adding ferricyanide implies insignificant change compared with their behavior after adding ferricyanide (Figure 5.25 D). For details, the images of GV with NADH encapsulated and TCNQ reconstituted after adding ferricyanide (original images used for normalization as shown in Figure 5.25 D) are shown in Figure 5.26. To analyze the fluorescence intensity of NADH in GV from the images, all GV were identified, and their sizes and the initial intensity values were compared (Figure 5.27). Based on statistical analysis, for GV under the size of 15 pixels, the initial fluorescence intensity of most GV was lower than 30000. The relationship of initial fluorescence intensity of GV with their diameters was $I_0 = 513.5 \cdot \text{diameter} - 3836$ ($R^2 = 0.57674$), as plotted in Figure 5.28 (A). Based on the photon counting, in larger GV more NADH would be encapsulated, thus more photons would be detected. After adding ferricyanide, with highly irregular diffusion (onsets could not be correlated to the position of GV) and without any available hydrodynamic control, we cannot exclude the contribution of forced mass transport, despite the efforts to add the oxidant as gently as possible. Therefore, the starting point of NADH oxidation was not exactly fixed. However, with the exponential fitting of the decay section of the GV, the corresponding decay rate of NADH is summarized in Figure 5.28 lower, staying around $0.028 \pm 0.018 \text{ s}^{-1}$ on average.

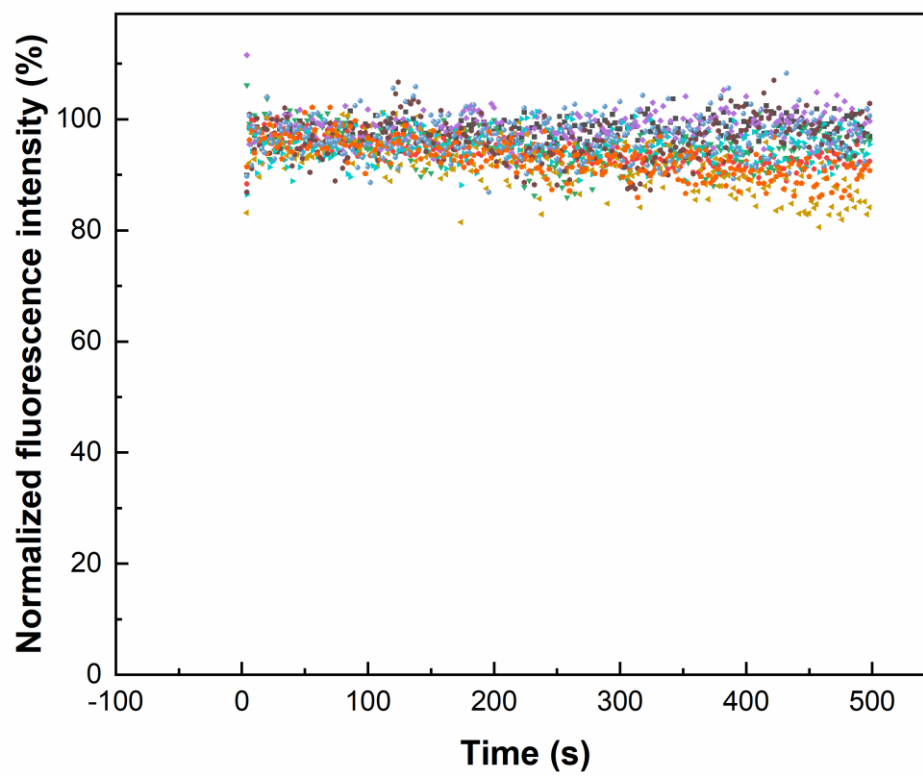
Unlike the bulk nanoscale LUVs analysis, which evaluates entire populations, monitoring individual GUVs provides a finer level of detail. In fact, observation of single nanovesicles has been reported several times, e.g. for deeper analysis of proton permeation by total internal reflection fluorescence (TIRF) microscopy¹⁸⁰. However, the optical access at the

micron scale potentially enables the correlation of activity with additional factors such as size, number of lamellae, membrane protrusions, etc. Furthermore, the oxidant supply could be more precisely controlled in future experiments by the use of hydrodynamic trapping in microfluidic devices¹⁸¹.

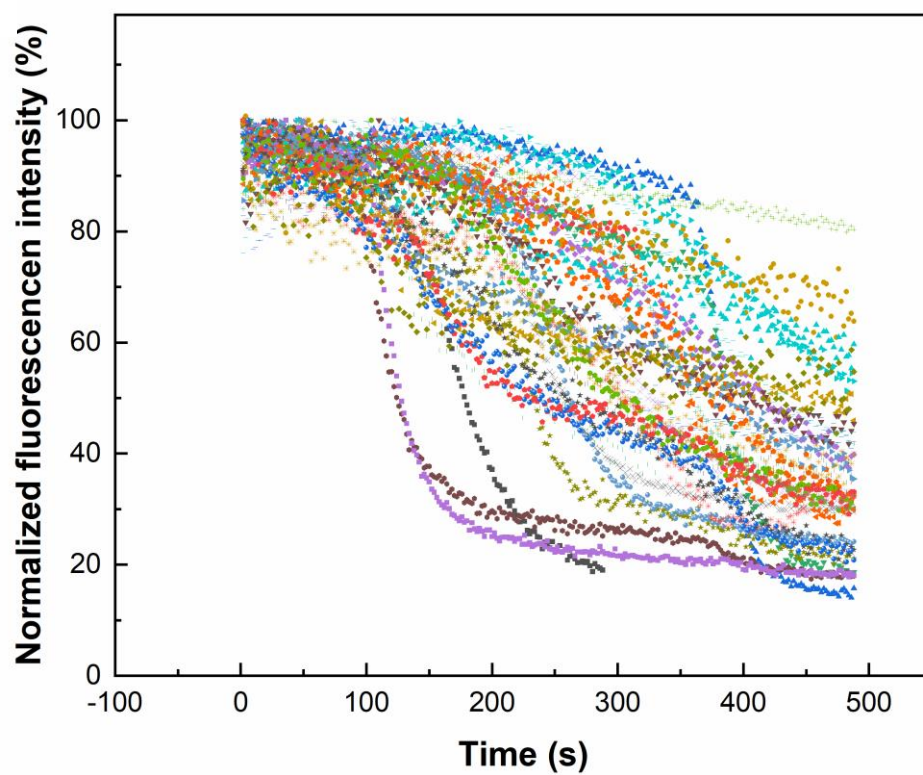
A)



B)



C)



D)

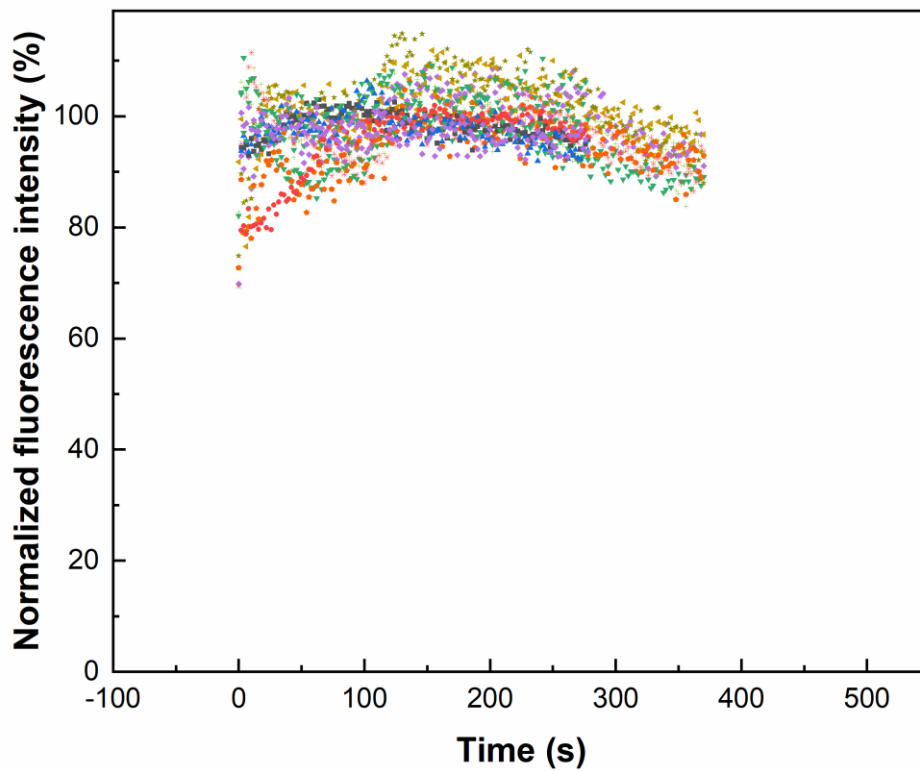


Figure 5.25 Time courses of normalized NADH fluorescent intensity traces monitored in GV containing NADH without (A, B) with TCNQ (C, D) before (A, C) and after (B, D) adding 10 mM ferricyanide.

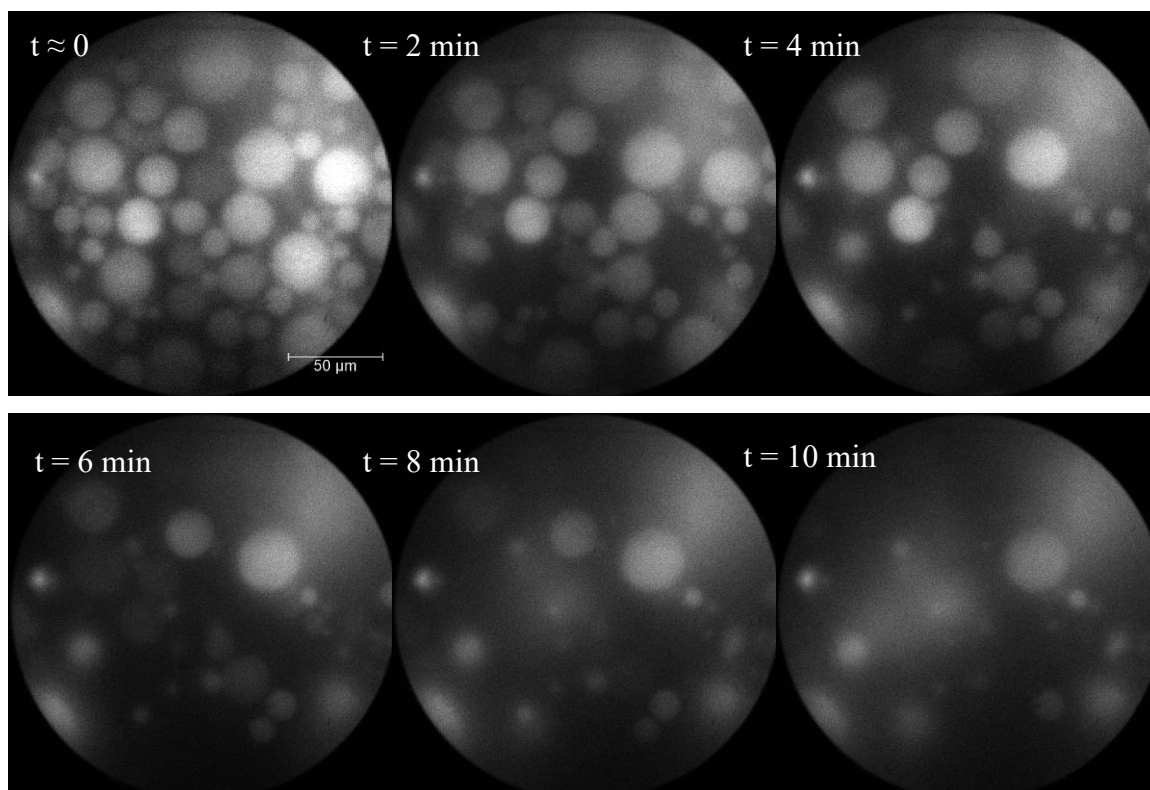
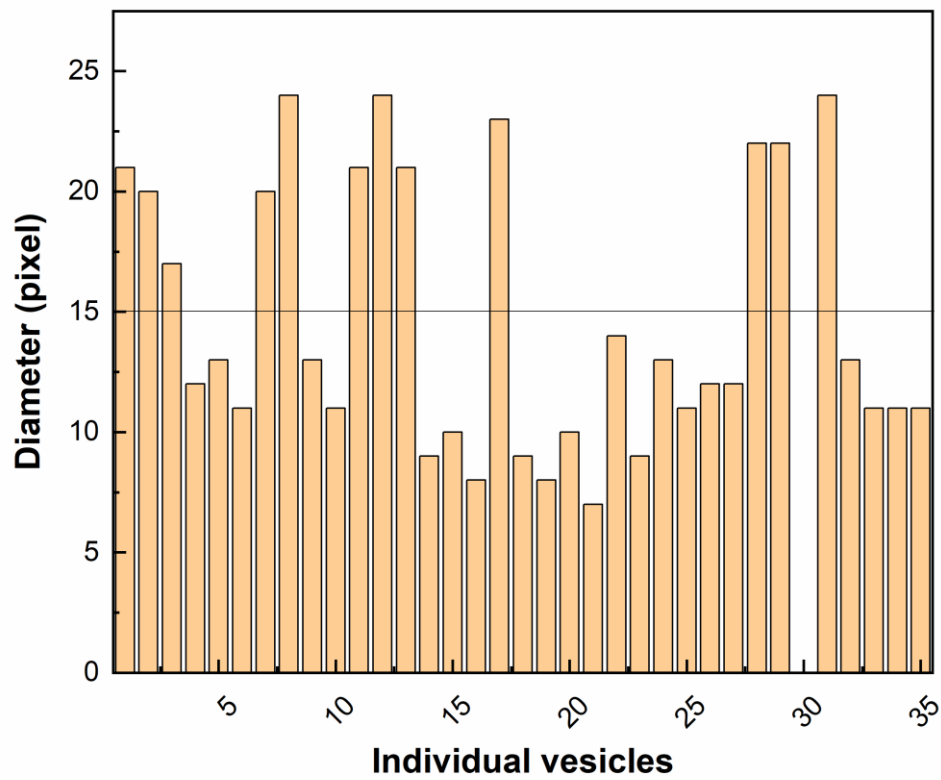


Figure 5.26 Time-lapse of GV microscope images after adding 10 mM ferricyanide (images of Figure 5.25 D).



B)

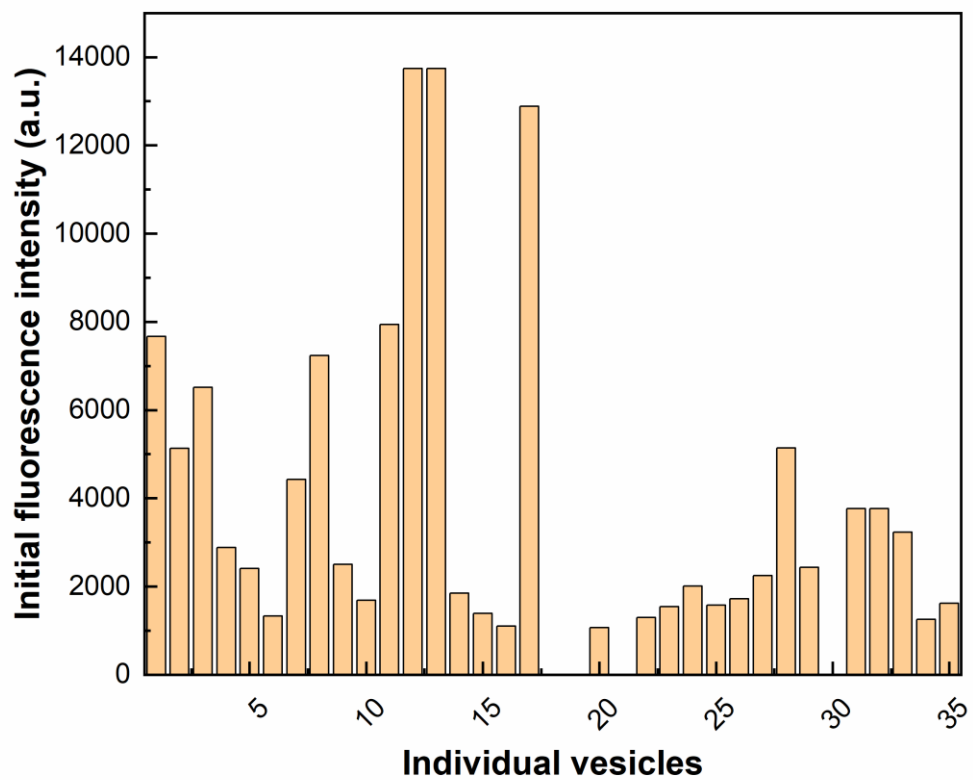
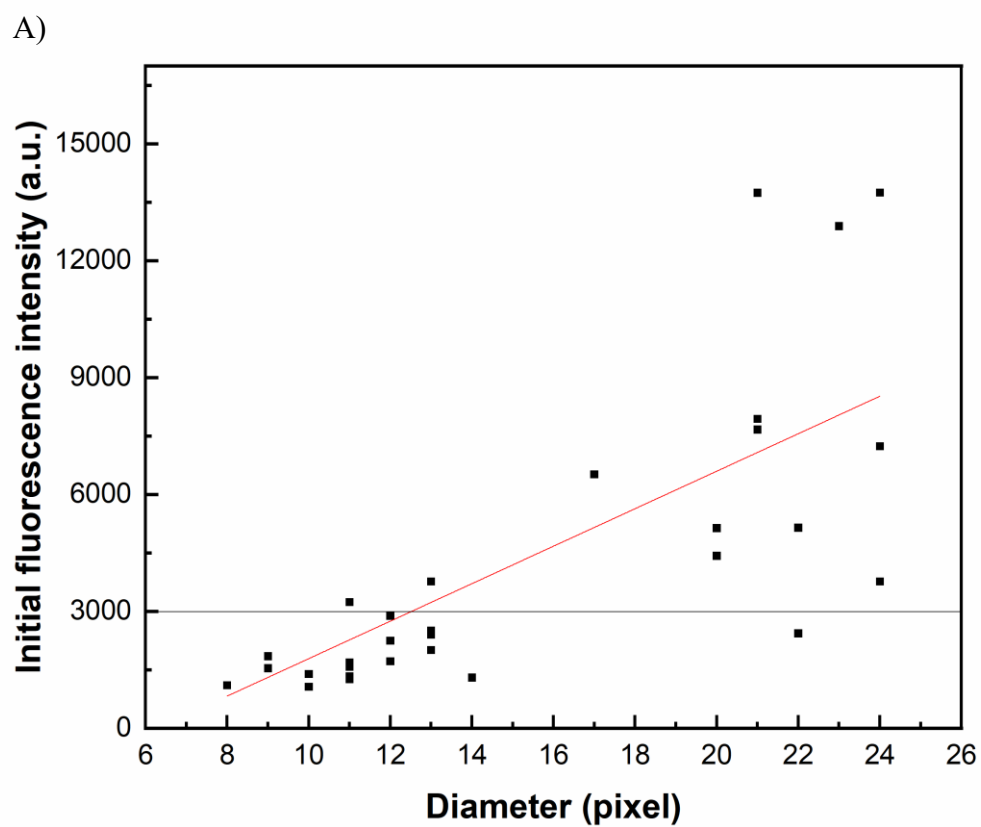


Figure 5.27 Diameters (A) and initial fluorescence intensity (B) of all GVs from the images presented in Figure 5.26.



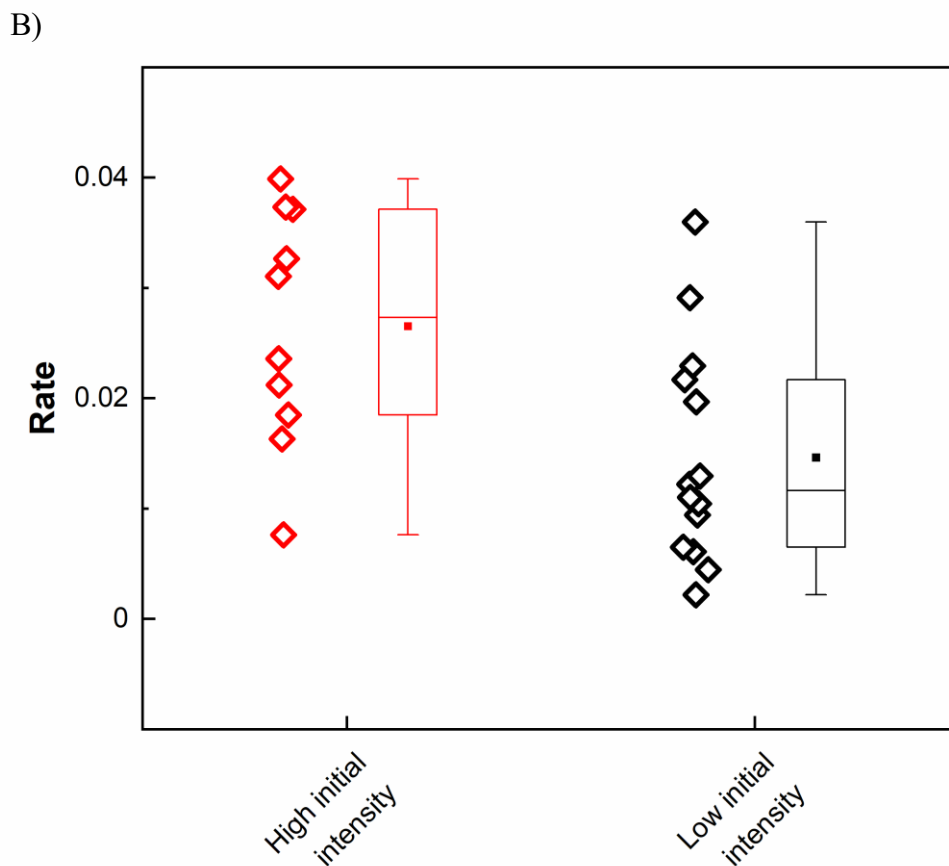


Figure 5.28 Initial fluorescence intensity relationship with diameters of GV (A) and their corresponding decay rate (B).

6 Rhodium based NADH regeneration module

In the natural cell, NAD^+ is reduced to its high energy form NADH in the process of oxidation of acetyl-CoA, known as the citric acid cycle, from the nutrients like carbohydrates, fats, and proteins. This process is a complex catalytic system involving many enzymes. Aiming to create a simple module for synthetic cells, similar to the NADH oxidation module discussed above, we sought non-enzymatic NADH regeneration catalysts and found organometallic complexes, which can be iridium¹⁸²⁻¹⁸³ or rhodium based¹⁸⁴ that could serve that purpose. In

particular, a pentamethylcyclopentadienyl rhodium bipyridine complex, $[\text{Cp}^*\text{Rh}(\text{bpy})\text{Cl}]\text{Cl}$ (RhC), which was synthesized by F. Hollmann and colleagues, has been shown to catalyze NAD regeneration, exhibiting stable activity in a broad range of pH and temperature conditions (Figure 6.1)^{73, 185}. Therefore, we attempted to engage RhC into POPC lipid vesicles to study transmembrane NAD^+ reduction.

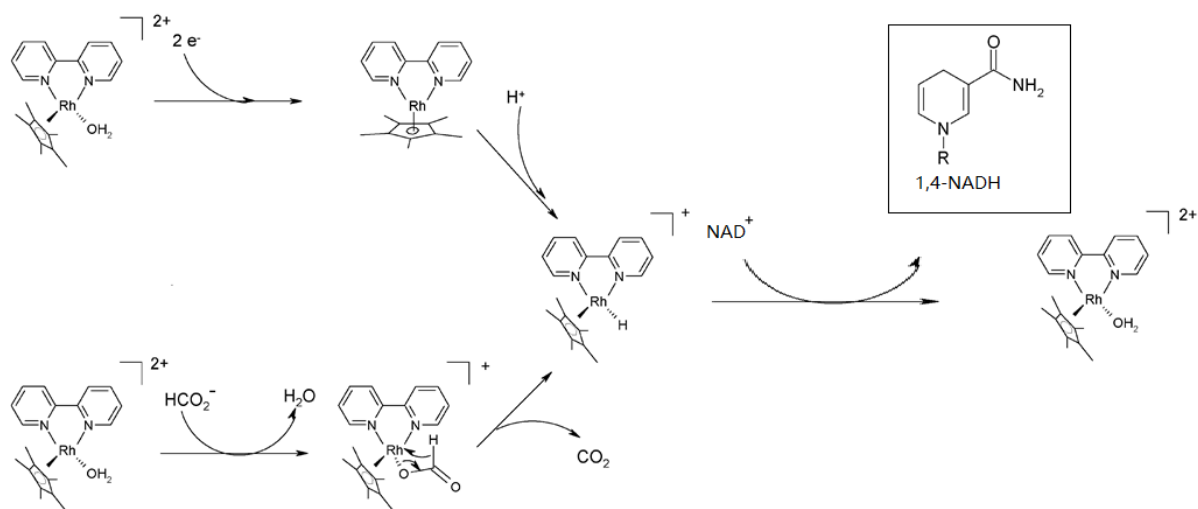


Figure 6.1 Non-enzyme regeneration of NADH by $[\text{Cp}^*\text{Rh}(\text{bpy})(\text{H}_2\text{O})]^{2+}$ synthesized by F. Hollmann⁷³.

6.1 Experimental details

6.1.1 NAD^+ reduction by rhodium complex

Firstly, in the same manner as NADH oxidation, NAD^+ reduction to NADH with rhodium complex was determined in buffer solution by monitoring the fluorescence intensity of NADH using a Cary Eclipse Fluorescence Spectrophotometer (Agilent Technologies, Santa Clara, USA). In detail, the reduction of NAD^+ in MOPS buffer (100 mM MOPS, 250 mM KCl,

Tris, pH 7.2) was monitored by the increase of the NADH fluorescence intensity after adding the electron donor sodium formate (HCOONa) and the rhodium complex.

6.1.2 NADH regeneration in rhodium-based LUVs

Along with the same strategy, used for NADH oxidation, the NADH regeneration module was developed with reconstitution of RhC in LUVs. POPC-based vesicles were prepared following the procedure described above. In total, 5 μmol POPC was used, and different concentrations of RhC dissolved in methanol were added, so that the molar ratios of POPC to RhC were 50:1, 25:1, and 12.5:1. For hydration, here instead of NADH solution, 500 μL of 2 mM NAD^+ in MOPS was used. Following the vortex, freeze-thaw cycles, and extrusion, different POPC-based LUVs were prepared. For non-encapsulated NAD^+ , the same column was used to remove free NAD^+ . Then, the sizes of different LUVs were determined by use of DLS.

At last, the NADH fluorescence intensity in different LUVs composed of different molar ratios of POPC to RhC was monitored over 12 h by adding 200 mM sodium formate as the electron donor to follow the reduction efficiency of NAD^+ by different amounts of RhC in LUVs.

6.2 Reduction of NAD^+ with the rhodium complex

NADH did not readily react with HCOONa in the absence of RhC even with a molar ratio of NAD^+ and HCOONa at 1:100, but when 10 mol% RhC to NAD^+ were added, the fluorescence intensity of NADH increased linearly (Figure 6.2). Additionally, without HCOONa as the reducing reagent, the direct addition of RhC to the NAD^+ solution did result in negligible reduction at the same molar ratio of RhC to NAD^+ 1:10.

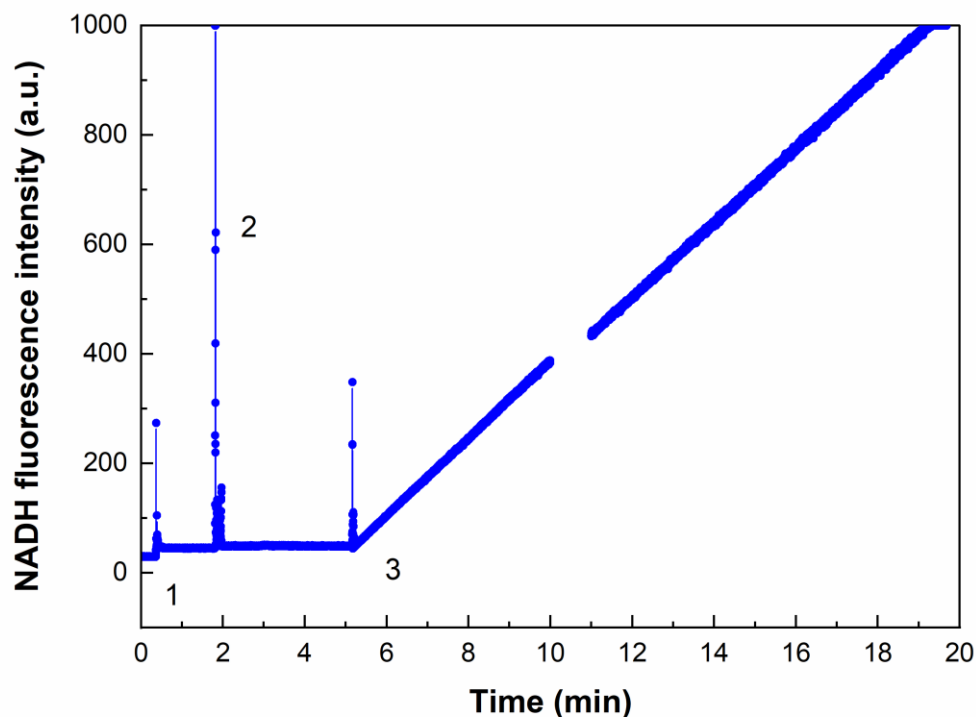


Figure 6.2 Fluorescence intensity of NADH in MOPS buffer monitored over time by stepwise adding different reagents: 1= 2 mM NAD^+ , 2= 200 mM HCOONa , and 3= 0.2 mM RhC.

6.3 NADH regeneration in rhodium based LUVs

The size distributions of different POPC-based vesicles comprising different ratios of POPC to RhC with and without encapsulated NAD^+ were obtained by DLS as illustrated in Figure 6.3. The mean diameters of all different vesicles were all around $\sim 180\text{--}200$ nm and the polydispersity indexes (PDI) were much lower than 0.2, indicating good quality of the results report. This indicated that also encapsulated NAD^+ did not affect the size of POPC-based LUVs.

After adding HCOONa to different RhC embedded LUVs, the fluorescence intensity of NADH profiles, as shown in Figure 6.4, was monitored, and the vesicle sizes were studied again by DLS to find out if the redox reaction affected them (dash lines in Figure 6.3). The

results from DLS suggested that after the reaction of HCOONa with different RhC-embedded LUVs, the relative intensity of the mean diameters was decreasing, and the distribution of diameters was wider. The z-average diameters were found to be slightly increased (e.g., from 187 nm to 192 nm for POPC: RhC = 25:1).

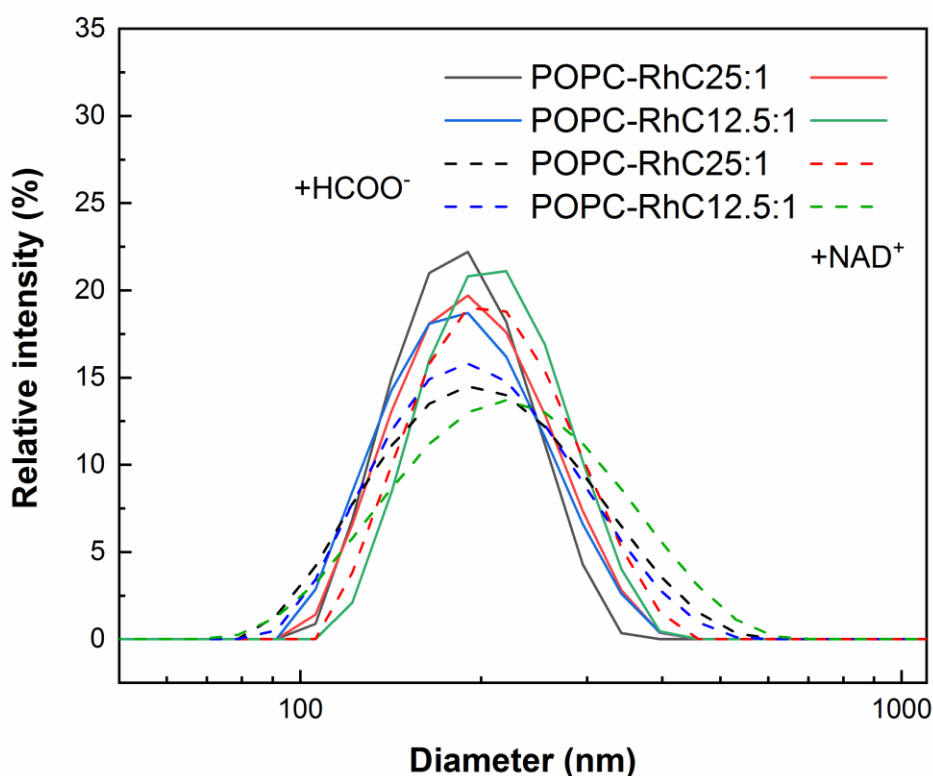


Figure 6.3 The size distribution of different POPC LUVs composed of different molar ratios of RhC (25:1, and 12.5:1) with and without encapsulation of NAD⁺ with (dash lines) and without (solid lines) adding exterior reducing agent HCOONa.

To address the effect of RhC on NADH regeneration in POPC-based LUVs, the NADH fluorescence intensity changes were compared with different amounts of RhC. As already demonstrated above, POPC-based LUVs accounted for background fluorescence intensity around 100 a.u., which corresponded to the present case. After adding HCOONa with 100-fold

molar concentration to NAD^+ entrapped in LUVs, NADH was readily produced in all RhC-embedded LUVs. The rate of NADH regeneration was proportional to the amount of RhC working as a mediator to catalyze the redox reaction. Considering that RhC is also soluble in water, it was removed during the column filtration used for removing non-encapsulated NAD^+ . As confirmed for POPC-based LUVs without RhC embedded (POPC: RhC 100:0), no NADH was generated over 12 h, which also indicated that no leakage of HCOONa through the LUV membrane took place.

These preliminary results indicate that the transmembrane arrangement can be applied both for the oxidation and the reduction of NAD cofactors.

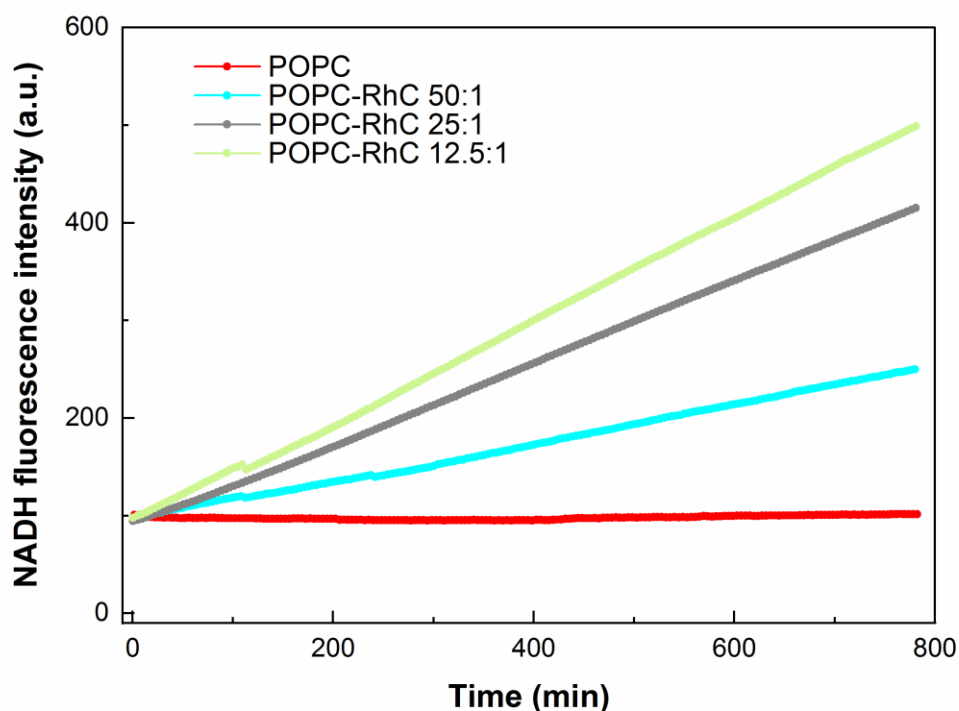


Figure 6.4 Fluorescence intensity profile of NADH in different POPC-based LUVs composed of different molar ratios of RhC (100:0, 50:1, 25:1, and 12.5:1) with encapsulation of NAD^+ after adding exterior reducing agent HCOONa .

7 Conclusions and outlook

In this thesis, we aimed to develop NAD regeneration strategies for use in artificial cells. To this end, we investigated the transmembrane oxidation of NADH and translated the same concept for NAD reduction. Thereby, we have demonstrated a highly simplified and feasible strategy for the transmembrane NAD regeneration by entrapping NAD inside the membrane and redox agents being placed outside the membrane with the aid of mediators embedded in the compartment membrane.

In this work, we investigated different types of membrane models.

Firstly, BLMs as well-known planar membrane models for studying ion conduction, offering access to both sides of the membrane were employed. Since NAD regeneration involved electrons and protons, we studied the NAD regeneration in BLMs with embedded conductive agents (DSSN) and associated catalysts (Methylene blue). The conductivity data and compatibility of DSSN in BLMs were shown to be promising. However, due to the limited stability of BLMs and the low efficiency of MB for the oxidation of NADH, we redirected our efforts toward vesicular systems.

Secondly, we developed an NAD⁺ regeneration module in vesicles via transmembrane oxidation of encapsulated NADH by an externally added electron acceptor and described the system behaviour through a simple dimensionless kinetic model. The primary motivation behind was the utilization as an NAD⁺ regeneration strategy for enzymatic oxidations, but the system also holds conceivable potential for use in living cells with respect to redox tuning of the NAD pool¹⁸⁶. Although rudimentary by nature, the theoretical description enabled us to trace all species concentrations and predict the spontaneous TCNQ reduction effects, which would remain hidden in the current experimental setup (lack of stop-flow apparatus, difficulties in online measurement of TCNQ redox state). We also substantiated the chemical aspect of “synthetic” in Synthetic Biology, opposed to the common interpretation in terms of man-made design in the top-down approach. A plain molecule like TCNQ allowed us to shortcut and mimic certain electron transport chain functionalities through a special form of interfacial redox catalysis, found in living cells. In this respect, the replacement of natural electron shuttles with synthetic counterparts provides the basis for novel architectures and opens new system

design possibilities in the stepwise assembly of minimal cells, with direct biotechnological implications.

The results clearly display the potential of the presented concept, but logically raise additional questions. From an experimental point of view, the next logical step is the encapsulation of a NAD-dependent dehydrogenase to demonstrate the utility of our approach for continuous cofactor regeneration. Experiments for more precise elucidation of the mechanism would be also beneficial. Regarding the better theoretical description of the system that we are striving for, it will be useful to expand the rate expressions with potential-dependent electron transfer parameters, according to Butler-Volmer kinetics or Marcus theory. In this way, we would be able to account for interfacial potential effects due to e.g. transport of protons. Another important aspect that must be considered is the influence of mass transport in an obviously heterogeneous system, wherein the interface plays a leading role. It is unclear to what extent the higher physicochemical precision would improve the predictability for our intended applications, but it would provide a solid theoretical framework for membrane-related electron transfer phenomena in biological systems.

Furthermore, we have studied the effect of different compositions of different compartments on the transmembrane NADH oxidation mediated by TCNQ. Taken together, the results suggested that hybrids consisting of POPC and the polymer PDMS-*g*-PEO with a molar ratio of 1:4 work more efficiently, both in the nanoscale and the micron scale, than other liposomes or hybrid vesicles which is potentially more applicable in powering synthetic cells. Further work needs to be done to combine this NAD⁺ regeneration module in hybrids with an ATP regeneration module to evaluate the efficiency for powering synthetic cells or with enzymatic reaction modules to produce potentially usable metabolites in synthetic cell-like bioreactors.

NAD⁺/NADH ratio is a hallmark for many cellular processes and the NADH signal is widely used as a readout for enzymatic assays based on its intrinsic fluorescence. Precise NADH analysis is required for the design of minimal systems in the context of bottom-up synthetic biology as well. The scaling up to micron-scaled vesicles also provided an unequivocal demonstration of the transmembrane electron transfer process in synthetic compartments at biologically relevant NADH concentrations, while analysis of the membrane

and kinetics required the use of confocal microscopy and time-correlated single-photon counting wide-field microscopy. The presented method accounts for sample heterogeneity and can be easily extrapolated to the investigation of passive or facilitated membrane transport. This simple approach will be particularly beneficial when using sensitive fluorophores, including readouts of spectroscopically modest substrates in coupled enzymatic assays while avoiding tedious preparation and sample manipulation procedures.

On the other hand, the NADH regeneration module based on the same strategy can be realized by embedding a rhodium complex (RhC) into the synthetic compartments even though the system would require further clarification. In future experiments, more precise control of these different modules using hydrodynamic trapping in microfluidic devices would broaden the development of functional modules for synthetic cells.

8 References

1. Benner, S. A.; Sismour, A. M., Synthetic Biology. *Nat Rev Genet* **2005**, *6* (7), 533-543.
2. Reardon, S., Visions of Synthetic Biology. *Science* **2011**, *333* (6047), 1242-1243.
3. Andrianantoandro, E.; Basu, S.; Karig, D. K.; Weiss, R., Synthetic biology: new engineering rules for an emerging discipline. *Mol Syst Biol* **2006**, *2* (1), 2006.0028.
4. Ball, P., Synthetic biology: Starting from scratch. *Nature* **2004**, *431* (7009), 624-626.
5. Check, E., Designs on life. *Nature* **2005**, *438* (7067), 417-418.
6. Purnick, P. E. M.; Weiss, R., The second wave of synthetic biology: from modules to systems. *Nat Rev Mol Cell Bio* **2009**, *10* (6), 410-422.
7. Hutchison, C. A.; Peterson, S. N.; Gill, S. R.; Cline, R. T.; White, O.; Fraser, C. M.; Smith, H. O.; Venter, J. C., Global transposon mutagenesis and a minimal *Mycoplasma* genome. *Science* **1999**, *286* (5447), 2165-2169.
8. Gibson, D. G.; Glass, J. I.; Lartigue, C.; Noskov, V. N.; Chuang, R. Y.; Algire, M. A.; Benders, G. A.; Montague, M. G.; Ma, L.; Moodie, M. M.; Merryman, C.; Vashee, S.; Krishnakumar, R.; Assad-Garcia, N.; Andrews-Pfannkoch, C.; Denisova, E. A.; Young, L.; Qi, Z. Q.; Segall-Shapiro, T. H.; Calvey, C. H.; Parmar, P. P.; Hutchison, C. A.; Smith, H. O.; Venter, J. C., Creation of a Bacterial Cell Controlled by a Chemically Synthesized Genome. *Science* **2010**, *329* (5987), 52-56.
9. Hutchison, C. A.; Chuang, R. Y.; Noskov, V. N.; Assad-Garcia, N.; Deerinck, T. J.; Ellisman, M. H.; Gill, J.; Kannan, K.; Karas, B. J.; Ma, L.; Pelletier, J. F.; Qi, Z. Q.; Richter, R. A.; Strychalski, E. A.; Sun, L. J.; Suzuki, Y.; Tsvetanova, B.; Wise, K. S.; Smith, H. O.; Glass, J. I.; Merryman, C.; Gibson, D. G.; Venter, J. C., Design and synthesis of a minimal bacterial genome. *Science* **2016**, *351* (6280).
10. Gibson, D. G.; Venter, J. C., Synthetic biology: Construction of a yeast chromosome. *Nature* **2014**, *509* (7499), 168-169.
11. Annaluru, N.; Muller, H.; Mitchell, L. A.; Ramalingam, S.; Stracquadiano, G.; Richardson, S. M.; Dymond, J. S.; Kuang, Z.; Scheifele, L. Z.; Cooper, E. M.; Cai, Y.; Zeller, K.; Agmon, N.; Han, J. S.; Hadjithomas, M.; Tullman, J.; Caravelli, K.; Cirelli, K.; Guo, Z.; London, V.; Yeluru, A.; Murugan, S.; Kandavelou, K.; Agier, N.; Fischer, G.; Yang, K.; Martin, J. A.; Bilgel, M.; Bohutski, P.; Boulter, K. M.; Capaldo, B. J.; Chang, J.; Charoen, K.; Choi, W. J.; Deng, P.; DiCarlo, J. E.; Doong, J.; Dunn, J.; Feinberg, J. I.; Fernandez, C.; Floria, C. E.; Gladowski, D.; Hadidi, P.; Ishizuka, I.; Jabbari, J.; Lau, C. Y.; Lee, P. A.; Li, S.; Lin, D.; Linder, M. E.; Ling, J.; Liu, J.; Liu, J.; London, M.; Ma, H.; Mao, J.; McDade, J. E.; McMillan, A.; Moore, A. M.; Oh, W. C.; Ouyang, Y.; Patel, R.; Paul, M.; Paulsen, L. C.; Qiu, J.; Rhee, A.; Rubashkin, M. G.; Soh, I. Y.; Sotuyo, N. E.; Srinivas, V.; Suarez, A.; Wong, A.; Wong, R.; Xie, W. R.; Xu, Y.; Yu, A. T.; Koszul, R.; Bader, J. S.; Boeke, J. D.; Chandrasegaran, S., Total synthesis of a functional designer eukaryotic chromosome. *Science* **2014**, *344* (6179), 55-58.
12. Shen, Y.; Wang, Y.; Chen, T.; Gao, F.; Gong, J.; Abramczyk, D.; Walker, R.; Zhao, H.; Chen, S.; Liu, W.; Luo, Y.; Muller, C. A.; Paul-Dubois-Taine, A.; Alver, B.; Stracquadiano, G.; Mitchell, L. A.; Luo, Z.; Fan, Y.; Zhou, B.; Wen, B.; Tan, F.; Wang, Y.; Zi, J.; Xie, Z.; Li, B.; Yang, K.; Richardson, S. M.; Jiang, H.; French, C. E.; Nieduszynski, C. A.; Koszul, R.; Marston, A. L.; Yuan, Y.; Wang, J.; Bader, J. S.; Dai, J.; Boeke, J. D.; Xu, X.; Cai, Y.; Yang, H., Deep functional analysis of synII, a 770-kilobase synthetic yeast chromosome. *Science* **2017**, *355* (6329).
13. Richardson, S. M.; Mitchell, L. A.; Stracquadiano, G.; Yang, K.; Dymond, J. S.; DiCarlo, J. E.; Lee, D.; Huang, C. L.; Chandrasegaran, S.; Cai, Y.; Boeke, J. D.; Bader, J. S., Design of a synthetic yeast genome. *Science* **2017**, *355* (6329), 1040-1044.
14. Teng, F.; Li, W.; Zhou, Q., Synthetic chromosome evolves the yeast genome. *Sci China Life Sci* **2019**, *62* (5), 708-709.
15. Breuer, M.; Earnest, T. M.; Merryman, C.; Wise, K. S.; Sun, L.; Lynott, M. R.; Hutchison, C. A.; Smith, H. O.; Lapek, J. D.; Gonzalez, D. J.; de Crecy-Lagard, V.; Haas, D.; Hanson, A. D.; Labhsetwar, P.; Glass, J. I.; Luthey-Schulten, Z., Essential metabolism for a minimal cell. *eLife* **2019**, *8*, e36842.
16. Venetz, J. E.; Del Medico, L.; Wolfle, A.; Schachle, P.; Bucher, Y.; Appert, D.; Tschan, F.; Flores-Tinoco, C. E.; van Kooten, M.; Guennoun, R.; Deutsch, S.; Christen, M.; Christen, B., Chemical synthesis rewriting of a bacterial genome to achieve design flexibility and biological functionality. *Proc Natl Acad Sci USA* **2019**, *116* (16), 8070-8079.
17. Schwillie, P., Bottom-Up Synthetic Biology: Engineering in a Tinkerer's World. *Science* **2011**, *333* (6047), 1252-1254.
18. Simpson, M. L., Cell-free synthetic biology: a bottom-up approach to discovery by design. *Mol Syst Biol* **2006**, *2* (1), 69.
19. Gopfrich, K.; Platzman, I.; Spatz, J. P., Mastering Complexity: Towards Bottom-up Construction of Multifunctional Eukaryotic Synthetic Cells. *Trends Biotechnol* **2018**, *36* (9), 938-951.
20. Rollie, S.; Mangold, M.; Sundmacher, K., Designing biological systems: Systems Engineering meets Synthetic Biology. *Chem Eng Sci* **2012**, *69* (1), 1-29.
21. Kim, D. M.; Swartz, J. R., Prolonging cell-free protein synthesis with a novel ATP regeneration system. *Biotechnol Bioeng* **1999**, *66* (3), 180-188.
22. Schwillie, P.; Diez, S., Synthetic biology of minimal systems. *Crit Rev Biochem Mol Biol* **2009**, *44* (4), 223-242.

23. Buddingh, B. C.; van Hest, J. C. M., Artificial Cells: Synthetic Compartments with Life-like Functionality and Adaptivity. *Acc Chem Res* **2017**, *50* (4), 769-777.
24. Schwillie, P.; Spatz, J.; Landfester, K.; Bodenschatz, E.; Herminghaus, S.; Sourjik, V.; Erb, T. J.; Bastiaens, P.; Lipowsky, R.; Hyman, A.; Dabrock, P.; Baret, J. C.; Vidakovic-Koch, T.; Bieling, P.; Dimova, R.; Mutschler, H.; Robinson, T.; Tang, T. Y. D.; Wegner, S.; Sundmacher, K., MaxSynBio: Avenues Towards Creating Cells from the Bottom Up. *Angew Chem Int Edit* **2018**, *57* (41), 13382-13392.
25. Wang, S. J.; Zhong, J. J., Bioreactor Engineering. *Bioprocessing for Value-Added Products from Renewable Resources: New Technologies and Applications* **2007**, 131-161.
26. Davy, A. M.; Kildegaard, H. F.; Andersen, M. R., Cell Factory Engineering. *Cell Syst* **2017**, *4* (3), 262-275.
27. Schmitt, C.; Lippert, A. H.; Bonakdar, N.; Sandoghdar, V.; Voll, L. M., Compartmentalization and Transport in Synthetic Vesicles. *Front Bioeng Biotechnol* **2016**, *4*, 19.
28. Chen, A. H.; Silver, P. A., Designing biological compartmentalization. *Trends Cell Biol* **2012**, *22* (12), 662-670.
29. Giessen, T. W.; Silver, P. A., Encapsulation as a Strategy for the Design of Biological Compartmentalization. *J Mol Biol* **2016**, *428* (5), 916-927.
30. Singer, S. J.; Nicolson, G. L., The Fluid Mosaic Model of the Structure of Cell Membranes. *Science* **1972**, *175* (4023), 720-731.
31. Mouritsen, O. G., Model Answers to Lipid Membrane Questions. *Csh Perspect Biol* **2011**, *3* (9), a004622.
32. Salehi-Reyhani, A.; Ces, O.; Elani, Y., Artificial cell mimics as simplified models for the study of cell biology. *Exp Biol Med* **2017**, *242* (13), 1309-1317.
33. Winterhalter, M., Black lipid membranes. *Curr Opin Colloid In* **2000**, *5* (3-4), 250-255.
34. Sackmann, E., Supported membranes: Scientific and practical applications. *Science* **1996**, *271* (5245), 43-48.
35. Chan, Y. H. M.; Boxer, S. G., Model membrane systems and their applications. *Curr Opin Chem Biol* **2007**, *11* (6), 581-587.
36. Schulz, M.; Binder, W. H., Mixed Hybrid Lipid/Polymer Vesicles as a Novel Membrane Platform. *Macromolecular rapid communications* **2015**, *36* (23), 2031-2041.
37. Nicolson, G. L., Update of the 1972 Singer-Nicolson Fluid-Mosaic Model of Membrane Structure. *Discoveries (Craiova)* **2013**, *1* (1), e3.
38. Otrin, L.; Marusic, N.; Bednarz, C.; Vidakovic-Koch, T.; Lieberwirt, I.; Landfester, K.; Sundmacher, K., Toward Artificial Mitochondrion: Mimicking Oxidative Phosphorylation in Polymer and Hybrid Membranes. *Nano Lett* **2017**, *17* (11), 6816-6821.
39. Ji, X. Y.; Wang, J.; Mei, L.; Tao, W.; Barrett, A.; Su, Z. G.; Wang, S. M.; Ma, G. H.; Shi, J. J.; Zhang, S. P., Porphyrin/SiO₂/Cp*Rh(bpy)Cl Hybrid Nanoparticles Mimicking Chloroplast with Enhanced Electronic Energy Transfer for Biocatalyzed Artificial Photosynthesis. *Adv Funct Mater* **2018**, *28* (9), 1705083.
40. Kim, J. H.; Nam, D. H.; Park, C. B., Nanobiocatalytic assemblies for artificial photosynthesis. *Curr Opin Biotech* **2014**, *28*, 1-9.
41. Otrin, L.; Kleineberg, C.; da Silva, L. C.; Landfester, K.; Ivanov, I.; Wang, M. H.; Bednarz, C.; Sundmacher, K.; Vidakovic-Koch, T., Artificial Organelles for Energy Regeneration. *Adv Biosyst* **2019**, *3* (6), 1800323.
42. Schwander, T.; von Borzyskowski, L. S.; Burgener, S.; Cortina, N. S.; Erb, T. J., A synthetic pathway for the fixation of carbon dioxide in vitro. *Science* **2016**, *354* (6314), 900-904.
43. Miller, T. E.; Beneyton, T.; Schwander, T.; Diehl, C.; Girault, M.; McLean, R.; Chotel, T.; Claus, P.; Cortina, N. S.; Baret, J. C.; Erb, T. J., Light-powered CO₂ fixation in a chloroplast mimic with natural and synthetic parts. *Science* **2020**, *368* (6491), 649-654.
44. Erb, T. J.; Jones, P. R.; Bar-Even, A., Synthetic metabolism: metabolic engineering meets enzyme design. *Curr Opin Chem Biol* **2017**, *37*, 56-62.
45. Houtkooper, R. H.; Canto, C.; Wanders, R. J.; Auwerx, J., The secret life of NAD⁺: an old metabolite controlling new metabolic signaling pathways. *Endocr Rev* **2010**, *31* (2), 194-223.
46. Lin, S. J.; Guarente, L., Nicotinamide adenine dinucleotide, a metabolic regulator of transcription, longevity and disease. *Current Opinion in Cell Biology* **2003**, *15* (2), 241-246.
47. Belenky, P.; Bogan, K. L.; Brenner, C., NAD⁺ metabolism in health and disease. *Trends Biochem Sci* **2007**, *32* (1), 12-19.
48. Canto, C.; Menzies, K. J.; Auwerx, J., NAD(+) Metabolism and the Control of Energy Homeostasis: A Balancing Act between Mitochondria and the Nucleus. *Cell Metab* **2015**, *22* (1), 31-53.
49. Wang, S.; Xing, Z.; Vosler, P. S.; Yin, H.; Li, W.; Zhang, F.; Signore, A. P.; Stetler, R. A.; Gao, Y.; Chen, J., Cellular NAD replenishment confers marked neuroprotection against ischemic cell death: role of enhanced DNA repair. *Stroke* **2008**, *39* (9), 2587-2595.
50. Wiley, C.; Campisi, J., NAD⁺ controls neural stem cell fate in the aging brain. *EMBO J* **2014**, *33* (12), 1289-1291.
51. Oka, S.; Hsu, C. P.; Sadoshima, J., Regulation of cell survival and death by pyridine nucleotides. *Circ Res* **2012**, *111* (5), 611-627.

52. Mouchiroud, L.; Houtkooper, R. H.; Moullan, N.; Katsyuba, E.; Ryu, D.; Canto, C.; Mottis, A.; Jo, Y. S.; Viswanathan, M.; Schoonjans, K.; Guarente, L.; Auwerx, J., The NAD⁺/Sirtuin Pathway Modulates Longevity through Activation of Mitochondrial UPR and FOXO Signaling. *Cell* **2013**, *154* (2), 430-441.
53. Chiarugi, A.; Dolle, C.; Felici, R.; Ziegler, M., The NAD metabolome—a key determinant of cancer cell biology. *Nat Rev Cancer* **2012**, *12* (11), 741-752.
54. van der Donk, W. A.; Zhao, H. M., Recent developments in pyridine nucleotide regeneration. *Curr Opin Biotech* **2003**, *14* (4), 421-426.
55. Wu, H.; Tian, C.; Song, X.; Liu, C.; Yang, D.; Jiang, Z., Methods for the regeneration of nicotinamide coenzymes. *Green Chemistry* **2013**, *15* (7), 1773-1789.
56. Maid, H.; Bohm, P.; Huber, S. M.; Bauer, W.; Hummel, W.; Jux, N.; Groger, H., Iron catalysis for in situ regeneration of oxidized cofactors by activation and reduction of molecular oxygen: a synthetic metalloporphyrin as a biomimetic NAD(P)H oxidase. *Angew Chem Int Ed Engl* **2011**, *50* (10), 2397-2400.
57. Canivet, J.; Suss-Fink, G.; Stepnicka, P., Water-soluble phenanthroline complexes of rhodium, iridium and ruthenium for the regeneration of NADH in the enzymatic reduction of ketones. *Eur J Inorg Chem* **2007**, (30), 4736-4742.
58. Kim, J. H.; Lee, M.; Lee, J. S.; Park, C. B., Self-Assembled Light-Harvesting Peptide Nanotubes for Mimicking Natural Photosynthesis. *Angew Chem Int Edit* **2012**, *51* (2), 517-520.
59. Summers, D. P.; Rodoni, D., Vesicle Encapsulation of a Nonbiological Photochemical System Capable of Reducing NAD(+) to NADH. *Langmuir* **2015**, *31* (39), 10633-10637.
60. Ma, B. C.; da Silva, L. C.; Jo, S. M.; Wurm, F. R.; Bannwarth, M. B.; Zhang, K. A. I.; Sundmacher, K.; Landfester, K., Polymer-Based Module for NAD(+) Regeneration with Visible Light. *ChemBiochem* **2019**, *20* (20), 2593-2596.
61. Shaked, Z.; Whitesides, G. M., Enzyme-Catalyzed Organic-Synthesis - NADH Regeneration by Using Formate Dehydrogenase. *Journal of the American Chemical Society* **1980**, *102* (23), 7104-7105.
62. Arrhenius, T. S.; Blancharddesce, M.; Dvolaitzky, M.; Lehn, J. M.; Malthete, J., Molecular Devices - Caroviologens as an Approach to Molecular Wires Synthesis and Incorporation into Vesicle Membranes. *P Natl Acad Sci USA* **1986**, *83* (15), 5355-5359.
63. Campos, R.; Katakay, R., Electron transport in supported and tethered lipid bilayers modified with bioelectroactive molecules. *The Journal of Physical Chemistry. B* **2012**, *116* (13), 3909-3917.
64. Murthy, A. S. N.; Gupta, A. R. L., NADH Sensor with Electrochemically Modified TCNQ Electrode. *Anal Chim Acta* **1994**, *289* (1), 43-46.
65. Schlereth, D. D.; Katz, E.; Schmidt, H. L., Surface-Modified Gold Electrodes for Electrocatalytic Oxidation of NADH Based on the Immobilization of Phenoxazine and Phenothiazine-Derivatives on Self-Assembled Monolayers. *Electroanal* **1995**, *7* (1), 46-54.
66. Kubota, L. T.; Gorton, L., Electrochemical study of flavins, phenazines, phenoxazines and phenothiazines immobilized on zirconium phosphate. *Electroanal* **1999**, *11* (10-11), 719-728.
67. Low, P. J.; Marques-Gonzalez, S., Molecular Wires: An Overview of the Building Blocks of Molecular Electronics. *Single-Molecule Electronics: An Introduction to Synthesis, Measurement and Theory* **2016**, 87-116.
68. Garner, L. E.; Park, J.; Dyar, S. M.; Chworos, A.; Sumner, J. J.; Bazan, G. C., Modification of the Optoelectronic Properties of Membranes via Insertion of Amphiphilic Phenylenevinylene Oligoelectrolytes. *Journal of the American Chemical Society* **2010**, *132* (29), 10042-10052.
69. Du, J.; Thomas, A. W.; Chen, X. F.; Garner, L. E.; Vandenberg, C. A.; Bazan, G. C., Increased ion conductance across mammalian membranes modified with conjugated oligoelectrolytes. *Chem Commun* **2013**, *49* (83), 9624-9626.
70. Krysiński, P., Redox Reactions on TCNQ-modified Self-assembled Monomolecular Films. *Adv. Mater. Opt. Electron.* **1998**, *8* (3), 121-128.
71. Garcia-Pineda, I.; Mayen, M.; Rodriguez-Mellado, J. M.; Rodriguez-Amaro, R., NADH Electrocatalytic Oxidation on Gold Nanoparticle-Modified PVC/TTF-TCNQ Composite Electrode. Application as Amperometric Sensor. *Electroanal* **2013**, *25* (8), 1981-1987.
72. Sevcik, P.; Dunford, H. B., Kinetics of the Oxidation of NADH by Methylene-Blue in a Closed System. *Journal of Physical Chemistry* **1991**, *95* (6), 2411-2415.
73. Hollmann, F.; Witholt, B.; Schmid, A., [Cp*Rh(bpy)(H₂O)](2+): a versatile tool for efficient and non-enzymatic regeneration of nicotinamide and flavin coenzymes. *J Mol Catal B-Enzym* **2002**, *19*, 167-176.
74. Mueller, P.; Rudin, D. O.; Tien, H. T.; Wescott, W. C., Reconstitution of Cell Membrane Structure in Vitro and Its Transformation into an Excitable System. *Nature* **1962**, *194* (4832), 979-980.
75. Mueller, P.; Rudin, D. O., Action Potential Phenomena in Experimental Bimolecular Lipid Membranes. *Nature* **1967**, *213* (5076), 603-604.
76. Vargas, J.; Alarcon, J. M.; Rojas, E., Displacement currents associated with the insertion of Alzheimer disease amyloid beta-peptide into planar bilayer membranes. *Biophys J* **2000**, *79* (2), 934-944.
77. Tsemperouli, M.; Amstad, E.; Sakai, N.; Matile, S.; Sugihara, K., Black Lipid Membranes: Challenges in Simultaneous Quantitative Characterization by Electrophysiology and Fluorescence Microscopy. *Langmuir* **2019**, *35* (26), 8748-8757.

78. van Meer, G.; Voelker, D. R.; Feigenson, G. W., Membrane lipids: where they are and how they behave. *Nat Rev Mol Cell Bio* **2008**, *9* (2), 112-124.
79. Salim, M.; Minamikawa, H.; Sugimura, A.; Hashim, R., Amphiphilic designer nano-carriers for controlled release: from drug delivery to diagnostics. *MedChemComm* **2014**, *5* (11), 1602-1618.
80. Carrion, F. J.; Delamaza, A.; Parra, J. L., The Influence of Ionic-Strength and Lipid Bilayer Charge on the Stability of Liposomes. *J Colloid Interf Sci* **1994**, *164* (1), 78-87.
81. Maurer, S. E.; Sorensen, K. T.; Iqbal, Z.; Nicholas, J.; Quirion, K.; Gioia, M.; Monnard, P. A.; Hanczyc, M. M., Vesicle Self-Assembly of Monoalkyl Amphiphiles under the Effects of High Ionic Strength, Extreme pH, and High Temperature Environments. *Langmuir* **2018**, *34* (50), 15560-15568.
82. Makino, K.; Yamada, T.; Kimura, M.; Oka, T.; Ohshima, H.; Kondo, T., Temperature-Induced and Ionic Strength-Induced Conformational-Changes in the Lipid Head Group Region of Liposomes as Suggested by Zeta-Potential Data. *Biophys Chem* **1991**, *41* (2), 175-183.
83. Kulkarni, C. V., Lipid crystallization: from self-assembly to hierarchical and biological ordering. *Nanoscale* **2012**, *4* (19), 5779-5791.
84. Ghysels, A.; Kramer, A.; Venable, R. M.; Teague, W. E.; Lyman, E.; Gawrisch, K.; Pastor, R. W., Permeability of membranes in the liquid ordered and liquid disordered phases. *Nat Commun* **2019**, *10* (1), 1-12.
85. Dieudonne, D. J.; Gurnev, P. A.; Rogozea, A. L.; Ray, B. D.; Petrache, H. I., Physical Properties of the Lipid Diphytanoyl Phosphatidylcholine (DPhPc) used for Ion Channel Measurements. *Biophys J* **2010**, *98* (3), 667a-668a.
86. Andersson, M.; Jackman, J.; Wilson, D.; Jarvoll, P.; Alfredsson, V.; Okeyo, G.; Duran, R., Vesicle and bilayer formation of diphytanoylphosphatidylcholine (DPhPC) and diphytanoylphosphatidylethanolamine (DPhPE) mixtures and their bilayers' electrical stability. *Colloid Surface B* **2011**, *82* (2), 550-561.
87. Thomas, A. W.; Garner, L. E.; Nevin, K. P.; Woodard, T. L.; Franks, A. E.; Lovley, D. R.; Sumner, J. J.; Sund, C. J.; Bazan, G. C., A lipid membrane intercalating conjugated oligoelectrolyte enables electrode driven succinate production in *Shewanella*. *Energy & Environmental Science* **2013**, *6* (6), 1761-1765.
88. Garner, L. E.; Thomas, A. W.; Sumner, J. J.; Harvey, S. P.; Bazan, G. C., Conjugated oligoelectrolytes increase current response and organic contaminant removal in wastewater microbial fuel cells. *Energy & Environmental Science* **2012**, *5* (11), 9449-9452.
89. Schafer, F. Q.; Buettner, G. R., Redox Environment of the Cell as Viewed through the Redox State of the Glutathione Disulfide/Glutathione Couple. *Free Radical Biol. Med.* **2001**, *30*, 1191-1212.
90. Karyakin, A. A.; Strakhova, A. K.; Karyakina, E. E.; Varfolomeyev, S. D.; Yatsimirsky, A. K., The Electrochemical Polymerization of Methylene-Blue and Bioelectrochemical Activity of the Resulting Film. *Bioelectrochemistry and Bioenergetics* **1993**, *32* (1), 35-43.
91. Hou, H.; Chen, X.; Thomas, A. W.; Catania, C.; Kirchhofer, N. D.; Garner, L. E.; Han, A.; Bazan, G. C., Conjugated oligoelectrolytes increase power generation in *E. coli* microbial fuel cells. *Advanced materials* **2013**, *25* (11), 1593-1597.
92. Hinks, J.; Wang, Y. F.; Poh, W. H.; Donose, B. C.; Thomas, A. W.; Wuertz, S.; Loo, S. C. J.; Bazan, G. C.; Kjelleberg, S.; Mu, Y. G.; Seviour, T., Modeling Cell Membrane Perturbation by Molecules Designed for Transmembrane Electron Transfer. *Langmuir* **2014**, *30* (9), 2429-2440.
93. Catania, C.; Ajo-Franklin, C. M.; Bazan, G. C., Membrane permeabilization by conjugated oligoelectrolytes accelerates whole-cell catalysis. *RSC Advances* **2016**, *6* (102), 100300-100306.
94. Gwozdzińska, P.; Pawłowska, R.; Milczarek, J.; Garner, L. E.; Thomas, A. W.; Bazan, G. C.; Chworos, A., Phenylenevinylene conjugated oligoelectrolytes as fluorescent dyes for mammalian cell imaging. *Chem Commun (Camb)* **2014**, *50* (94), 14859-14861.
95. Elani, Y.; Law, R. V.; Ces, O., Vesicle-based artificial cells as chemical microreactors with spatially segregated reaction pathways. *Nat Commun* **2014**, *5*, 1-5.
96. Kuchler, A.; Yoshimoto, M.; Luginbuhl, S.; Mavelli, F.; Walde, P., Enzymatic reactions in confined environments. *Nat Nanotechnol* **2016**, *11* (5), 409-420.
97. Gomez-Hens, A.; Fernandez-Romero, J. M., The role of liposomes in analytical processes. *Trac-Trend Anal Chem* **2005**, *24* (1), 9-19.
98. Hope, M. J.; Bally, M. B.; Webb, G.; Cullis, P. R., Production of Large Unilamellar Vesicles by a Rapid Extrusion Procedure - Characterization of Size Distribution, Trapped Volume and Ability to Maintain a Membrane-Potential. *Biochimica Et Biophysica Acta* **1985**, *812* (1), 55-65.
99. Patil, Y. P.; Jadhav, S., Novel methods for liposome preparation. *Chem Phys Lipids* **2014**, *177*, 8-18.
100. Angelova, M. I.; Dimitrov, D. S., Liposome Electroformation. *Faraday Discuss* **1986**, *81*, 303-311.
101. Rodriguez, N.; Pincet, F.; Cribier, S., Giant vesicles formed by gentle hydration and electroformation: A comparison by fluorescence microscopy. *Colloid Surface B* **2005**, *42* (2), 125-130.
102. Rideau, E.; Dimova, R.; Schwille, P.; Wurm, F. R.; Landfester, K., Liposomes and polymersomes: a comparative review towards cell mimicking. *Chem Soc Rev* **2018**, *47* (23), 8572-8610.

103. Maherani, B.; Arab-Tehrany, E.; Kheiriloom, A.; Geny, D.; Linder, M., Calcein release behavior from liposomal bilayer; influence of physicochemical/mechanical/structural properties of lipids. *Biochimie* **2013**, *95* (11), 2018-2033.
104. Discher, B. M.; Won, Y. Y.; Ege, D. S.; Lee, J. C. M.; Bates, F. S.; Discher, D. E.; Hammer, D. A., Polymersomes: Tough vesicles made from diblock copolymers. *Science* **1999**, *284* (5417), 1143-1146.
105. Le Meins, J. F.; Schatz, C.; Lecommandoux, S.; Sandre, O., Hybrid polymer/lipid vesicles: state of the art and future perspectives. *Mater Today* **2013**, *16* (10), 397-402.
106. Antonietti, M.; Forster, S., Vesicles and liposomes: A self-assembly principle beyond lipids. *Advanced Materials* **2003**, *15* (16), 1323-1333.
107. Lin, Z.; Hill, R. M.; Davis, H. T.; Scriven, L. E.; Talmon, Y., Cryo-Transmission Electron-Microscopy Study of Vesicles and Micelles in Siloxane Surfactant Aqueous-Solutions. *Langmuir* **1994**, *10* (4), 1008-1011.
108. Marusic, N.; Otrin, L.; Zhao, Z. L.; Lira, R. B.; Kyrilic, F. L.; Hamdi, F.; Kastritic, P. L.; Vidakovic-Koch, T.; Ivanov, I.; Sundmacher, K.; Dimova, R., Constructing artificial respiratory chain in polymer compartments: Insights into the interplay between bo(3) oxidase and the membrane. *Proc Natl Acad Sci USA* **2020**, *117* (26), 15006-15017.
109. Itel, F.; Najer, A.; Palivan, C. G.; Meier, W., Dynamics of Membrane Proteins within Synthetic Polymer Membranes with Large Hydrophobic Mismatch. *Nano Lett* **2015**, *15* (6), 3871-3878.
110. Tribet, C.; Vial, F., Flexible macromolecules attached to lipid bilayers: impact on fluidity, curvature, permeability and stability of the membranes. *Soft Matter* **2008**, *4* (1), 68-81.
111. Robinson, J. N.; Colehamilton, D. J., Electron-Transfer across Vesicle Bilayers. *Chem Soc Rev* **1991**, *20* (1), 49-94.
112. Cheng, Y. F.; Cunnane, V. J.; Kontturi, A. K.; Kontturi, K.; Schiffrin, D. J., Potential dependence of transmembrane electron transfer across phospholipid bilayers mediated by ubiquinone 10. *Journal of Physical Chemistry* **1996**, *100* (38), 15470-15477.
113. Ma, W.; Li, D.-W.; Sutherland, T. C.; Li, Y.; Long, Y.-T.; Chen, H.-Y., Reversible Redox of NADH and NAD(+) at a Hybrid Lipid Bilayer Membrane Using Ubiquinone. *Journal of the American Chemical Society* **2011**, *133* (32), 12366-12369.
114. Ma, W.; Ying, Y. L.; Qin, L. X.; Gu, Z.; Zhou, H.; Li, D. W.; Sutherland, T. C.; Chen, H. Y.; Long, Y. T., Investigating electron-transfer processes using a biomimetic hybrid bilayer membrane system. *Nature Protocols* **2013**, *8* (3), 439-450.
115. Seto-Young, D.; S.Perlin, D., Effect of Membrane Voltage on the Plasma Membrane H⁺-ATPase of *Saccharomyces cerevisiae*. *J Biol Chem* **1991**, *266* (25), 1383-1389.
116. Shiba, H.; Maeda, K.; Ichieda, N.; Kasuno, M.; Yoshida, Y.; Shirai, O.; Kihara, S., Voltammetric study on the electron transport through a bilayer lipid membrane containing neutral or ionic redox molecules. *J Electroanal Chem* **2003**, *556*, 1-11.
117. Asaka, K.; Ottova, A.; Tien, H. T., Mediated Electron Transfer across Supported Bilayer Lipid Membrane (s-BLM). *Thin Solid Films* **1999**, *354*, 201-207.
118. Wang, M. H.; Woelfer, C.; Otrin, L.; Ivanov, I.; Vidakovic-Koch, T.; Sundmacher, K., Transmembrane NADH Oxidation with Tetracyanoquinodimethane. *Langmuir* **2018**, *34* (19), 5435-5443.
119. Tamaya, H.; Nakano, H.; Iimori, T., 7,7,8,8-Tetracyanoquinodimethane (TCNQ) emits visible photoluminescence in solution. *J Lumin* **2017**, *192*, 203-207.
120. Chen, R. F.; Knutson, J. R., Mechanism of Fluorescence Concentration Quenching of Carboxyfluorescein in Liposomes - Energy-Transfer to Nonfluorescent Dimers. *Analytical Biochemistry* **1988**, *172* (1), 61-77.
121. Daeneke, T.; Uemura, Y.; Duffy, N. W.; Mozer, A. J.; Koumura, N.; Bach, U.; Spiccia, L., Aqueous dye-sensitized solar cell electrolytes based on the ferricyanide-ferrocyanide redox couple. *Adv Mater* **2012**, *24* (9), 1222-1225.
122. Boschloo, G.; Hagfeldt, A., Characteristics of the iodide/triiodide redox mediator in dye-sensitized solar cells. *Acc Chem Res* **2009**, *42* (11), 1819-1826.
123. Rao, S.P.; Singh, S.R.; Bandakavi, S.R., Formal redox potentials of ferricyanide ferrocyanide couple in certain non-aqueous water mixtures. *Proc Natl Acad Sci India Sect Phys Sci* **1978**, *44*, 333-335.
124. Rock, P.A., The Standard Oxidation Potential of the Ferrocyanide-Ferricyanide Electrode at 25° and the Entropy of Ferrocyanide Ion. *The Journal of Physical Chemistry* **1966**, *70* (2), 576-580.
125. Wang, J.; Yang, C.; Chen, X.; Bao, B.; Zhang, X.; Li, D.; Du, X.; Shi, R.; Yang, J.; Zhu, R., A high effective NADH-ferrocyanide dehydrogenase coupled with laccase for NAD(+) regeneration. *Biotechnol Lett* **2016**, *38* (8), 1315-1320.
126. Kulikova, V. S., NADH oxidase activity of gold nanoparticles in aqueous solution. *Kinet Catal* **2005**, *46* (3), 373-375.
127. Hinkle, P., A Model System for Mitochondrial Ion Transport and Respiratory Control. *Biochem. Biophys. Res. Commun.* **1970**, *41*, 1375-1381.
128. Matsumoto, R.; Kakuta, M.; Sugiyama, T.; Goto, Y.; Sakai, H.; Tokita, Y.; Hatazawa, T.; Tsujimura, S.; Shirai, O.; Kano, K., A liposome-based Energy Conversion System for Accelerating the Multi-enzyme Reactions. *Phys. Chem. Chem. Phys.* **2010**, *12*, 13904-13906.
129. Fujita, S.; Matsumoto, R.; Ogawa, K.; Sakai, H.; Maesaka, A.; Tokita, Y.; Tsujimura, S.; Shirai, O.; Kano, K., Bioelectrocatalytic oxidation of glucose with antibiotic channel-containing liposomes. *Phys. Chem. Chem. Phys.* **2013**, *15*, 2650-2653.

130. Daskalakis, N. N.; Muller, A.; Evans, S. D.; Jeuken, L. J. C., Driving Bioenergetic Processes with Electrodes. *Soft Matter* **2011**, *7*, 49-52.
131. Herzog, A.; Uchiya, K.; Karthaus, O., Pollen-like Particles can be Prepared by Exposure of Polymer Microparticles to an Electron Beam. *Matters (Zürich)* **2016**, *2* (3), 1-5.
132. Hernandez, V. A.; Eriksson, E. K.; Edwards, K., Ubiquinone-10 alters mechanical properties and increases stability of phospholipid membranes. *Bba-Biomembranes* **2015**, *1848* (10), 2233-2243.
133. Rover Junior, L.; Fernandes, J. C.; de Oliveira Neto, G.; Kubota, L. T.; Katekawa, E.; Serrano, S. H., Study of NADH stability using ultraviolet-visible spectrophotometric analysis and factorial design. *Anal Biochem* **1998**, *260* (1), 50-55.
134. Ma, L.; Hu, P.; Jiang, H.; Kloc, C.; Sun, H.; Soci, C.; Voityuk, A. A.; Michel-Beyerle, M. E.; Gurzadyan, G. G., Single photon triggered dianion formation in TCNQ and F4TCNQ crystals. *Sci Rep* **2016**, *6*(1), 1-7.
135. Song, J.; Ji, Z.; Nie, Q.; Hu, W., Facilely and efficiently tuning metal-organic nanostructures of a charge-transfer complex based on a water controlled nanoreaction and the chemistry of 7,7,8,8-tetracyanoquinodimethane (TCNQ). *Nanoscale* **2014**, *6* (5), 2573-2576.
136. Le, T. H.; Nafady, A.; Qu, X. H.; Bond, A. M.; Martin, L. L., Redox and Acid-Base Chemistry of 7,7,8,8-Tetracyanoquinodimethane, 7,7,8,8-Tetracyanoquinodimethane Radical Anion, 7,7,8,8-Tetracyanoquinodimethane Dianion, and Dihydro-7,7,8,8-Tetracyanoquinodimethane in Acetonitrile. *Anal Chem* **2012**, *84* (5), 2343-2350.
137. Hichiri, K.; Shirai, O.; Kitazumi, Y.; Kano, K., Coupling of Proton Transport across Planar Lipid Bilayer and Electron Transport Catalyzed by Membrane-bound Enzyme D-Fructose Dehydrogenase. *Electrochemistry* **2016**, *84* (5), 328-333.
138. Kussmaul, L.; Hirst, J., The Mechanism of Superoxide Production by NADH:ubiquinone Oxidoreductase (complex I) from Bovine Heart Mitochondria. *Proc. Natl. Acad. Sci. U. S. A.* **2006**, *103*, 7607-7612.
139. Cheng, Y. F.; Schiffrin, D. J., Redox electrocatalysis by tetracyanoquinodimethane in phospholipid monolayers absorbed at a liquid-liquid interface. *Journal of the Chemical Society-Faraday Transactions* **1994**, *90* (17), 2517-2523.
140. Fukuzumi, S.; Kondo, Y.; Tanaka, T., Effects of Base on Oxidation of an NADH Model-compound by Iron(III) Complexes and Tetracyanoethylene. *J. Chem. Soc., Perkin Trans.* **1984**, *2* (4), 673-679.
141. Ivanov, I.; Vidakovic-Koch, T.; Sundmacher, K., Alternating electron transfer mechanism in the case of high-performance tetrathiafulvalene-tetracyanoquinodimethane enzymatic electrodes. *J Electroanal Chem* **2013**, *690*, 68-73.
142. Yuasa, J.; Fukuzumi, S., A Mechanistic Dichotomy in Concerted versus Stepwise Pathways in Hydride and Hydrogen Transfer Reactions of NADH Analogues. *J. Phys. Org. Chem.* **2008**, *21*, 886-896.
143. Czochralska, B.; Lindqvist, L., Biphotonic One-electron Oxidation of NADH on Laser Excitation at 353 nm. *Chem. Phys. Lett.* **1983**, *101*, 297-299.
144. Carlson, B. W.; Miller, L. L.; Neta, P.; Grodkowski, J., Oxidation of NADH Involving Rate-limiting One-electron Transfer. *J. Am. Chem. Soc.* **1984**, *106*, 7233-7239.
145. Pandey, P. C., Tetracyanoquinodimethane-mediated Flow-injection Analysis Electrochemical Sensor for NADH Coupled with Dehydrogenase Enzymes. *Anal. Biochem.* **1994**, *221*, 392-396.
146. Tien, H. T., Cyclic Voltammetry of Electron-Conducting Bilayer Lipid-Membranes. *Bioelectrochemistry and Bioenergetics* **1984**, *13* (4-6), 299-316.
147. Solomon, T.; Bard, A. J., Reverse (uphill) Electron-Transfer at the Liquid/Liquid Interface. *J Phys Chem* **1995**, *99* (49), 17487-17489.
148. Oreilly, J. E., Oxidation-Reduction Potential of Ferro-Ferricyanide System in Buffer Solutions. *Biochim Biophys Acta* **1973**, *292* (3), 509-515.
149. Sasakura, K.; Shirai, O.; Hichiri, K.; Goda-Tsutsunii, M.; Tsujimura, S.; Kano, K., Ion Transport across Planar Bilayer Lipid Membrane Driven by D-Fructose Dehydrogenase-catalyzed Electron Transport. *Chemistry Letters* **2011**, *40* (5), 486-488.
150. Wang, N.; Feng, L. Y.; Shang, Y. C.; Zhao, J. X.; Cai, Q. H.; Jin, P., Two-Dimensional Iron-Tetracyanoquinodimethane (Fe-TCNQ) Monolayer: an Efficient Electrocatalyst For The Oxygen Reduction Reaction. *RSC Advances* **2016**, *6* (77), 72952-72958.
151. Suchanski, M. R.; Vanduyne, R. P., Resonance Raman Spectroelectrochemistry .4. Oxygen Decay Chemistry of Tetracyanoquinodimethane Dianion. *Journal of the American Chemical Society* **1976**, *98* (1), 250-252.
152. Sakata, T.; Okai, T.; Tsubomura, H., Charge-Transfer Interactions Between Oxygen and Anion Radicals of Tetracyanoquinodimethane and Tetracyanoethylene. *Bulletin of the Chemical Society of Japan* **1975**, *48* (7), 2207-2208.
153. Wood, P. M., The Potential Diagram for Oxygen at pH-7. *Biochemical Journal* **1988**, *253* (1), 287-289.
154. Kucerka, N.; Nieh, M. P.; Katsaras, J., Fluid Phase Lipid Areas and Bilayer Thicknesses of Commonly Used Phosphatidylcholines as a Function of Temperature. *Biochim. Biophys. Acta, Biomembr.* **2011**, *1808*, 2761-2771.
155. Hoops, S.; Sahle, S.; Gauges, R.; Lee, C.; Pahle, J.; Simus, N.; Singhal, M.; Xu, L.; Mendes, P.; Kummer, U., COPASI-A COMplex PATHway SIMulator. *Bioinformatics* **2006**, *22* (24), 3067-3074.
156. Back, T.; Schwefel, H. P., An Overview of Evolutionary Algorithms for Parameter Optimization. *Evolutionary Computation* **1993**, *1* (1), 1-23.
157. Nelder, J. A.; Mead, R., A Simplex-Method for Function Minimization. *Computer Journal* **1965**, *7* (4), 308-313.

158. Schaber, J., Easy parameter identifiability analysis with COPASI. *Biosystems* **2012**, *110* (3), 183-185.
159. Zielonka, J.; Marcinek, A.; Adamus, J.; Gebicki, J., Direct Observation of NADH Radical Cation Generated in Reactions with One-electron Oxidants. *J. Phys. Chem. A* **2003**, *107*, 9860-9864.
160. Marcus, R. A.; Sutin, N., Electron Transfers in Chemistry and Biology. *Biochim. Biophys. Acta, Rev. Bioenerg.* **1985**, *811*, 265-322.
161. Sethi, R.; Sangaranarayanan, M. V., Nonequilibrium Thermodynamics Formalism for Marcus Theory of Heterogeneous and Self-Exchange Electron-Transfer Rate Constants. *J. Phys. Chem. A* **2008**, *112*, 4308-4313.
162. Barker, A. L.; Unwin, P. R.; Zhang, J., Measurement of the Forward and Back Rate Constants for Electron Transfer at the Interface between Two Immiscible Electrolyte Solutions Using Scanning Electrochemical Microscopy (SECM): Theory and Experiment. *Electrochem. Commun.* **2001**, *3*, 372-378.
163. Zahl, A.; van Eldik, R.; Swaddle, T. W., Cation-dependent Electron Transfer between Ferricyanide and Ferrocyanide Ions in Aqueous Solution. *Inorg. Chem.* **2002**, *41*, 757-764.
164. Cheng, Y. F.; Schiffrin, D. J., AC Impedance Study of Rate Constants for 2 Phase Electron-transfer Reactions. *J. Chem. Soc., Faraday Trans.* **1993**, *89*, 199-205.
165. Ahuja, R. C.; Dringenberg, B. J., Reduction of TCNQ in Mixed Monolayers with Cationic Amphiphiles at the Air/Water Interface. *Langmuir* **1995**, *11* (5), 1515-1523.
166. Lim, S. K.; de Hoog, H. P.; Parikh, A. N.; Nallani, M.; Liedberg, B., Hybrid, Nanoscale Phospholipid/Block Copolymer Vesicles. *Polymers* **2013**, *5* (3), 1102-1114.
167. Patty, P. J.; Frisken, B. J., The pressure-dependence of the size of extruded vesicles. *Biophys J* **2003**, *85* (2), 996-1004.
168. Shimanouchi, T.; Ishii, H.; Yoshimoto, N.; Umakoshi, H.; Kuboi, R., Calcein permeation across phosphatidylcholine bilayer membrane: Effects of membrane fluidity, liposome size, and immobilization. *Colloid Surface B* **2009**, *73* (1), 156-160.
169. Rudolphi-Skorska, E.; Filek, M.; Zembala, M., The Effects of the Structure and Composition of the Hydrophobic Parts of Phosphatidylcholine-Containing Systems on Phosphatidylcholine Oxidation by Ozone. *J Membrane Biol* **2017**, *250* (5), 493-505.
170. Chemin, M.; Brun, P. M.; Lecommandoux, S.; Sandre, O.; Le Meins, J. F., Hybrid polymer/lipid vesicles: fine control of the lipid and polymer distribution in the binary membrane. *Soft Matter* **2012**, *8* (10), 2867-2874.
171. Jiang, W. F.; Zhou, Y. F.; Yan, D. Y., Hyperbranched polymer vesicles: from self-assembly, characterization, mechanisms, and properties to applications. *Chem Soc Rev* **2015**, *44* (12), 3874-3889.
172. Anderson, N. A.; Richter, L. J.; Stephenson, J. C.; Briggman, K. A., Characterization and control of lipid layer fluidity in hybrid bilayer membranes. *Journal of the American Chemical Society* **2007**, *129* (7), 2094-2100.
173. Weinstein, J. N.; Blumenthal, R.; Klausner, R. D., Carboxyfluorescein Leakage Assay for Lipoprotein-liposome Interaction. *Methods Enzymol.* **1986**, *128*, 657-668.
174. De Maria, P.; Filippone, P.; Fontana, A.; Gasbarri, C.; Siani, G.; Velluto, D., Cardanol as a Replacement for Cholesterol into the Lipid Bilayer of POPC Liposomes. *Colloids Surf., B* **2005**, *40*, 11-18.
175. Lingwood, D.; Simons, K., Lipid Rafts As a Membrane-Organizing Principle. *Science* **2010**, *327* (5961), 46-50.
176. Dao, T. P. T.; Fernandes, F.; Er-Rafik, M.; Salva, R.; Schmutz, M.; Brulet, A.; Prieto, M.; Sandre, O.; Le Meins, J. F., Phase Separation and Nanodomain Formation in Hybrid Polymer/Lipid Vesicles. *ACS Macro Lett* **2015**, *4* (2), 182-186.
177. Cremer, P. S.; Boxer, S. G., Formation and spreading of lipid bilayers on planar glass supports. *Journal of Physical Chemistry B* **1999**, *103* (13), 2554-2559.
178. Karimi, M.; Steinkuhler, J.; Roy, D.; Dasgupta, R.; Lipowsky, R.; Dimova, R., Asymmetric Ionic Conditions Generate Large Membrane Curvatures. *Nano Lett* **2018**, *18* (12), 7816-7821.
179. Walde, P.; Cosentino, K.; Engel, H.; Stano, P., Giant Vesicles: Preparations and Applications. *ChemBioChem* **2010**, *11* (7), 848-865.
180. Kuyper, C. L.; Kuo, J. S.; Mutch, S. A.; Chiu, D. T., Proton permeation into single vesicles occurs via a sequential two-step mechanism and is heterogeneous. *Journal of the American Chemical Society* **2006**, *128* (10), 3233-3240.
181. Yandrapalli, N.; Seemann, T.; Robinson, T., On-Chip Inverted Emulsion Method for Fast Giant Vesicle Production, Handling, and Analysis. *Micromachines* **2020**, *11* (3), 285.
182. Maenaka, Y.; Suenobu, T.; Fukuzumi, S., Efficient Catalytic Interconversion between NADH and NAD(+) Accompanied by Generation and Consumption of Hydrogen with a Water-Soluble Iridium Complex at Ambient Pressure and Temperature. *Journal of the American Chemical Society* **2012**, *134* (1), 367-374.
183. Maenaka, Y.; Suenobu, T.; Fukuzumi, S., Hydrogen Evolution from Aliphatic Alcohols and 1,4-Selective Hydrogenation of NAD(+) Catalyzed by a [C,N] and a [C,C] Cyclometalated Organoiridium Complex at Room Temperature in Water. *Journal of the American Chemical Society* **2012**, *134* (22), 9417-9427.
184. Liu, J.; Antonietti, M., Bio-inspired NADH regeneration by carbon nitride photocatalysis using diatom templates. *Energy & Environmental Science* **2013**, *6* (5), 1486-1493.
185. Hollmann, F.; Schmid, A.; Steckhan, E., The First Synthetic Application of a Monooxygenase Employing Indirect Electrochemical NADH Regeneration. *Angew Chem Int Ed* **2001**, *40* (1), 169-171.

186. Liu, Z.; Romero-Canelon, I.; Qamar, B.; Hearn, J. M.; Habtemariam, A.; Barry, N. P. E.; Pizarro, A. M.; Clarkson, G. J.; Sadler, P. J., The Potent Oxidant Anticancer Activity of Organoiridium Catalysts. *Angew. Chem., Int. Ed.* **2014**, *126* (15), 4022-4027.